ROGIER VAN DER GEER

SEARCHES FOR NEW PHYSICS THROUGH SINGLE TOP

ROGIER VAN DER GEER

SEARCHES FOR NEW PHYSICS THROUGH SINGLE TOP

SEARCHES FOR NEW PHYSICS THROUGH SINGLE TOP

ROGIER VAN DER GEER

Searches for new physics through single top

ISBN 978·94·6259·778·5
Available online as CERN-THESIS-2015-092

Printed by Ipskamp Drukkers
Cover design by Esther Ris

This work is part of the research program of the *Stichting voor Fundamenteel Onderzoek der Materie* (FOM), which is financially supported by the *Nederlandse Organisatie voor Wetenschappelijk Onderzoek* (NWO). The author was financially supported by NWO.

SEARCHES FOR NEW PHYSICS THROUGH SINGLE TOP

ACADEMISCH PROEFSCHRIFT
ter verkrijging van de graad van doctor
aan de Universiteit van Amsterdam
op gezag van de Rector Magnificus
prof. dr. D.C. van den Boom
ten overstaan van een door het College van Promoties
ingestelde commissie,
in het openbaar te verdedigen in de Agnietenkapel
op dinsdag 1 september 2015, te 14:00 uur

door ROGIER VAN DER GEER

geboren te Boston, Verenigde Staten van Amerika

Promotiecommissie:

Promotor:	prof. dr. S.C.M. Bentvelsen	Universiteit van Amsterdam
Copromotor:	dr. M. Vreeswijk	Universiteit van Amsterdam
Overige leden:	dr. D.B. Ta	Michigan State University
	prof. dr. N. de Groot	Radboud Universiteit Nijmegen
	prof. dr. R.J.M. Snellings	Universiteit Utrecht
	prof. dr. F.L. Linde	Universiteit van Amsterdam
	dr. I.B. van Vulpen	Universiteit van Amsterdam
	prof. dr. ir. P.J. de Jong	Universiteit van Amsterdam

Faculteit der Natuurwetenschappen, Wiskunde en Informatica

CONTENTS

INTRODUCTION

In all of history humankind has wondered what the world is made of. Most ancient cultures believed that four fundamental elements, earth, water, air and fire, were the basis of everything in our world, some adding more elements such as metal, light, darkness or space. In ancient Greece and ancient India the idea was developed that all substances in the world were made of indivisible particles, called atoms.

In the middle ages some modern chemical elements were discovered, and in 1789 a list containing 33 elements was compiled by Antoine Lavoisier, including among others oxygen, nitrogen and sulfur, but also light and caloric. This list grew to 66 elements in 1869, when Dmitri Mendeleev saw periodic trends in the properties of the elements and made his periodic table.

It was believed that the chemical elements were indivisible until 1897 when the electron was discovered by Joseph John Thomson. About ten years later the photon and nucleus of the atom were discovered by Albert Einstein and Ernest Rutherford respectively, and in the following decades the proton and the neutron, which make up the nucleus, were discovered.

The clear model with only electrons, photons, protons and neutrons as elementary particles did not exist for long, as in the same year of the discovery of the neutron the positron, the antiparticle of the electron, was discovered. In the following decades an extensive list of other particles was discovered, including the muon, pion, kaon, lambda baryon and neutrino.

In 1964 the quark model was developed, predicting the existence of three quarks (up, down and strange) which together make up many of the previously discovered particles. Not long after two more quarks (charm and bottom) were discovered, followed by the gauge bosons of the weak force.

The three most recent discoveries were those of the top quark in 1995, the tau neutrino in 2000 and the Higgs boson in 2012. With these, the total number of known elementary particles has come to be 17 excluding antiparticles (see figure 1): three generations of matter (fermions) each consisting of two quarks and two leptons, and five force carriers (bosons).

The theory that describes these particles and their interactions is called the Standard Model. The Standard Model not only describes the interactions at the high energies needed to create particles such as the top quark, but also at very low energies.

Nowadays particle physics research involves building the largest machines ever built. Detectors the size of a palace buried deep underground, aligned to tiny fractions of a millimeter, observe billions of collisions a second. Large collaborations of thousands of people analyze the unfathomably large amounts of data the detectors produce. A million computers sort through the data running software that is so complex that no-one can even come close to understanding every detail.

These experiments search for deviations from the Standard Model that may point to so-called *new physics*. The new physics may lead to answers to some of the big open

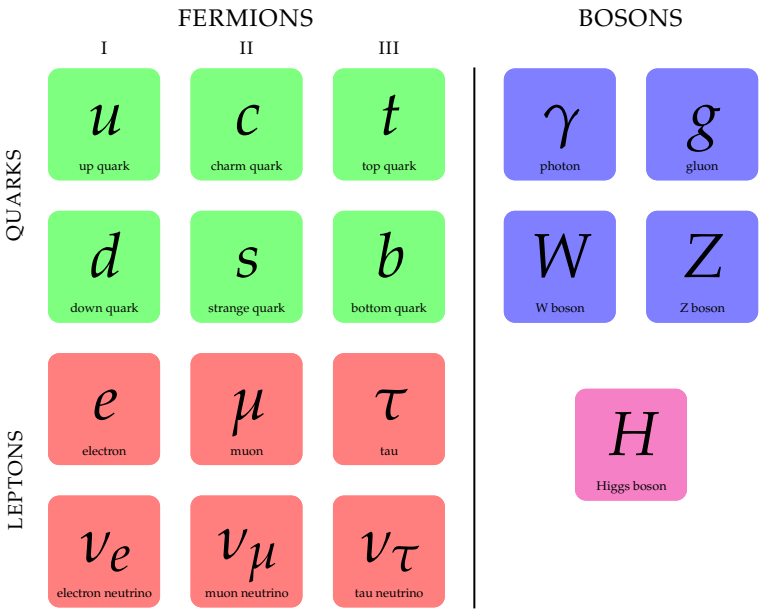

Figure 1: Particles in the Standard Model of particle physics.

questions of science, such as: Why does our universe contain primarily matter, and hardly any anti-matter? This question of *baryogenesis* is the main motivation for the analyses described in this thesis.

THIS THESIS

Chapter 1 gives a short theoretical introduction to single top processes, and describes the theory behind the analyses. Experiment follows the theory, with a description of the ATLAS experiment and the LHC in chapter 2. Once your appetite has been whetted, chapter 3 will provide you with many details on the performance of the detector, the reconstruction of physics objects in the detector and the simulation of collisions and detector response.

Now comes the analysis: a search for excited b quarks in the single top Wt-channel is described in chapter 4. Then we switch channels: an analysis in single top t-channel is spread over two chapters: chapter 5 describes a cut and count measurement of the t-channel cross section and finally chapter 6 describes a search for CP-violation in the t-channel.

1

SINGLE TOP QUARK PRODUCTION

1.1 INTRODUCTION

The Standard Model [1–4] (SM) of particle physics describes the interactions of all known elementary particles. Despite being a very complete and succesful theory, with the recent discovery of the Higgs boson being its latest success [5, 6], it is incomplete. For example, the SM does not contain gravity. Also the hierarchy problem [7], the baryon asymmetry in the universe [8] and the existence of dark matter [9] are reasons to look for new physics, or physics *beyond the Standard Model*.

Many theories that aim to solve one or more of the problems with the SM exist. Among the most notable ones are supersymmetry [10] and string theory [11].

The research presented in this thesis is motivated by the baryon asymmetry in the universe [8]. The absence of anti-matter in our universe is still one of biggest questions in cosmology today. The conditions for the existence of a matter dominated universe, the baryogenesis, have been first described in 1967 by Andrei Sakharov [12]: baryon number violation [13], C- and CP-violation, and a departure from thermal equilibrium.

All three conditions are ingredients of the Standard Model as it passes through the electroweak phase transition during the formation of our universe. The CP-violation is experimentally well established in the K- and B-systems and described in the SM by the CP-violating phase [14] in the CKM matrix [15]. However, the CP-violation in the SM is far too small, by 10 orders of magnitude, to account for the baryon asymmetry [16]. Hence, there must be *new physics* to provide a substantial enhancement of the CP-violation in the SM.

In this thesis, two analyses are presented that search for such new physics processes: a direct search for an excited b quark that realizes additional CP-violation [16], and a model-independent search for CP-violation in the top quark production and decay vertex.

Interactions involving the top quark are an interesting and promising place to look for new physics [17]. Not only are there still many details of the top quark to uncover (it was discovered only in 1995 at the CDF and DO experiments [18, 19], almost two decades after the discovery of the bottom quark), with its mass of $m_t = 173.2 \pm 0.9\ \mathrm{GeV}/c^2$ [20] it is also the heaviest known elementary particle.

In section 1.3 an introduction to a search for excited quarks decaying to top quarks is given. New physics can also influence top physics in more subtle ways, modifying processes and causing for example CP-violation. Section 1.4 introduces a model-independent search for CP-violation.

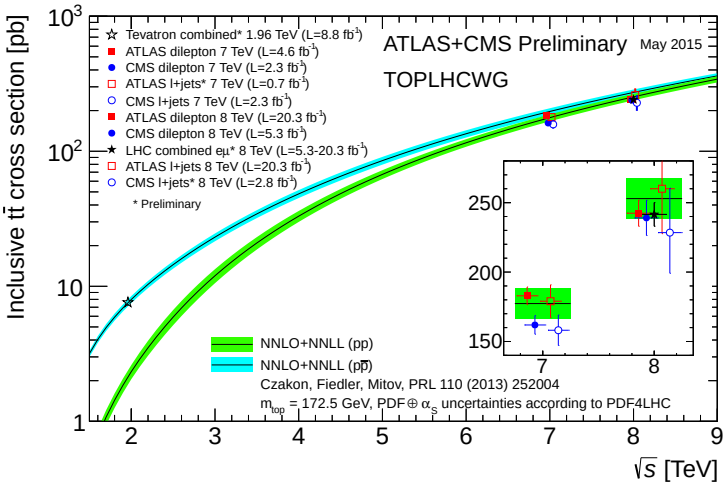

Figure 2: Predicted and measured $t\bar{t}$ cross sections at the Tevatron and the LHC [21]. All measurements show good agreement with the predictions.

1.2 SINGLE TOP PRODUCTION CHANNELS

In a proton-proton collider like the LHC (see section 2.1) top quarks are produced through a multitude of processes. Top-antitop pair production ($t\bar{t}$) is the process with the highest cross section. Figures 2 shows the cross sections of $t\bar{t}$ production at the LHC and the Tevatron. Single top production processes, where a single top quark is produced, have smaller cross sections but provide complementary and essential information on the Wtb-vertex. These processes can be divided into three *channels*: t-channel, s-channel and associated Wt production (or Wt-channel[1]). Feynman diagrams of the $t\bar{t}$, s- and t-channel and Wt associated production processes are shown in figures 4, 5 and 6 respectively, and the cross sections of these processes are shown in figure 3.

Due to the larger center-of-mass energy, the cross sections of the top production processes are larger at the LHC than at the Tevatron, where the top quark has been discovered. As can be seen in table 1, the cross sections of the four processes do not grow with the same factor: while $t\bar{t}$ and single top t-channel production gain roughly a factor of 30 from Tevatron to LHC, Wt-channel gains more than two orders of magnitude and the s-channel cross section grows by a factor of four. This is the result of a difference in nature of the colliding particles: Tevatron was a $p\bar{p}$ collider, while the LHC is a pp collider. The colliders therefore probe different combinations of valence and sea quark distributions.

1.3 EXCITED QUARKS

Some beyond the Standard Model physics models feature new heavy quarks, such as a fourth generation of quarks. The new quarks in such models have, in addition to

1 In some literature this is also called tW-channel.

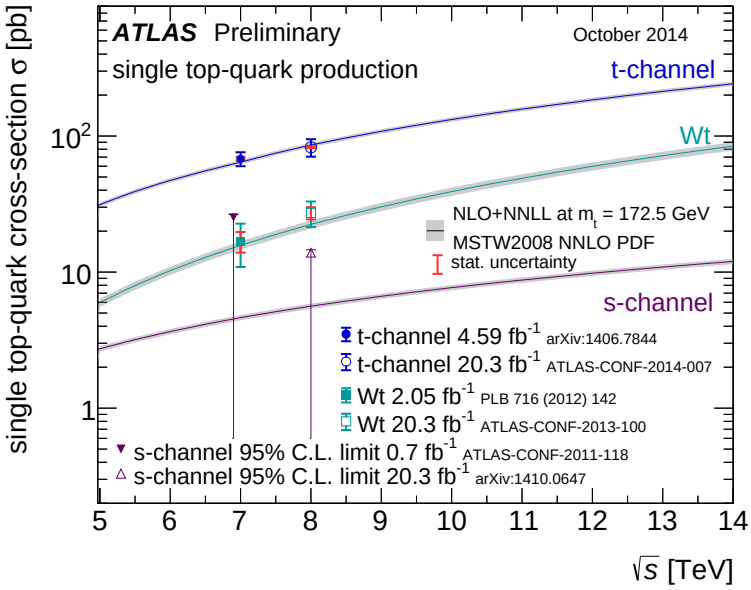

Figure 3: Predicted and measured single top cross sections at the the LHC [21]. All measurements show good agreement with the predictions.

weak couplings, new strong couplings such as technicolor or vector-like couplings. These models intend to address, for example, the hierarchy problem or the baryon asymmetry in the universe [33–37].

The Wt-channel signature is sensitive to heavy particles decaying to a top quark and a W boson. An example of such a particle is a heavy excited bottom-like quark (b^*) which is resonantly produced through the fusion of a bottom quark and a gluon [38, 39] and which decays to a top quark and a W boson [40]. A Feynman diagram of this process is shown in figure 7.

The Langrangian describing the chromomagnetic coupling through which the b^* is created is given by

$$\mathcal{L} = \frac{g_s}{2\Lambda} G_{\mu\nu} \bar{b} \sigma^{\mu\nu} \left(\kappa_L^{b^*} P_L + \kappa_R^{b^*} P_R \right) b^* + \text{h.c.}, \tag{1}$$

where g_s is the strength of the strong coupling, $G_{\mu\nu}$ is the gauge field tensor of the gluon $\Lambda = M_{b^*}$ is the scale of new physics, P_L and P_R are the projection operators and $\kappa_L^{b^*}$ and $\kappa_R^{b^*}$ are the left- and right-handed coupling strengths, respectively. This chromomagnetic coupling leads to a relatively high production cross section.

The Lagrangian describing the electroweak decay of the b^* is given by

$$\mathcal{L} = \frac{g_2}{\sqrt{2}} W_\mu^+ \bar{t} \gamma^\mu \left(g_L P_L + g_R P_R \right) b^* + \text{h.c.}, \tag{2}$$

where g_2 is the strength of the $SU(2)_L$ weak coupling and g_L and g_R are the respective coupling strengths for the left- and right-handed couplings. For all SM processes, the

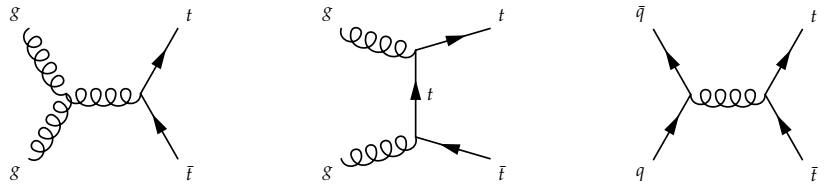

Figure 4: Leading order top-antitop quark pair production Feynman diagrams.

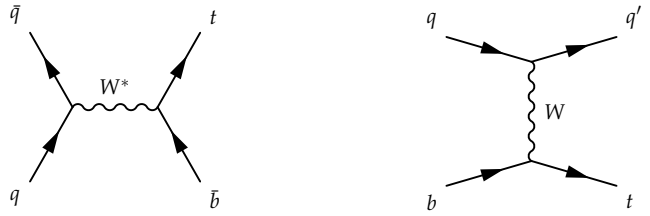

(a) s-channel (b) t-channel

Figure 5: Leading order s-channel and t-channel production Feynman diagrams.

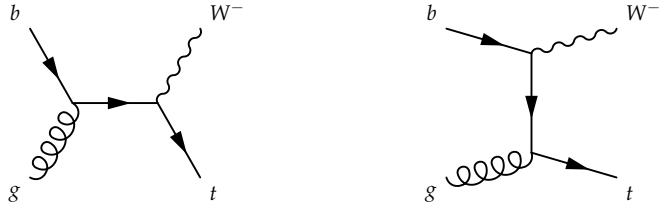

Figure 6: Leading order Wt associated production Feynman diagrams.

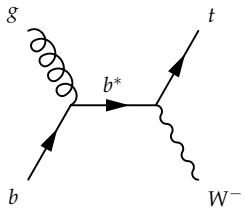

Figure 7: Excited bottom quark production and decay Feynman diagram.

	Tevatron	LHC	
$\sqrt{s}$	1.96 TeV	7 TeV	8 TeV
$t\bar{t}$	7.60±0.41 [22]	173.3±10.1 [23]	237.7±32 [24]
s-channel	1.29±0.25 [25]	4.6±0.2† [26]	5.6±0.2† [26]
t-channel	2.26±0.12† [27]	82.7±13.1 [28]	85±12 [29]
Wt-channel	0.14±0.03† [30]	16.8±5.7 [31]	23.4±5.5 [32]

Table 1: Cross section (in picobarn) of the top production processes at the Tevatron and at two center-of-mass energies at the LHC. The center-of-mass energy is not the only difference between the machines, as the Tevatron was a proton-antiproton machine, and the LHC is a proton-proton collider. Where available, observed cross sections are shown. Cross sections noted with a dagger† are theoretical cross sections.

electroweak coupling is purely left-handed, but for the b^* it could left-handed, right-handed or vector-like[2].

The branching ratios of the excited quark are shown in figure 8a. For a left-handed coupling the decay is dominated by $b^* \to Wt$ for masses above 400 GeV/c^2. For masses below 400 GeV/c^2, $b^* \to Zb$ is the primary decay channel.

The cross section of the excited quark production and decay to Wt at the LHC is shown in figure 8b. At $\sqrt{s} = 7$ TeV and for a mass of $m_{b^*} = 900$ GeV/c^2, the cross section times branching ratio is 0.80 pb, which is of the order of 5% of the SM Wt-channel production cross section at that center-of-mass energy. For masses below $m_{b^*} = 500$ GeV/c^2, the cross section times branching ratio of $b^* \to Wt$ is larger than the SM Wt-channel cross section. The width of the b^* is small enough to recognize a b^* signal by its mass. This makes the Wt-channel a good candidate for a search for excited quarks, or other new heavy quarks that decay to Wt. In chapter 4 a search for the b^* is presented.

1.4 POLARIZATION IN T-CHANNEL SINGLE TOP

Due to its very high mass and its decay width of 2 GeV [15] the top quark has a lifetime of the order of 10^{-25} s. As this is much shorter than the timescale of QCD interactions, the top quark does not hadronize before decay [41]. The top quark is therefore the only quark of which the spin can be measured. Single top quarks produced in the LHC are strongly polarized [42], and this polarization is sensitive to new physics, such as supersymmetry [43].

A general, minimal, parameterization of the Wtb vertex arising from effective operators of maximum dimension six can be written as [44]

$$\begin{aligned}\mathcal{L}_{Wtb} = &-\frac{g}{\sqrt{2}}\bar{b}\gamma^\mu\left(V_L P_L + V_R P_R\right) t W^-_\mu \\ &-\frac{g}{\sqrt{2}}\bar{b}\frac{i\sigma^{\mu\nu}q_\nu}{M_W}\left(g_L P_L + g_R P_R\right) t W^-_\mu + \text{h.c.},\end{aligned} \tag{3}$$

2 A vector-like coupling has non-zero coupling strengths for the left- and right-handed couplings.

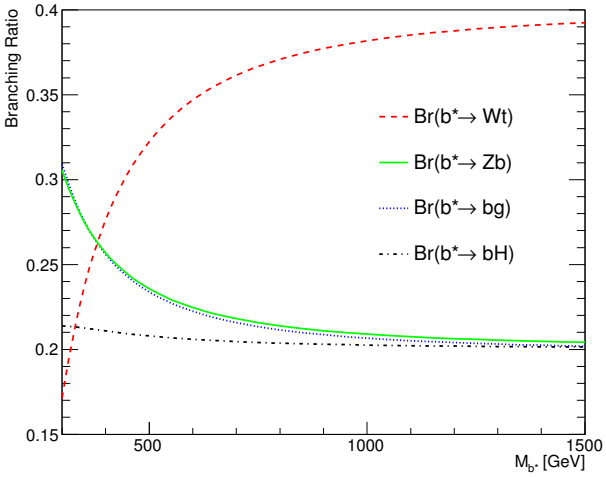

(a) Branching ratio of the left-handed decay of an excited bottom quark.

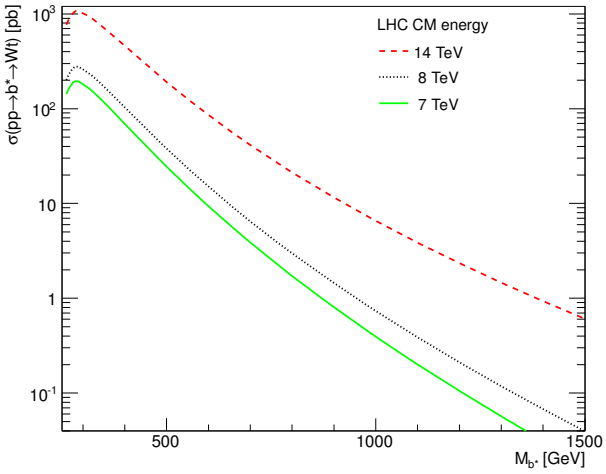

(b) Cross section times branching ratio of the production of an excited bottom quark and the decay to Wt at the LHC.

Figure 8: Branching ratio and cross section of the left-handed production and decay of an excited bottom quark as a function of its mass [40].

where V_L and V_R are the coupling strengths of the left- and right-handed vector couplings repectively, and g_L and g_R are the left- and right-handed tensor couplings respectively. In the SM, $V_L = 1$ while $V_R = g_L = g_R = 0$.

Here g_R is particularly interesting, as a non-zero imaginary part of g_R implies CP-violation. The imaginary part of g_R is experimentally accessible through the angular distribution of the top quark and its decay products, as explained below.

1.4.1 *Top quark polarization*

The angular distribution of any decay product of the top quark is given by

$$\frac{1}{\Gamma}\frac{d\Gamma}{d\cos\theta} = \frac{1}{2}\left(1 + P\alpha\cos\theta\right), \tag{4}$$

where θ is the angle between the momentum of the decay product in the top quark rest frame and the top spin direction, Γ is the decay width of the top quark, the constant α is the *spin analyzing power* of the decay product, and P is the degree of polarization of the top quark [45]. In the decay $t \to W^+ b \to \ell^+ \nu_\ell b$, the spin analyzing power for the decay products are shown in table 2.

α_{ℓ^+}	$= 1.000$
α_b	$= -0.403$
α_{W^+}	$= 0.403$
α_{ν_ℓ}	$= -0.324$

Table 2: Leading order spin analyzing power for all decay products of the top quark [42]. The corresponding quantities for anti top quarks have equal values with opposite signs.

The decay of a polarized top quark is visualized in figure 9. The W boson is either left-handed or longitudinal; a right-handed W boson would require the bottom quark to have spin-$\frac{2}{3}$ and is therefore not allowed. The momentum of a longitudinal W boson is parallel to the spin of the top quark, while the momentum of a left-handed W boson is antiparallel to the top quark spin. Since the neutrino is always left-handed, the momentum of the charged lepton is always in the direction of the spin of the W boson in the W boson rest frame. As a result, and due to the momentum of the W boson in the top quark rest frame, the projection of the momentum of the charged lepton in the top quark rest frame onto the top quark spin is always parallel to this spin. This means that the charged lepton is the most sensitive spin analyzer.

The degree of polarization of the top quark depends on the chosen spin basis. The top quark is highly polarized in the helicity basis and the spectator basis. In the helicity basis the spin quantization axis is chosen along the direction of the momentum of the top quark in the center-of-mass frame, while in the spectator basis the spin quantization axis is chosen along the direction of the momentum of the spectator quark[3] in the top quark rest frame [46]. If the center-of-mass frame is calculated using only the top quark and the spectator jet these two bases are equal but inverted.

3 The spectator quark is the light quark produced in a t-channel diagram. In figure 5b, q' is the spectator.

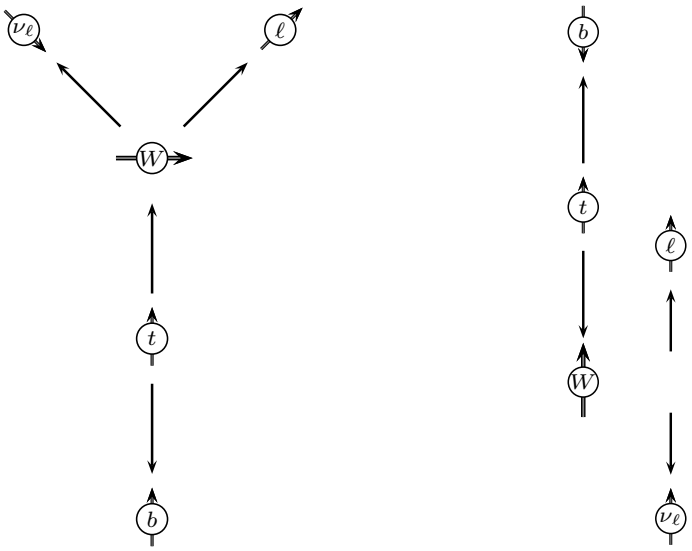

(a) (b)

Figure 9: Spin in the decay of a top quark. Only two configurations are possible: in a the direction of the momentum of the W boson is parallel to the spin of the top quark, while in b it is antiparallel.

Figures 10a-f show the definitions of several polarization-sensitive angles. The most sensitive angle which can be used to measure the polarization using equation 4, θ^x, which uses the charged lepton as the spin analyzer in the spectator basis, is shown in figure 10b. An alternative angle, using the W boson as spin analyzer, is shown in figure 10c. This angle is much less sensitive due to the lower spin analyzing power of the W boson.

1.4.2 *W boson polarization*

The polarization of the W boson decay product of top quarks can also be measured. This is done using the distribution of the angle between the lepton producted in the W boson decay and a spin axis.

The helicity, the spin along the momentum axis, of the W boson can be measured using the distribution of the angle between the W boson momentum axis in the top quark rest frame and the momentum of the charged lepton in the W boson rest frame, as shown in figure 10d. For polarized top quarks two alternative spin axes can be considered: the *normal* axis ($\hat{N}$), perpendicular to the momentum of the W boson in the top quark rest frame and the top quark spin direction and the *transverse* axis ($\hat{T}$), perpendicular to both the normal axis and the W momentum in the top quark rest frame as defined in figure 10a.

In the case of fully polarized top quarks, the angular distribution is given by

$$\frac{1}{\Gamma}\frac{d\Gamma}{d(\cos\theta)} = \frac{3}{8}(1+\cos\theta)^2 F_+ + \frac{3}{8}(1-\cos\theta)^2 F_- + \frac{3}{4}(\sin\theta)^2 F_0, \tag{5}$$

where θ is the angle between the momentum of the lepton in the W boson rest frame and the reference axis (either the transverse or the normal axis, see figures 10e and f), Γ is the decay width of the W boson, and F_+, F_- and F_0 are the polarization fractions corresponding to right-handed, left-handed and longitudinal helicities respectively. Each term is maximal ($= 3/4$) when the momentum of the lepton is parallel to the direction of the spin: $\theta = 0$ for right-handed, $\theta = \pi$ for left-handed and $\theta = \pi/2$ for longitudinal helicities. The polarization fractions satisfy

$$F_+ + F_- + F_0 = 1. \tag{6}$$

The SM predictions for the polarization fractions are listed in table 3.

When the top quarks are not fully polarized (i.e. $P < 1$), the polarization fractions in equation 5 are replaced by effective polarization fractions depending on P:

$$\tilde{F}_+ = \frac{1+P}{2}F_+ + \frac{1-P}{2}F_-, \tag{7}$$

$$\tilde{F}_- = \frac{1+P}{2}F_- + \frac{1-P}{2}F_+, \tag{8}$$

$$\tilde{F}_0 = F_0. \tag{9}$$

From the polarization fractions we can construct the forward-backward asymmetry in the angular distributions as follows:

$$A_{FB}^{\hat{N}} = \frac{3}{4}\left(\tilde{F}_+^{\hat{N}} - \tilde{F}_-^{\hat{N}}\right) = \frac{3}{4}P\left(F_+^{\hat{N}} - F_-^{\hat{N}}\right), \tag{10}$$

$$A_{FB}^{\hat{T}} = \frac{3}{4}\left(\tilde{F}_+^{\hat{T}} - \tilde{F}_-^{\hat{T}}\right) = \frac{3}{4}P\left(F_+^{\hat{T}} - F_-^{\hat{T}}\right). \tag{11}$$

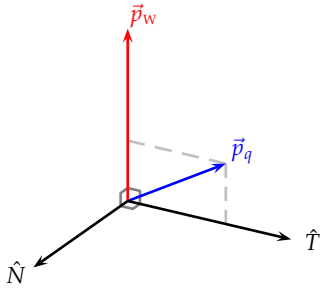

(a) Definition of $\hat{N}$ and $\hat{T}$: $\hat{N} = \vec{p}_q \times \vec{p}_W$ and $\hat{T} = \vec{p}_W \times \hat{N}$, where $\vec{p}_q$ and $\vec{p}_W$ are the momenta of respectively the spectator quark and the W boson in the top quark rest frame.

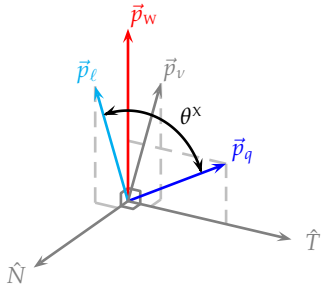

(b) Angle θ^x between the momenta of the spectator quark ($\vec{p}_q$) and the charged lepton ($\vec{p}_\ell$), both in the top quark rest frame.

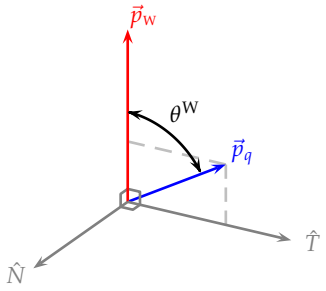

(c) Angle θ^W between the momenta of the spectator quark ($\vec{p}_q$) and the W boson ($\vec{p}_W$), both in the top quark rest frame.

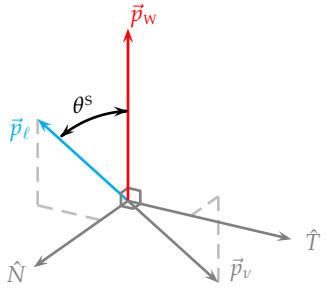

(d) Angle θ^s between the momenta of the W boson in the top quark rest frame ($\vec{p}_W$) and of the charged lepton in the W boson rest frame ($\vec{p}_\ell$).

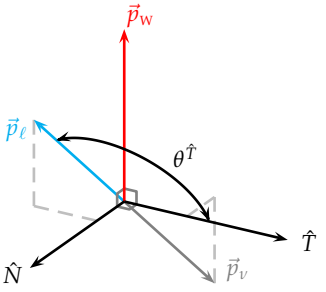

(e) Angle $\theta^{\hat{T}}$ between the momentum of the charged lepton in the W boson rest frame ($\vec{p}_\ell$) and the transverse axis.

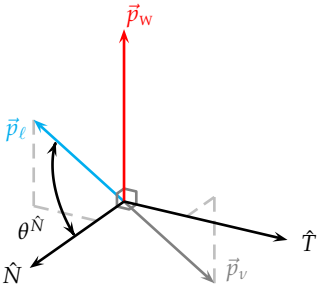

(f) Angle $\theta^{\hat{N}}$ between the momentum of the charged lepton in the W boson rest frame ($\vec{p}_\ell$) and the normal axis.

Figure 10: Definition of the spin axes $\hat{N}$ and $\hat{T}$ and the angles θ^x, θ^W, θ^s, $\theta^{\hat{T}}$ and $\theta^{\hat{N}}$.

$F_+^{\hat{N}} = 0.426$	$F_+^{\hat{T}} = 0.679$
$F_-^{\hat{N}} = 0.426$	$F_-^{\hat{T}} = 0.172$
$F_0^{\hat{N}} = 0.149$	$F_0^{\hat{T}} = 0.149$
(a)	(b)

Table 3: The SM predictions at tree-level for the polarization fractions in the normal basis (a) and the transverse basis (b) [45].

While $A_{FB}^{\hat{T}}$ is sensitive to the real parts of anomalous Wtb-couplings, $A_{FB}^{\hat{N}}$ is sensitive to the imaginary parts. It is particularly sensitive to the imaginary part of the right-handed tensor coupling $\mathfrak{I}(g_R)$. When $V_R = g_L = 0$ and $V_L = 1$, like in the SM,

$$A_{FB}^{\hat{N}} = 0.64\,P\,\mathfrak{I}(g_R), \tag{12}$$

for small g_R [45]. When combining top and antitop decays, a non-zero $A_{FB}^{\hat{N}}$ implies CP-violation. Hence this quantity provides a promising means to study anomalous couplings, and a search for CP-violation is described in chapter 6.

1.5 SUMMARY

Although the SM is very complete and successful, there are several reasons to look for new physics. Processes involving the top quark are interesting to study in search for new physics, for example because of the very high mass of the top quark. The single top t- and Wt-channels are especially good candidates for searches for new physics, because they are sensitive to the polarization of the top quark and to new, heavy particles decaying to signatures similar to these channels.

2

THE LHC AND ATLAS

2.1 THE LARGE HADRON COLLIDER

The Large Hadron Collider (LHC) is a proton-proton collider situated at the European Organization for Nuclear Research (CERN) in Geneva, Switzerland [47]. It is a synchrotron with a circumference of 27 km, and is built in the tunnel of the former Large Electron-Positron Collider (LEP). It was designed to collide proton beams with a center-of-mass energy of 14 TeV at a luminosity of 10^{34} $cm^{-2}s^{-1}$.

The two beams of the LHC cross at four points in the tunnel. At these interaction points four large experiments have been built:

- **A Toroidal LHC ApparatuS** (ATLAS) is a general-purpose detector designed to explore the full spectrum of proton-proton physics. A detailed description of ATLAS follows in section 2.2.
- **Compact Muon Solenoid** (CMS) is also a general-purpose detector, with a similar physics programma as ATLAS [48].
- **Large Hadron Collider beauty** (LHCb) is a forward detector designed especially for studying rare B-meson decays [49].
- **A Large Ion Collider Experiment** (ALICE) is an experiment designed for studying lead-lead collisions, which the LHC can also produce [50].

The startup of the LHC took place in summer 2008, but was quickly followed by a magnet quench accident. After a long period of repairs it was restarted at the end of 2009, and in the years 2010, 2011 and 2012 three datasets (*runs*) were taken. As the luminosity increased greatly during the 2010 run, the two latter datasets are much larger. During 2010 and 2011 the center-of-mass energy of the LHC was $\sqrt{s} = 7$ TeV, while in 2012 it was $\sqrt{s} = 8$ TeV. The total delivered luminosity was 5.46 fb^{-1} and 22.8 fb^{-1} in 2011 and 2012 respectively. See Section 3.1.1 for more details.

2.2 THE ATLAS EXPERIMENT

The ATLAS detector was designed to cover the full frontier of proton-proton physics [51]. In the design the following physics goals were set:

- large acceptance of almost the full solid angle,

- good charged-particle momentum resolution and reconstruction efficiency,
- very good electromagnetic calorimetry and full-coverage hadronic calorimetry,
- good muon identification and momentum resolution,
- highly efficient triggering.

The Standard Model Higgs-boson, which has been discovered by ATLAS in 2012 [5], was an important benchmark during the design process of the ATLAS detector, together with new heavy gauge bosons and supersymmetry.

2.2.1 *Coordinate system*

The origin of the right-handed ATLAS coordinate system lies in the nominal interaction point. The positive x-axis points to the center of the LHC ring, the positive y-axis points up (i. e. away from the center of the earth) so that the z-axis is parallel to the beam axis. The x-y-plane is called the *transverse* plane, being perpendicular to the beam axis. The azimuthal angle (around the beam axis) is denoted by ϕ and the polar angle (from the beam axis) is denoted[1] by θ.

From the polar angle θ a *pseudorapidity* is defined as $\eta \equiv -\ln\tan(\theta/2)$. Transverse properties, like the transverse momentum p_T and the missing transverse energy E_T^{miss}, are projected onto the transverse plane.

2.2.2 *Detector layout*

Three detector subsystems of ATLAS are positioned enclosing eachother around the interaction point. Magnet subsystems provide all the detector subsystems with a magnetic field.

Each subsystem is divided in a *barrel* and two *endcaps*. The barrel has the form of a cylinder with the beam line in its axis, serving the *central* (low absolute pseudorapidity) region. The endcaps close off the cylinder of the barrel, serving the *forward* (high absolute pseudorapidity) regions.

The magnet system and each of the detector subsystems will be briefly discussed in the following sections.

2.2.3 *Magnets*

In the center of the detector a superconducting solenoid with an axial length of 5.8 m and a diameter of 2.5 m encloses the inner tracker and provides it with a 2 T axial field.

The much larger superconducting toroidal magnets from which ATLAS derives its name can be found inside the muon spectrometer and consists of one barrel part and two endcaps. Each of these magnets contains eight superconducting coils, providing a field of 0.5 to 1 T average in the muon spectrometer. The magnetic field integrated over the path of a muon ranges from 3 Tm in the barrel to 6 Tm in the endcaps.

1 The naming convention in physics is opposite to the one in mathematics, where the azimuthal angle is denoted by ϕ and the polar angle is denoted by θ. This may be confusing for mathematicians.

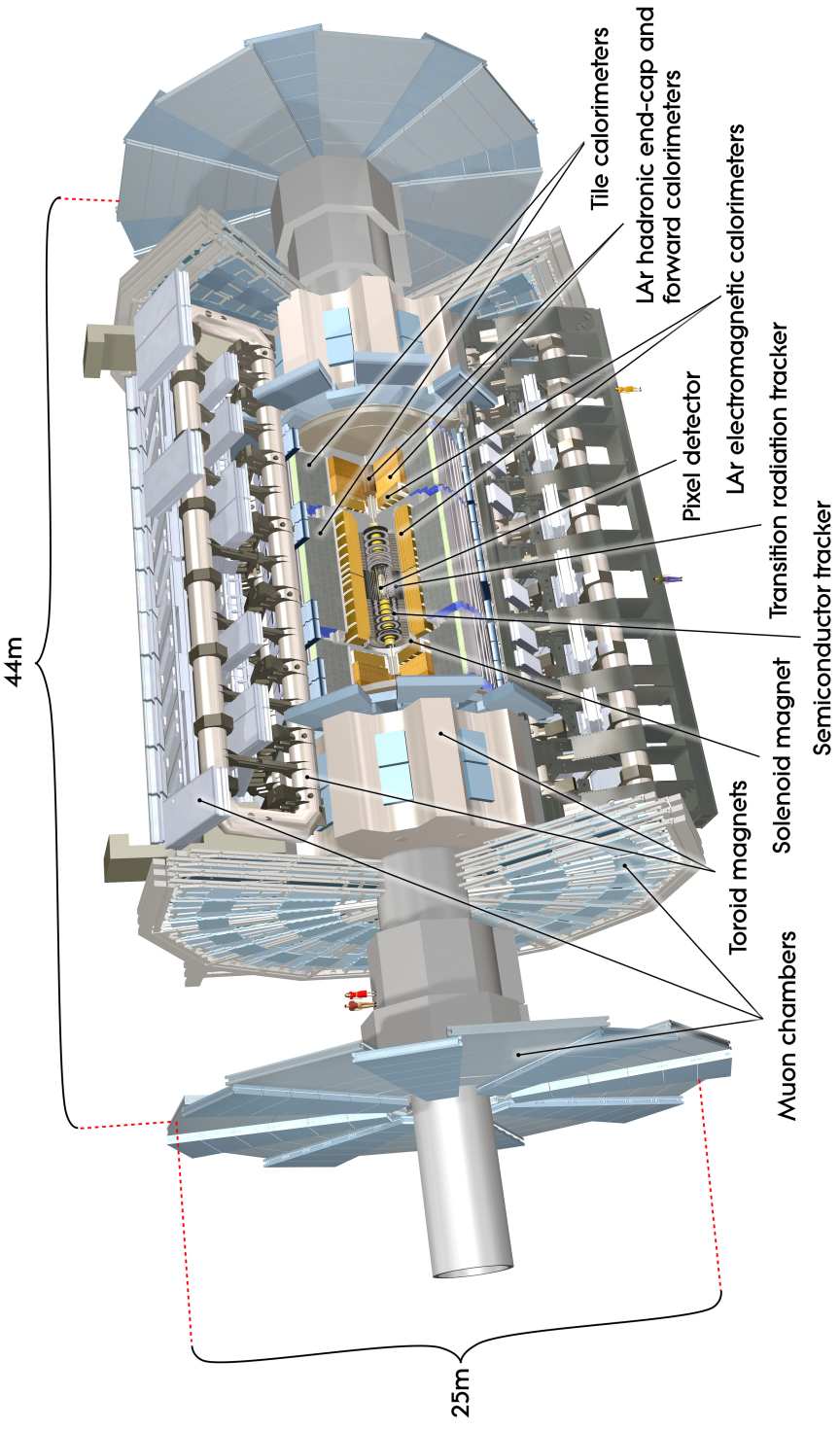

Figure 11: A computer-generated overview of the ATLAS detector.

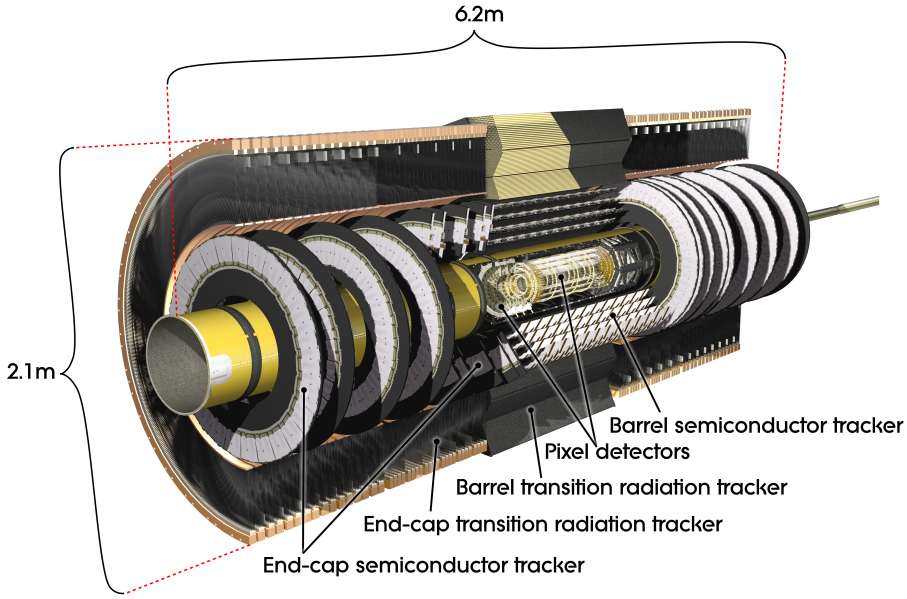

Figure 12: A computer-generated overview of the ATLAS inner tracker.

2.2.4 *Inner tracker*

The ATLAS inner tracker is composed of three subsystems: which are, from the inside out: the pixel detector, the silicon strip detector (SCT) and the Transition Radiation Tracker (TRT) [52]. The layout of the inner tracker is shown in Figure 12. Both the pixel detector and SCT are silicon detectors, while the TRT is a gas filled detector. The inner tracker is fully enclosed in the solenoid magnet.

The pixel detector is designed to be a very accurate tracker as close to the beam line as possible. In the barrel it consists of three concentric cylinders with radii of about 5.9 cm, 12 cm and 14 cm, while the endcaps consist of four disks. The pixel chips are made of 250 µm thick n-type silicon, equivalent to less than 1.39% of a radiation length. All layers combined contain over 80 million pixels, which amounts to the vast majority of all ATLAS readout channels.

	Barrel		End caps	
	$R\phi$	z	$R\phi$	R
pixel	10 µm	115 µm	12 µm	77 µm
SCT	17 µm	580 µm	17 µm	580 µm

Table 4: Intrinsic spatial detector resolution.

The SCT consists of silicon microstrip detectors. The strips measure 6.4 cm by 80 µm, and thus alone provide accuracy in one direction (ϕ) only. By using two modules of strip detectors under a slight angle with respect to eachother, some accuracy in the z-direction (θ for the endcap) is restored. The SCT has four layers of detectors in the barrel region, and nine disks in each endcap.

The SCT sensors are made of a much cheaper classic p-in-n silicon with a thickness of about 285 µm. Due to the one-dimensional granularity the SCT and despite its larger size, the 6.3 million readout channels of the SCT are a fraction of that of the pixel detector.

The tracking resolution of the pixel detector and the SCT can be found in Table 4.

The TRT is a straw tube detector with electron identification capabilities. It contains total of $3.7 \cdot 10^5$ straw tubes with a diameter of 4 mm and a length varying between 150 cm in the barrel down to 20 cm in some end cap regions. In the barrel the tubes are oriented axially, while in the end caps they are oriented radially. The barrel tubes are electrically separated at the center to reduce occupancy, resulting in double the number of readout channels in the barrel. The total number of readout channels of the TRT is $4.2 \cdot 10^5$.

An average track traversing the TRT produces 36 hits, making pattern recognition relatively easy, and resulting in a tracking accuracy of 130 µm (in one dimension). Electron identification is done by using xenon gas to detect transition radiation photons produced between the straws.

To achieve tracking resolutions as shown in Table 4 the detector has to be properly aligned: i. e. deformations in the detector structure have to be measured accurately in order to reconstruct tracks correctly. While the inner tracker is installed in the ATLAS detector its alignment can be measured in two ways: by using information from measured tracks and by using optical alignment measurements. Accurate alignment using tracks can only be done if the detector is very stable in time, or if the alternative alignment methods can be used to correct for short term distortions.

In the pixel detector and the SCT two optical alignment methods are used: *straightness monitors* which measure the deviation from a straight line with mutiple translucent photosensors in a laser beam, and frequency scan interferometry [53] to measure distances. Using these methods, pixel sensors can be located with an precision down to about 10 µm. In the TRT the alignment requirements are such that track alignment alone is sufficient.

Together the three subsystems of the inner tracker achieve a momentum resolution of $\sigma \approx 1.5\%$ for low-p_T tracks and of $\sigma\left(p_T^{-1}\right) \approx 0.4\ \text{TeV}^{-1}$ for high-p_T central tracks. The impact parameter resolutions are as small as $\sigma(d_0) \approx 13$ µm and $\sigma(z_0) \approx 75$ µm for central 25 GeV/c tracks, and the inner tracker has sensitivity over the full $|\eta| \leqslant 2.5$ range.

2.2.5 *Calorimeter*

The calorimeter is located outside of the solenoid magnet. It is divided into a liquid argon filled calorimeter up to a detector radius of 2.2 m and an iron-scintillator tile calorimeter with an outer radius of 4.2 m which surrounds the liquid argon detector [54, 55]. A schematic of the calorimeter layout is shown in Figure 13.

The electromagnetic (EM) calorimeter is designed to have a much smaller granularity than the hadronic calorimeter, while the hadronic calorimeter contains much more material

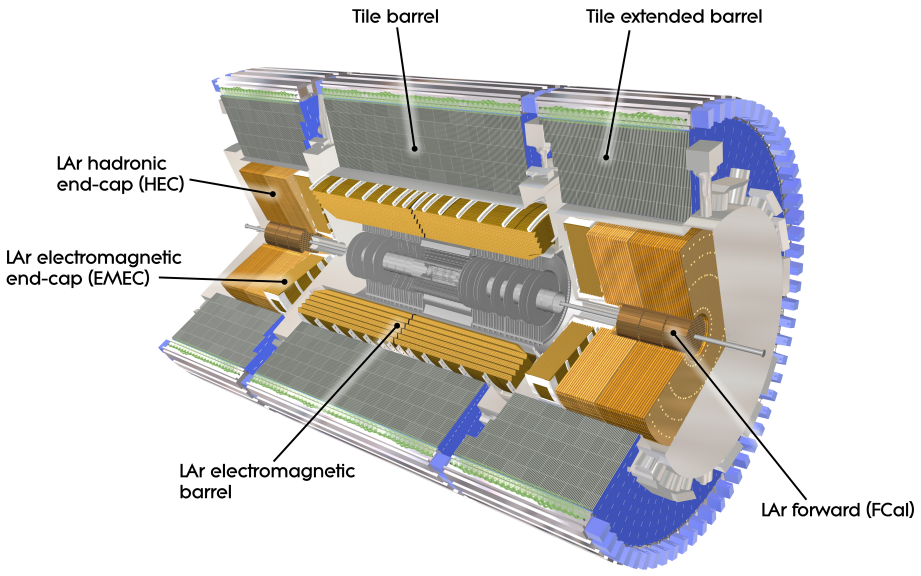

Figure 13: A computer-generated overview of the ATLAS calorimeter.

in order to stop the high energetic (hadronic) particles and to minimize escaping of such particles into the muon spectrometer. The granularity of each calorimeter subdetector is summarized in Table 5.

The liquid argon calorimeter is contained in three cryostats: one barrel and two endcaps. The barrel cryostat is shared with the solenoid magnet. The endcap cryostats contain an electromagnetic calorimeter as well as an hadronic liquid argon calorimeter, while the tile calorimeter acts as hadronic calorimeter in the barrel region. A forward calorimeter (FCAL) with an outer radius of 47 cm is also situated inside the calorimeter endcaps.

The barrel liquid argon calorimeter, which covers the range $0 < |\eta| < 1.475$, is divided into two half-barrels, which each consist of 1024 lead-stainless-steel converters covered with electrodes and with readout boards in between. The converters are shaped like an accordion to create a large surface while maintaining continuity in ϕ. As a function of pseudorapidity the amount of material in the barrel liquid argon calorimeter varies from about 1 to 2 absorption lengths, and 20 to 30 radiation lengths.

The endcap electromagnetic calorimeters ($1.375 < |\eta| < 3.2$) each consist of two concentric wheels of accordion-shaped converters, and otherwise have a design similar to that of the barrel part.

The hadronic endcap calorimeters do not use the accordion electrode structure, but use flat copper plates. Each endcap consists of two wheels, one with 25 mm thick plates, and a second with 50 mm thick plates. The thickness of these plates is chosen such that the

amount of material in the hadronic endcap calorimeter in terms of absorption lengths is about 10, similar to that of the tile calorimeter.

The FCAL ($3.1 < |\eta| < 4.9$) consists of a grounded metal matrix with channels filled with concentric high-voltage rods and tubes. The liquid argon gap between the rod and the tube can be as narrow as 250 μm. With a density of up to 14.5 g/cm^3 the FCAL is much denser than the other calorimeters, leading to an average of about 10 absorption lengths of material, similar to that of the hadronic calorimeters.

The tile calorimeter is split up into one barrel and two *extended barrel* parts, which have the form of a barrel around the liquid argon endcaps. A gap of 60 cm exists between the barrel and extended barrel parts. All parts contain steel tiles with scintillators in between. Light produced by the scintillators is transported out of the calorimeter using optical fibers.

Just like the endcap hadronic calorimeter and the FCAL, the barrel tile calorimeter amounts to about 10 absorption lenghts of material, while the material in the extended barrel varies from about 7 to 13 absorption lengths as a function of pseudorapidity.

	$\Delta\eta \times \Delta\phi$
EM barrel	0.025×0.025
EM endcap	0.025×0.1
FCAL	3.0×2.6
Had. endcap	0.1×0.1
Tile barrel	0.1×0.1
Tile endcap	0.1×0.1

Table 5: Granularity per calorimeter subdetector. In some subdetectors the granularity varies by pseudorapidity region or by layer. In such cases the best granularity is quoted.

The calorimeters have an energy resolution below 5% for electrons, and an angular resolution of $< 1.5°$ for particles up to 300 GeV. The coverage of the calorimeters goes up to $|\eta| < 4.7$, leaving only a very small part of the solid angle uncovered.

2.2.6 *Muon spectrometer*

The ATLAS muon spectrometer consists of a precision system and a trigger system, arranged such that each muon traverses at least three layers of precision chambers and at least one layer of trigger chambers [56]. The barrel of the muon spectrometer is interspersed between the barrel toroid magnet coils, while in the endcaps this is not possible.

Precision track measurements are done by two types of chambers: *monitored drift tube* chambers (MDT) and *cathode strip chambers* (CSC). The CSCs are only used in the very forward regions as they have a finer granularity so that they can cope with the higher flux of muon and large backgrounds.

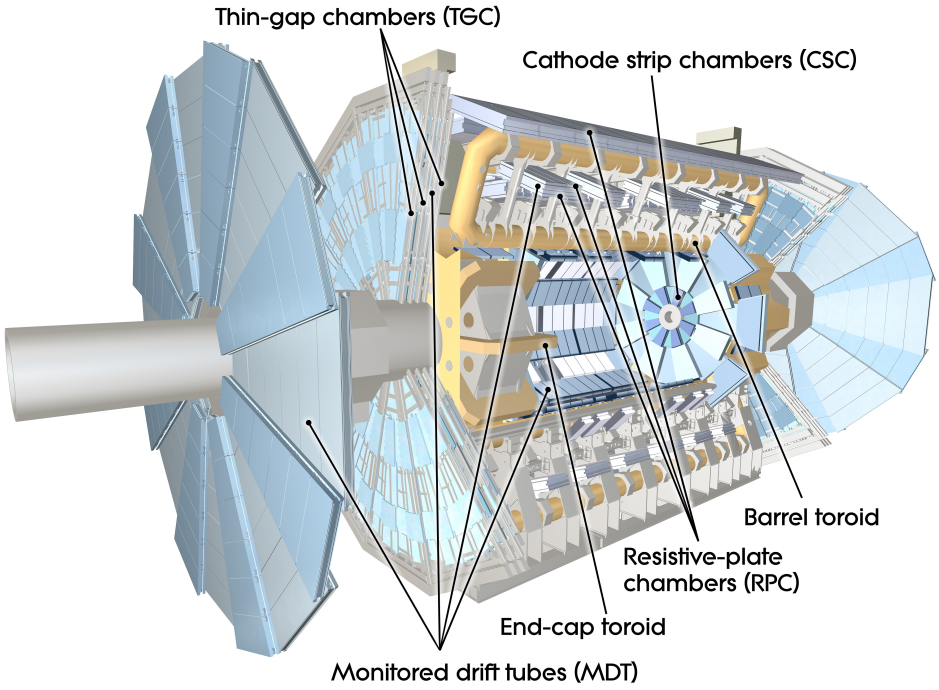

Figure 14: A computer-generated overview of the ATLAS muon spectrometer.

The MDT chambers are gas-filled detectors using 30 mm diameter aluminum tubes with an anode wire along the axis of the tube. The resolution on the drift radius of a single wire is 80 μm, and each chamber incorporates several layers (6 to 8) of tubes to achieve an accuracy below 50 μm in the direction of the sagitta. The length of the tubes varies from 70 cm to over 6 m.

An MDT chamber consists of an aluminum frame with several layers of tubes on each side. The frame is designed such that the gravitational bending of the tubes is similar to the gravitational sag of the wires. The frame also contains an alignment system which is described in Section 2.3.

The almost 1200 MDT chambers together cover a total of 5500 m^2 and have $3.7 \cdot 10^5$ readout channels.

The CSCs are multiwire proportional chambers with an anode wire pitch and anode-cathode spacing of 2.54 mm. The cathode strips, which are oriented perpendicular to the anode wires, have a spacing of 5.08 mm. Resolutions better than 60 μm can be achieved by charge interpolation using multiple strips. The CSCs also have a good time resolution of 7 ns.

Only 32 CSCs are installed in ATLAS, covering 27 m^2. Due to the high density of wires these chambers combined have $67 \cdot 10^3$ channels.

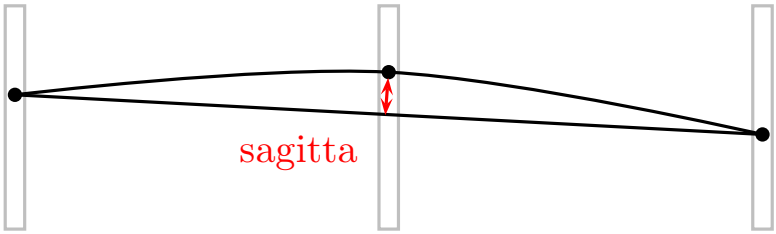

Figure 15: Definition of the sagitta: in a three-point track measurement, the sagitta is the distance from the middle point of the three to the straight line connecting the two exterior points.

The trigger chambers of the muon spectrometer provide the trigger system with a muon p_T-cutoff for low-p_T muons. They also provide bunch crossing identification, as the MDT precision chambers do not have the time resolution to do so, and a coarse (5 to 10 mm) measurement of the second coordinate of a track. Two types of trigger chambers are used in the ATLAS muon spectrometer.

Resistive plate chambers (RPC) are the trigger chambers used in the barrel region. They consist of a narrow gas-filled gap between two resistive plates, with a 4.5 kV field acrross the gap. The RPCs have a time resolution of 1.5 ns, which is more than sufficient to identify bunch crossings at intervals of 25 ns. The RPCs have a total of $35 \cdot 10^4$ channels, and a time resolution of 1.5 ns.

Triggering in the endcaps is done by *thin gap chambers* (TGC). These TGCs are similar to the CSCs, but have an anode pitch which is larger than the anode-cathode spacing and use a quenching gas mixture. Up to 7 layers of TGCs are used per MDT chamber, which leads to a total of $44 \cdot 10^4$ channels, and a time resolution of 4 ns.

The muon spectrometer covers the full rapidity region of $|\eta| < 2.7$, except for a gap at $\eta = 0$. Muon momentum resolution is $\sigma \approx 2\%$ for muons with $p_T = 10$ GeV/c, and goes up to $\sigma \approx 11\%$ for muons with $p_T = 1$ TeV/c, while the angular resolution of ϕ is on average 1 mrad. The trigger efficiency of the muon spectrometer trigger system is $> 90\%$ for $p_T = 25$ GeV/c central muons.

2.3 MUON SPECTROMETER ALIGNMENT

The ATLAS muon spectrometer is designed to provide a p_T-resolution of 10% for 1 TeV/c muons [57]. The minimum sagitta (see Figure 15) of a 1 TeV muon track (at $\eta = 0$) is 500 µm, meaning that the error on the measurement of the sagitta must be less than 50 µm. To reach this level of precision, the alignment of the muon spectrometer precision chambers must be very well known. Like in the inner tracker, the alignment of the muon spectrometer can be determined by using information from fitted tracks and by using an optical alignment system.

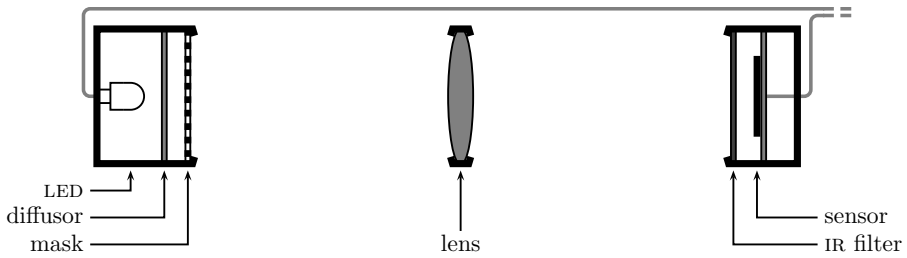

Figure 16: A schematic view of a RASNIK system. Infrared light from an illuminated coded mask is projected onto a sensor via a lens.

Figure 17: A RASNIK mask image projected onto a sensor. The code lines that replace the checkerboard pattern every ten lines are clearly visible.

The muon spectrometer barrel and endcaps each have their own optical alignment system. In each of these subdetector two types of sensors are used. The RASNIK system is used in all parts of the muon spectrometer, while the SaCam system is used only in the barrel and the BCAM system is used in both endcaps [58, 59].

2.3.1 *The* RASNIK *system*

The Red Alignment system NIKHEF (RASNIK) is the main alignment system for the ATLAS muon spectrometer [60]. It is a three-point straightness monitor, consisting of three components: a checkerboard mask, backlit by an infrared led through a diffusor, is projected onto a CCD sensor through a lens (see Figure 16). An infrared-passthrough filter is mounted in front of the CCD sensor to block any stray (visible) light.

By analyzing the size, position and angle of the checkerboard pattern projected onto the sensor, the relative position of the three components can be reconstructed. As only a small part of the mask is projected onto the sensor, the mask is coded such that software can identify the projected section. An example of the image created by a mask projected onto a sensor is shown in Figure 17.

Depending on the requirements of the system, the distance between the sensor and the mask can range from a few cm up to over 10 m. A RASNIK system with the lens halfway between the sensor and the mask has a resolution for off-axis translations of 1 µm. The magnification of the projected image, which is used to measure the position in the longitudinal direction, can be determined with a resolution of $2 \cdot 10^{-5}$.

2.3.2 *The SaCam system*

The Saclay Camera system (SaCam) is much alike the RASNIK system, but instead of a checkerboard mask a plate with four laser diodes is used (see Figure 18a). The camera and the lens are always mounted in the same housing, making this a two-point alignment system. Due to the large ratio of light source to lens and lens to sensor distances, this sensor is not very sensitive to translations, but much more so for rotations. The resolution for rotations of this system is 0.5 mrad, and the resolution for magnification is $5 \cdot 10^{-4}$.

2.3.3 *The BCAM system*

The housing of the Brandeis CCD Angular Monitor (BCAM) contains all three components: the sensor, the lens, and two laser diodes. Two BCAM housings facing eachother therefore compose two complete alignment systems facing in opposite directions, as shown in Figure 18b. Two BCAMs mounted in the same housing are used to create concatenated alignment lines. The intrinsic rotational resolution of this system is 50 µm. In practice this is limited by the precision of the BCAM mount. As the distances between the muon chambers in the endcaps are much larger than in the barrel, this system was designed to cover much larger distances than the SaCam.

2.3.4 *Barrel alignment*

The barrel MDT chambers are arranged into 16 *sectors* in ϕ, which follow the eightfold symmetry of the toroid magnet. Each of these sectors consists of three layers of 8 to 12 chambers. An overview of the chambers and the alignment systems three half-sectors in shown in Figure 19.

Chamber deformations are measured by *inplane* RASNIK systems. Four RASNIK systems are installed in every chamber (see Figure 20). Two sensors are mounted on a support bar on one side of the chamber, four lenses in holes in a support bar in the middle, and four masks on the support bar at the end opposite of the sensors. The sensors are shared by two lines. Switching the LEDs to illuminate only one of the two masks allows subsequent individual measurements for each line. Two holes are made in longitudinal support structures to allow the light of the diagonal lines to reach the sensors.

Some chambers[2], which are placed between the toroid magnet coils and the calorimeter and are therefore rather small, have only one inplane RASNIK system, as shown in Figure 21.

The *axial* and *praxial* systems measure the relative positions of all chambers in a sector. The axial RASNIK systems run along the short edges of multiple chambers, and can be seen in Figure 19. At all corners each chamber is connected to the corners of adjacent

2 These are the *barrel inner small* (BIS) chambers.

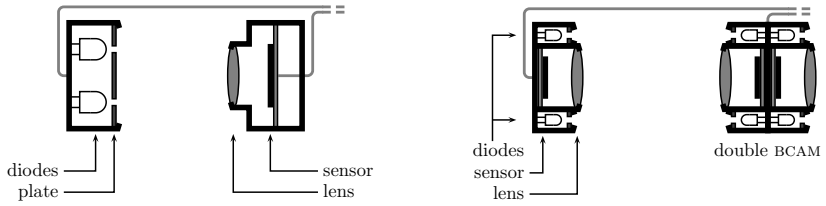

(a) SaCam: Light from four (two shown) laser diodes is projected onto a sensor.

(b) BCAM: two sensors face eachother. Multiple systems can be linked.

Figure 18: Schematic views of the SaCam and BCAM alignment sensors.

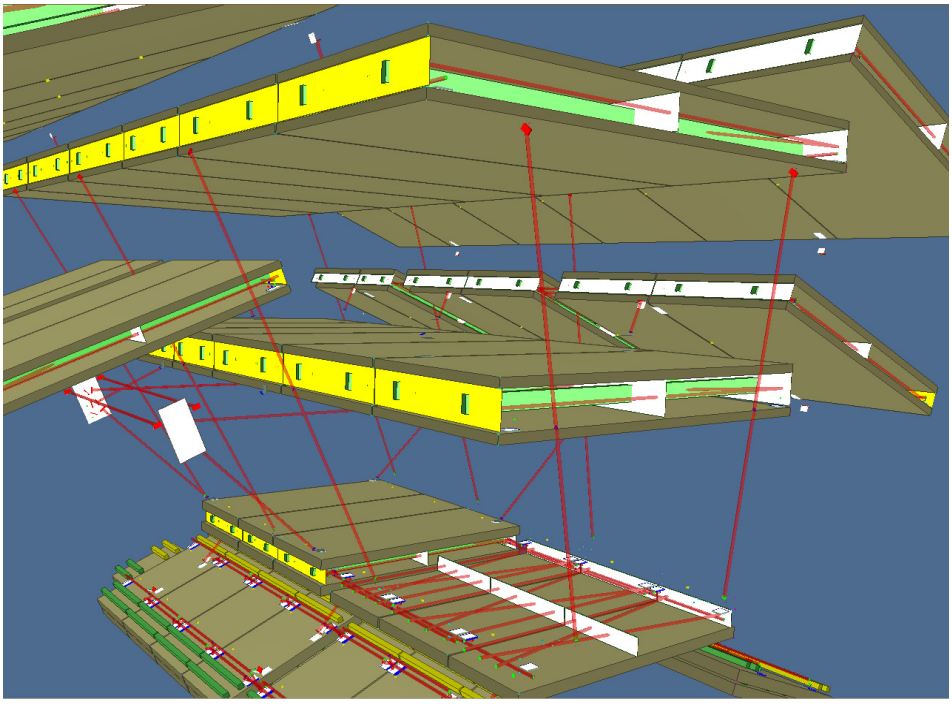

Figure 19: A computer generated view of a part of the ATLAS muon spectrometer barrel. The alignment systems are indicated with red lines.

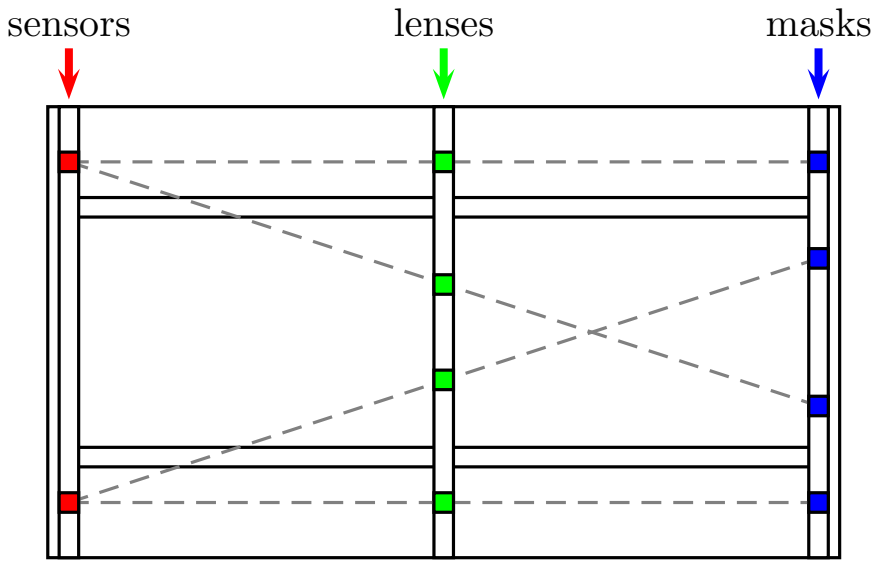

Figure 20: A schematic view of the inplane RASNIK alignment systems in barrel MDT chambers. Four optical lines are constructed using two sensors.

chambers with two crossing praxial RASNIK systems. These systems are very short (of the order of 10 cm), and have the sensor and lens built into one package, similar to the BCAM and SaCam systems.

The *projective* RASNIK systems connect the three layers of a sector. The mask is mounted on a chamber of the inner layer, while the lens and the sensor are mounted on chambers of the middle and outer layers respectively. The extrapolation of the optical axis of each projective line intersects with the interaction point, such that high-p_T muon tracks are parallel to these lines, maximizing their resolution in the relevant direction.

Projective systems are only mounted on the odd-numbered sectors, since the need to go through the middle layer of adjacent sectors complicates the design (see Figure 19).

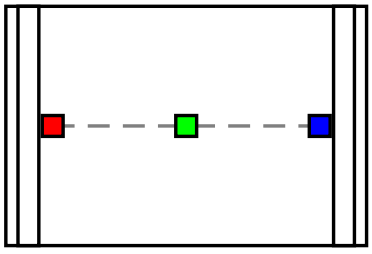

Figure 21: Layout of the inplane alignment RASNIK system on *barrel inner small* MDT chambers. The color coding is the same as in Figure 20.

The even-numbered sectors are aligned with respect to the odd-numbered sections via *chamber-to-chamber connections* (CCCS). These consist of a SaCam cameras mounted on the

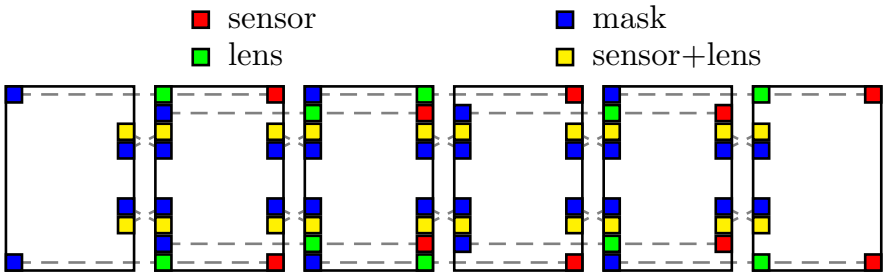

Figure 22: A schematic view of the axial and praxial RASNIK alignment systems along six barrel MDT chambers. Axial lines span two full chambers, while praxial lines only span the gap between two chambers.

on the even-numbered sectors looking at target spots on the odd-numbered sectors. Three CCCs on each side connect the inner and middle layers to the adjacent sectors, while only two CCCs per side do so for the outer layer.

An additional *reference* system of SaCams measures the position of the inner and middle layer chambers in odd-numbered sectors with respect to the barrel toroid in order to correct for higher order displacements. This reference system also monitors the position and deformation of the toroid coils with systems installed between to points on one coil or from coil to coil.

2.3.5 *Endcap alignment*

The muon spectrometer endcap consists of three *wheels*, disks covered with muon chambers. On each side, the inner wheel is mounted between the barrel toroid magnet and the endcap toroid magnet cryostat. The middle and outer wheels are mounted behind the endcap magnet.

As the endcap magnet cryostats are placed in between the inner and middle wheels projective lines like in the barrel can not be used in the endcaps. Instead, reference bars are aligned with bar-to-bar alignment systems, and chambers are aligned to these bars with chamber-to-bar alignment systems.

These reference bars are mounted throughout each wheel. The deformation of each alignment bar is monitored by in-bar RASNIK systems, and the positions of the bars with respect to eachother is measured by long-distance BCAM systems.

Similar to the alignment in the barrel, each MDT chamber in the endcap has four *inplane* RASNIK systems: two parallel to the tubes and two diagonally. The deformation of the CSCs is only measured prior to installation in the ATLAS detector. Proximity systems (RASNIKS) monitor the position of the MDT chambers and CSCs with respect to eachother and to the alignment bars.

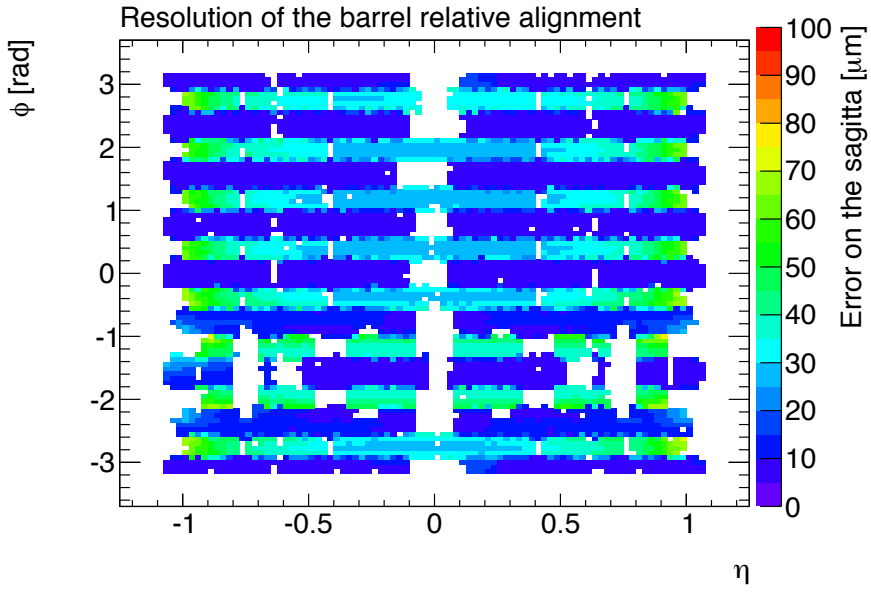

Figure 23: Resolution of the optical barrel alignment system. ATLAS work in progress [61].

2.3.6 *Alignment performance*

Figure 23 shows the performance of the barrel alignment system. The distinction between odd sectors (with projective alignment system) and the even sectors (without) is clearly visible, as the resolution in the latter is half an order of magnitude worse. Nevertheless, also in the even sectors the resolution is close to the requirement of 50 μm [61].

The resolution of the alignment in the endcaps is, due to the much larger distances, not as good as in the barrel. Where the average resolution in the barrel in 43 μm, it is 90 μm in the even sectors of the endcaps. Fortunately, this is not too far from the requirement to pose a large problem. Current work focuses on introducing nuisance parameters in the track fit to account for the misalignment of the muon chambers. The results of the track fitter on data can then be used to determine the alignment of the muon chambers.

2.4 TRIGGER

The ATLAS trigger system is designed to reduce the event rate from the interaction rate of 1 GHz to a rate of the order of 100 Hz, which can be written to disk. It is divided into three levels: the *level-1 trigger* [62], the *level-2 trigger* and the *event filter* [63]. Together the

level-2 trigger and the event filter make up the *high level trigger* (HLT), which make a more refined selection of the events that are selected by the level-1 trigger.

The level-1 trigger is hardware-based, which allows a much higher event rate but severely limits the number and complexity of the calculations which can be performed. Therefore only information from the calorimeter and the trigger chambers in the muon spectrometer is used. Objects triggered on by the level-1 trigger include high-p_T electrons, muons and photons, large E_T^{miss} and total transverse energy.

As shown in Figure 24 the events that are selected by the level-1 trigger are read into the *readout buffers* (ROBs) by *readout drivers* (RODs). The *derandomizers* placed after the level-1 trigger average out the incoming data rate to match the input rate of the RODs.

Event data is stored in the ROBs until the software-based level-2 trigger rejects the event or after it has been sent to the *event builder* for further processing. The level-1 trigger provides the level-2 trigger with a *region of interest* for each event. This includes information on high-p_T regions and E_T^{miss}. By using these regions of interest, it does not need to access the full event data.

The event filter has access to the complete selected events, and has sufficient calculation time to select events based on complex algorithms. It is designed to reduce the input event rate of the order of 1 kHz to a rate which can be written to disk, which is about 400 Hz for events of roughly 1 MB size.

The trigger uses a complex set (*menu*) of signatures, designed to identify objects, such as electrons, muons and jets, and the missing transverse energy, to select events based on the properties of these objects. Triggers can be prescaled in order to reduce their footprint in the total event rate. The events used in the analyses in this thesis, single top t-channel and Wt-channel events with one lepton, are selected by a trigger for isolated leptons. The trigger rate for true single top t-channel and Wt-channel events with one lepton was about 2 per minute in 2012.

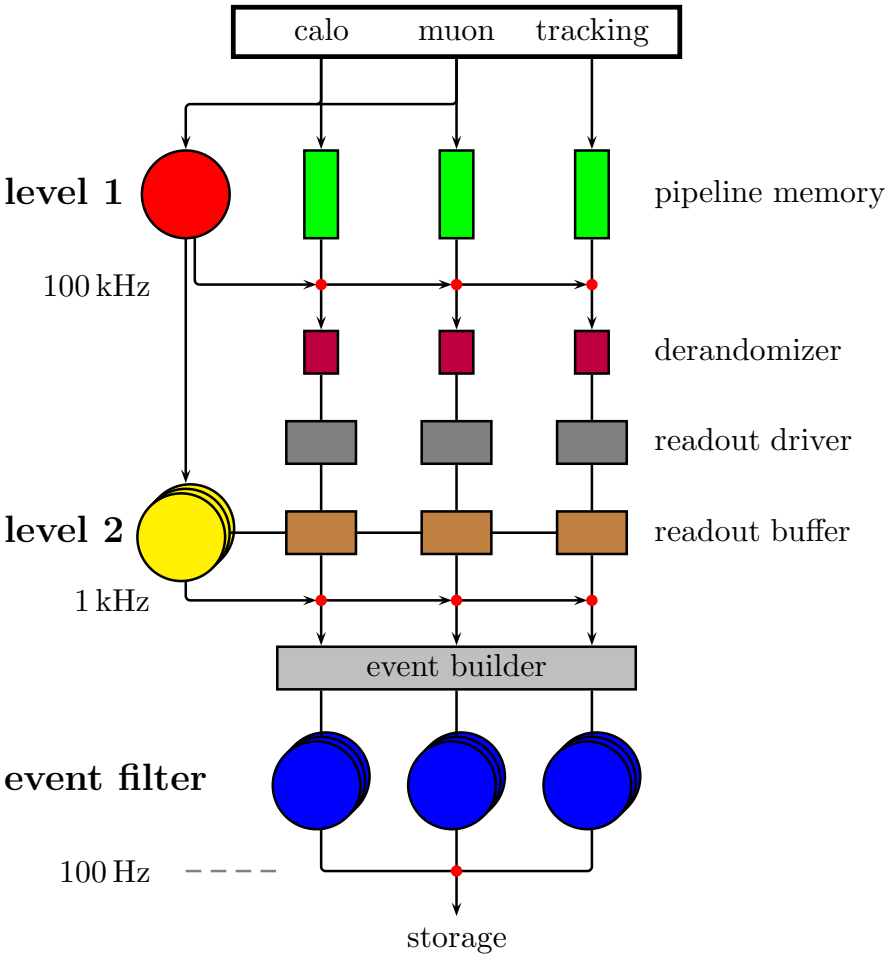

Figure 24: A block diagram of the data flow in the ATLAS trigger.

3

DATA, OBJECT RECONSTRUCTION AND SIMULATION

3.1 PERFORMANCE

The analyses described in this thesis make use of the proton-proton datasets recorded by ATLAS in 2011 and 2012. The physics conditions varied between and during these *runs*. The following subsections describe the conditions and the performance of ATLAS during the 2011 and 2012 proton-proton runs.

3.1.1 *Run conditions*

The data recorded during 2011 and 2012 are treated as distinct datasets. The analysis described in Chapter 4 uses the dataset recorded in 2011, for which the center-of-mass energy was $\sqrt{s} = 7$ TeV. The dataset recorded in 2012, for which the center-of-mass energy was $\sqrt{s} = 8$ TeV, is used in the analysis described in Chapter 6.

Figure 25 shows the integrated luminosity during the 2011 and 2012 runs. The instantaneous luminosity greatly increased from the 2011 to the 2012 run, yielding more than four times more usable data in 2012. The total luminosity used for physics is 4.57 fb^{-1} for the 2011 run and 20.3 fb^{-1} for the 2012 run.

Due to the very high instantaneous luminosity delivered by the LHC, multiple interactions occur per bunch crossing. The number of interactions per bunch crossing (also called *pile-up*) has increased more than twofold in the 2012 run with respect to the 2011 run. The distribution of pile-up is shown in figure 26.

3.1.2 *Detector performance*

As can be seen in Figure 25, not all delivered luminosity has been succesfully recorded. Table 6 shows the fraction of data recorded by each subsystem. With all subsystems combined, ATLAS has recorded almost 90% of all luminosity in 2011 and over 95% in 2012.

Also in data which is labelled "good", not all detector subsystems were fully working. In all subdetectors a small fraction of channels is inoperable, for various reasons. The fractions of *dead* channels are listed in Table 7. Fortunately, all these fractions are very low, and do not pose a serious problem to any analysis.

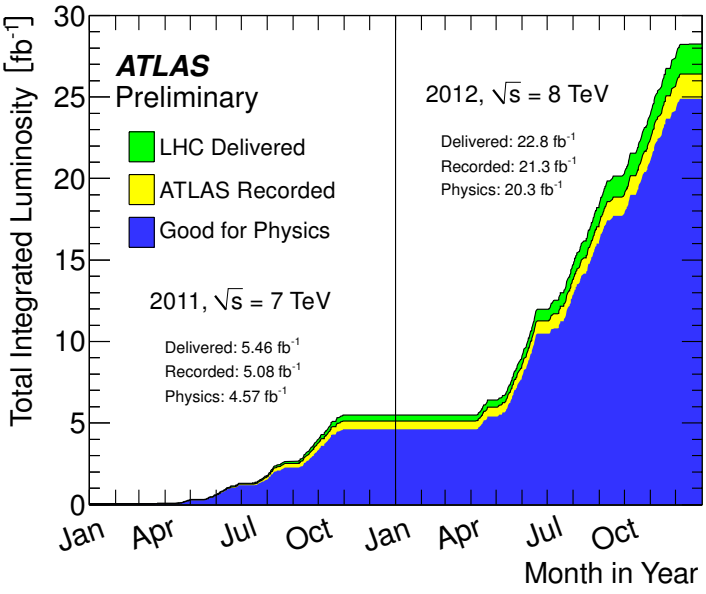

Figure 25: The total integrated luminosity as a function of time as delivered (green), recorded by ATLAS (yellow) and quality approved (blue) during the 2011 and 2012 runs.

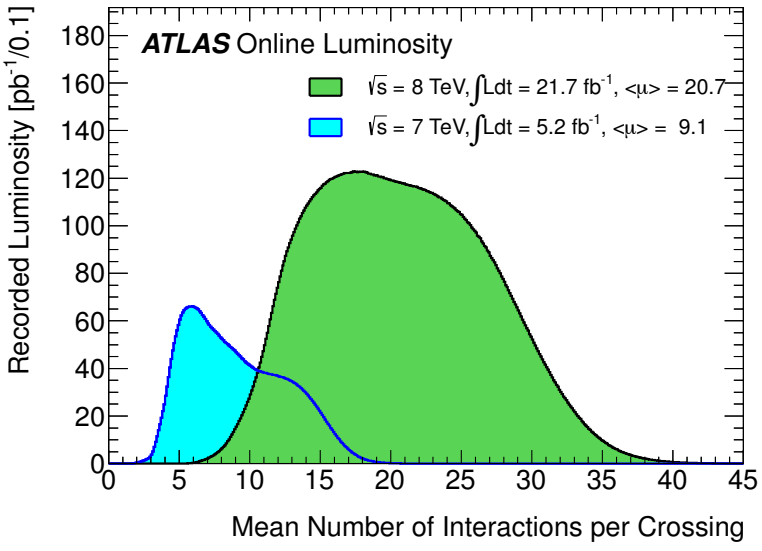

Figure 26: Luminosity-weighted distributions of the mean number of interactions per bunch crossing (pile-up) for the 2011 (blue) and 2012 (green) runs.

	Inner Tracker			Calorimeters		Muon Spectrometer				all
	pixel	SCT	TRT	LAr	tile	MDT	RPC	CSC	TGC	good
2011	0.998	0.996	0.992	0.969	0.992	0.994	0.988	0.994	0.991	0.898
2012	0.999	0.991	0.998	0.991	0.996	0.996	0.998	1.000	0.996	0.955

Table 6: Luminosity weighted fractions of good quality data recorded by the ATLAS subsystems and all subsystems combined for the 2011 and 2012 proton-proton runs [64].

	Inner Tracker			Calorimeters	
	pixel	SCT	TRT	LAr	tile
channels	$8 \cdot 10^7$	$6.3 \cdot 10^6$	$3.5 \cdot 10^5$	$1.8 \cdot 10^5$	$9.8 \cdot 10^3$
dead	0.050	0.007	0.025	0.001	0.017

(a) Inner tracker and calorimeters

	Muon Spectrometer			
	MDT	RPC	CSC	TGC
channels	$3.5 \cdot 10^5$	$3.7 \cdot 10^5$	$3.1 \cdot 10^4$	$3.2 \cdot 10^5$
dead	0.003	0.029	0.040	0.018

(b) Muon spectrometer

Table 7: Number of channels and fraction of dead channels for each ATLAS subdetector [65].

3.2 PHYSICS OBJECT RECONSTRUCTION

From the raw data that passes the event filter (see Section 2.4) physics objects are reconstructed. As many particles can be detected by several subdetectors, data from these subdetectors has to be combined into a single reconstructed object. The methods and algorithms for reconstructing these objects vary with the particle and the region of the detector where the particle was detected.

3.2.1 *Electrons*

Electron identification starts in the calorimeter [66]. In the central region of $|\eta| < 2.47$, energy deposits in the calorimeter are matched with a charged particle track from the inner detector. The distance between the extrapolated track and the deposit must be smaller than 0.05 in η and, depending on the direction of curvature, smaller than 0.05 or 0.1 in ϕ. If there are several tracks that match the cluster, the one with the smallest distance is chosen.

The direction of a central electron is determined by the direction of the matched track at the interaction point. The energy of the electron is determined by the energy deposit in the cluster.

Since there are no tracking detectors in the forward region ($2.5 < |\eta| < 4.9$), forward electrons are reconstructed using only the energy deposits in the calorimeter. The direction

of the electron is established by the center of the energy deposit, while the energy is determined by the total energy deposit in the cluster, corrected for energy losses in the path before the calorimeter.

Electron candidates are selected based on discriminating variables such as the track quality, the number of hits in the TRT and the deposited energy in the hadronic calorimeter. Three selections are made, each a subset of the next: *tight*, *medium* and *loose*[1]. Each selection is optimized in bins of $|\eta|$ and E_T. The efficiencies for identifying and reconstructing electrons with each selection are shown in Figure 27. These figures show that the reconstruction and identification efficiencies for loose electrons are very close to 100%, but that the efficiency for tight electrons is much lower. The agreement between data and MC is reasonable.

For the analyses described in this thesis the *tight* selection is used. This selection has a lower efficiency than the other selections, but has much lower fake rates [67, 68].

3.2.2 *Muons*

Muons are only reconstructed in the central region of $|\eta| < 2.7$, since the muon spectrometer does not extend beyond $|\eta| = 2.7$ (see Section 2.2.6) and muons can only be identified by the inner tracker or the muon spectrometer. Depending on what information on the muon is available, four types of muons can be reconstructed [69]:

- *Combined* (CB) muons, which are constructed by combining two independently reconstructed tracks from the inner tracker and the muon spectrometer.
- *Stand-Alone* (SA) muons, which are constructed using only a track in the muon spectrometer.
- *Segment-tagged* (ST) muons, which are constructed from a track in the inner tracker which matches a track segment in the muon spectrometer.
- *Calorimeter-tagged* (CaloTag) muons, which are constructed from a track in the inner tracker which matches an energy deposit in the calorimeter which is compatible with a minimum-ionizing particle.

Two *chains* that reconstruct muons exist in ATLAS: Staco [70] and Muid [71] (also called chain 1 and chain 2 respectively), which have very similar performance. For the 2012 data a third reconstruction chain has been developed, incorporating the best features of both chains.

The identification and reconstruction efficiencies are shown in Figure 28. One can clearly see the reduction in efficiency for very low $|\eta|$, where there is a gap in the coverage of the muon spectrometer. The CaloTag muons, which are reconstructed without the use the the muon spectrometer, suffer much less from this gap.

1 An additional selection called *multilepton* is made for the 2012 dataset, optimized for specialized analyses. Detailed information on this selection can be found in [67].

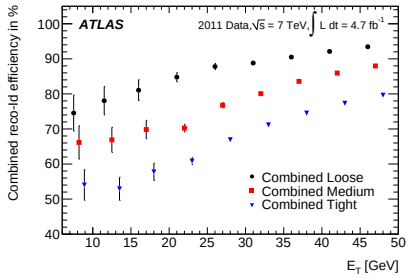

(a) Combined efficiency as a function of E_T for all selections in 2011.

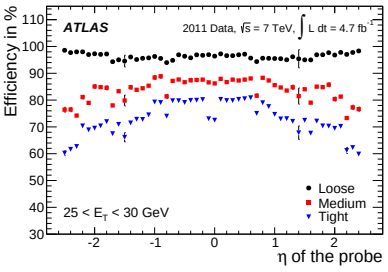

(b) Combined efficiency for electrons with $25 < E_T < 30\ GeV$ as a function of η for all selections in 2011.

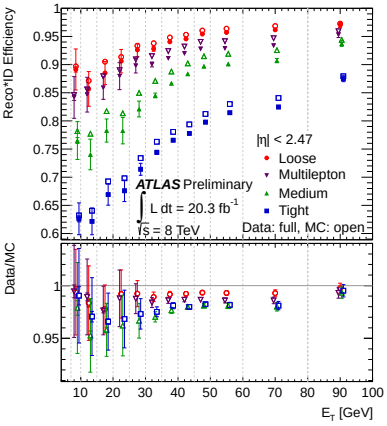

(c) Combined efficiency as a function of E_T for all selections in 2012, compared between monte carlo and data.

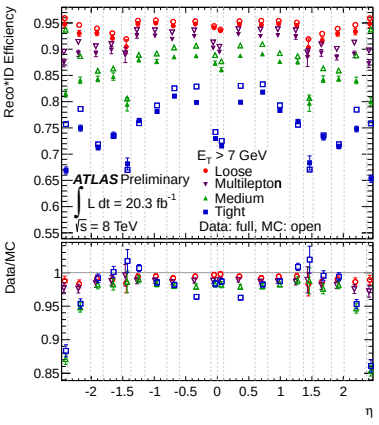

(d) Combined efficiency for electrons with $E_T > 7\ GeV$ as a function of η for all selections in 2012.

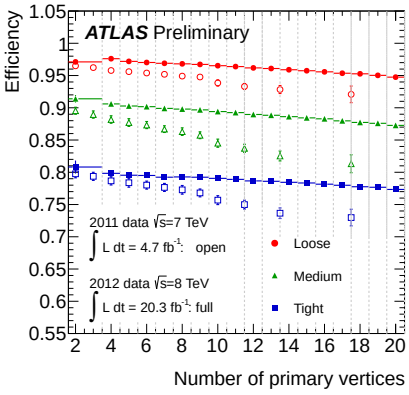

(e) Combined efficieny for all selections as a function of the number of primary vertices in the event in 2011 and 2012 data and monte carlo.

Figure 27: Electron reconstruction and identification efficiencies for 2011 and 2012 datasets.

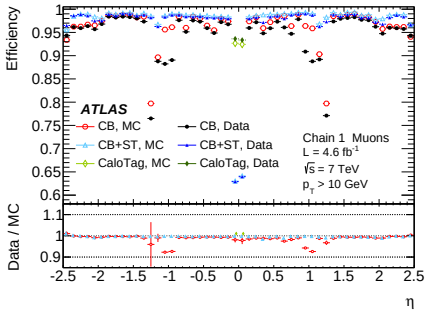

(a) Reconstruction efficiency of Staco (chain 1) during the 2011 datataking period.

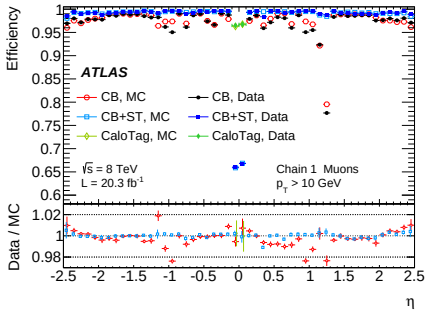

(b) Reconstruction efficiency of Staco (chain 1) during the 2012 datataking period.

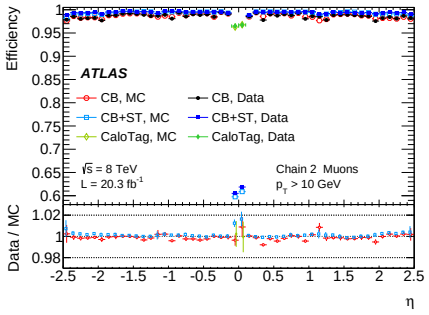

(c) Reconstruction efficiency of Muid (chain 2) during the 2012 datataking period.

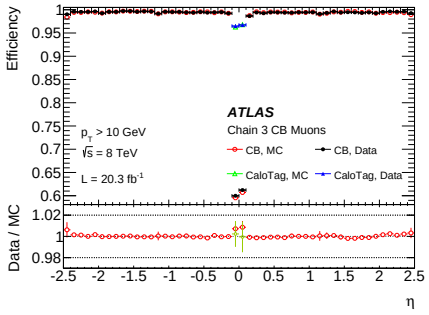

(d) Reconstruction efficiency of the third chain during the 2012 datataking period.

Figure 28: Reconstruction efficiency of muons as a function of rapidity. Figure a shows the efficiency during the 2011 run, while figures b through d show the efficiencies of all three chains during the 2012 run. The low efficiencies around $|\eta| = 1$ during the 2011 run are caused by missing muon chambers, which were installed after the 2011 run.

3.2.3 *Jets*

Jets in ATLAS are reconstructed using only data from the calorimeter. The clusters in the calorimeter are resolved using the anti-k_T algorithm [72], with a radius parameter of 0.4. This algorithm works well in the case of large numbers of soft jets.

The largest uncertainty in the reconstruction of jets is on the *jet energy scale* (JES), which is of the order of 5%, depending on the $p_T$of the jet. Figure 29a shows the JES uncertainty on 2011 data.

Several b-tagging algorithms, which try to distinguish light jets from b-jets, are deployed in ATLAS. The often used MV1 tagger is a neural network that combined the output of three other b-tagging algorithms [73]. Each b-tagging algorithm can be used at a multitude of working points, which define the efficiency and the mistagging rates of the tagger. A performance graph of the MV1 tagger is shown in Figure 29b.

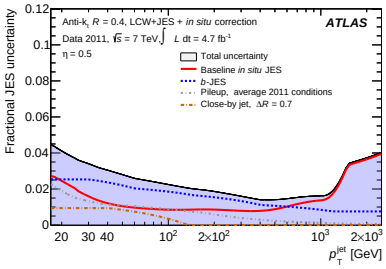

(a) Jet energy scale uncertainty as a function of p_T^{jet} for anti-k_T jets in 2011 data [74].

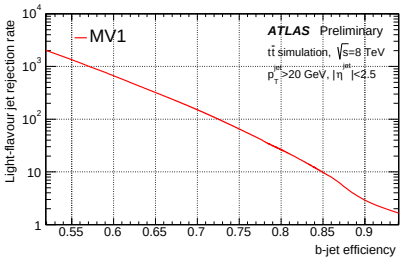

(b) Performance of the MV1 b-tagging algorithm on $\sqrt{s} = 8$ TeV simulation of $t\bar{t}$ events [75].

Figure 29: Jet energy scale uncertainty and b-tagging performance plots.

3.2.4 *Missing transverse energy*

The missing transverse energy (E_T^{miss}) has two contributions [76]. A calorimeter missing transverse energy is calculated using all energy deposits in the calorimeter. Low-$p_T$tracks from the inner detector are added if the particles are missing in the calorimeters.

The second contribution is the muon missing transverse energy, which is established using all muons detected in the muon spectrometer, and using tracks in the inner detector in regions where the muon spectrometer has no coverage.

The resolution of the E_T^{miss}, split up in components of E_x^{miss} and E_y^{miss}, where

$$E_T^{miss} = \sqrt{(E_x^{miss})^2 + (E_y^{miss})^2}, \tag{13}$$

as a function of the total transverse energy of an event is shown in Figure 30. For $\sqrt{s} =$ 8 TeV, several pile-up suppression techniques are applied to prevent the deterioration seen in E_T^{miss}resolution due to increasing pile-up [77].

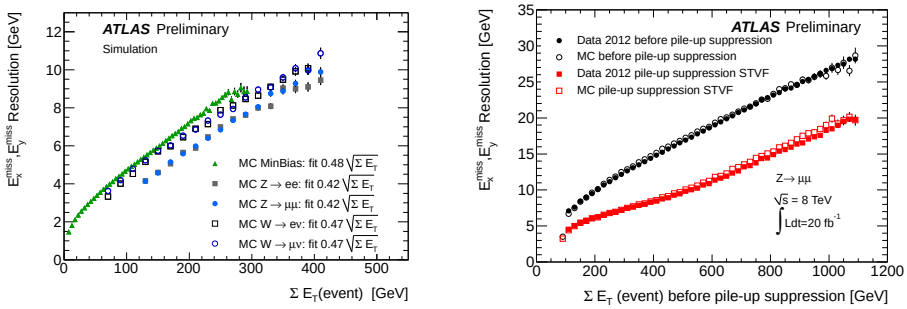

(a) Missing energy resolutions in monte carlo for $\sqrt{s} = 7$ TeV events.

(b) Missing energy resolutions in data and monte carlo for $\sqrt{s} = 8$ TeV events.

Figure 30: Resolution of E_x^{miss} and E_y^{miss} as a function of the total transverse energy of the event [77–79].

3.3 SIMULATION

In order to study the detector response for various physics processes, simulated *monte carlo* (MC) data samples are produced. The simulation process in ATLAS consists of three stages [80], each of which will be briefly discussed in the following subsections.

3.3.1 *Generation*

An event generator uses a matrix element (or a set of matrix elements) to produce complete events starting from a proton-proton (or nucleon-nucleon) initial state. Event generators also handle immediate decays, such as decays of top quarks, and hadronization. The output is a tree of all particles and their decay products.

Many event generators are used in ATLAS, including PYTHIA [81], HERWIG [82], Sherpa [83], Powheg [84], Alpgen [85], MC@NLO [86] MadGraph [87] and AcerMC [88]. The PYTHIA and HERWIG generators are the benchmark generators of ATLAS, to which all other generators are compared. While both PYTHIA and HERWIG have new versions written in C++, older well-tested versions (PYTHIA 6.4 and HERWIG 6.5) written in the very old FORTRAN77 language are used.

Powheg, Alpgen, AcerMC, MadGraph and MC@NLO generate only the matrix element interaction, and write out the result in the *Les Houches* format [89], leaving the decay and hadronization to for example PYTHIA or HERWIG. Each of these generators targets a specific type of processes: Alpgen specializes in final states with several well-separated jets, AcerMC is designed for producing events with W or Z bosons with several jets, and Powheg and MC@NLO generate hard scattering events at next to leading order.

Sherpa is expected to perform better for events with large numbers of isolated jets in the final state and interfaces with PYTHIA's hadronization model, making it a complete generator.

While many of these generators generate the matrix element at leading order, some generators include one-loop corrections. Powheg and MC@NLO are examples of such next-to-leading order generators.

In the generation process *parton density functions* (PDFs) are used to approximate the structure of the protons. ATLAS uses the LHAPDF [90] library of PDFs, from which the QTEC [91] PDFs are default. An alternative set op PDFs is the HeraPDF library [92].

3.3.2 *Detector simulation*

The output of the event generator is fed into the detector simulation, which simulates the interactions of the particles with the detector, tracking their propagation through the detector. The simulation is done by GEANT4 [93], for which a very detailed model describing the detector has been made. This model contains over 300 000 individual volumes, more than half of which belong to the calorimeters.

Energy deposits in the sensitive regions of the detectors, called *hits*, are stored as output, together with the time and place coordinates of the deposit.

The vertex position of the generated collision is not always placed in the exact center of the detector: the vertices are smeared according to the ideal luminous region of the LHC in ATLAS, and can be rotated in ϕ in order to produce a more accurate approximation of reality.

3.3.3 *Digitization*

The response of the detector is simulated in the digitization step. The voltage on each readout channel is calculated, taking into account noise, cross-talk, and channel-dependent variation such as dead channels. The simulated detector output is then fed into the triggering and reconstruction algorithms that are also used for data. The result is a file with simulated events in a format similar to the data files.

Pile-up In order to simulate pile-up, hits of simulated signal events are combined with background events, such as minimum bias, cavern background, and beam halo. The number of events per simulated bunch crossing is varied according to the distribution of pile-up in data.

3.3.4 *Truth*

The generated events, before hadronization and shower, are stored together with the results of the entire simulation process, and are called *(monte carlo) truth*. This truth information is useful for studies targeting the detector response, for example in *folding* or *unfolding* (see Section 6.3).

3.3.5 *Fast simulations*

The detector simulation method described above is very compute-intensive, taking on average over half an hour per $t\bar{t}$ event [94]. By far the largest fraction ($\approx 95\%$) of time is spent in the simulation of the calorimeter.

atlfast I This first fast simulation does not provide any realistic detector description, making detector performance studies impossible. Any simulated track is passed on as reconstructed object, bypassing object reconstruction. Therefore misreconstruction effiencies are not modeled, and only fake b-jets and taus are modeled by applying jet flavor tagging effiencies.

atlfast II In contrast to ATLFAST I, the second fast simulation simulates all properties of a track using parametrizations obtained with the full simulation, and produces hits which are passed on to the reconstruction algoritms. This has the advantage that the final simulation output has the same format as that of the full simulation, and monte carlo sets generated by the two methods can therefore be used together in one analysis.

Fast G4 simulation A GEANT4 simulation which only treats electromagnetic showers in the sensitive regions of the calorimeter reduces the required computing time by a factor of three, without sacrificing effiency. As the output format is exactly the same as that of the full simulation, it too can be used together with full simulation and ATLFAST II monte carlo sets.

4

SEARCH FOR SINGLE EXCITED B QUARK PRODUCTION

This chapter describes a search [95, 96] for excited b quarks (b^*) decaying to a W boson and a top quark as described in section 1.3. The analysis uses 4.7 ± 0.2 fb^{-1} of data recorded by ATLAS during the 2011 run with $\sqrt{s} = 7$ TeV/c^2 [97]. Since this analysis is similar to the analysis described in the next chapter, the description of some details of this analysis is concise.

4.1 DATA AND MONTE CARLO

Contributions from background processes and acceptances of the signal process are calculated from MC samples processed with the full detector simulation (see section 3.3.2).

The signal samples were generated at tree-level using MadGraph5 and decay and hadronization was handled by PYTHIA using only a left-handed coupling for production and decay. A total of twelve signal samples are used, each with a different mass for the b^* quark ranging from $m_{b^*} = 300$ GeV/c^2 to $m_{b^*} = 1400$ GeV/c^2 in steps of 100 GeV/c^2. The production cross section of the b^* quark is mass dependent, and the used cross sections are listed in table 8.

b^* mass	cross section	b^* mass	cross section
300 GeV/c^2	181.2 pb	900 GeV/c^2	0.804 pb
400 GeV/c^2	69.2 pb	1000 GeV/c^2	0.394 pb
500 GeV/c^2	24.5 pb	1100 GeV/c^2	0.201 pb
600 GeV/c^2	9.37 pb	1200 GeV/c^2	0.106 pb
700 GeV/c^2	3.88 pb	1300 GeV/c^2	0.057 pb
800 GeV/c^2	1.72 pb	1400 GeV/c^2	0.032 pb

Table 8: Total cross section of $b^* \to Wt$ for each generated b^* quark mass.

The t-channel background sample was generated with AcerMC and for the other top backgrounds (Wt-channel, s-channel and $t\bar{t}$) MC@NLO was used. The W+jets and Z+jets samples were generated using Alpgen, and diboson samples for WW, WZ and ZZ were generated by HERWIG.

4.2 OBJECT SELECTION

In this analysis several types of objects were used. The definitions of these objects are briefly discussed here. More details can be found in [95], and performance studies can be found in [98].

Electrons are required to pass the tight[1] selection criteria and to have $p_T > 25$ GeV/c and $|\eta| < 1.37$ or $1.52 < |\eta| < 2.47$. Backgrounds from fake electrons and electrons from heavy-flavor decays are suppressed using isolation criteria in a cone around the electron.

Combined[1] muons with $p_T > 25$ GeV/c and $|\eta| < 2.5$ are used. As with electrons, muons from heavy-flavor decays are suppressed using isolation criteria in a cone around the muon.

Jets are reconstructed using the anti-k_T algorithm[1], and only jets with $p_T > 25$ GeV/c and $|\eta| < 2.5$ are used. In order to reject jets from pile-up events, at least 75% of the tracks associated to a jet must be compatible with originating from the primary vertex[2]. The MV1 tagger[1] with an efficiency of 70% is used to identify b-jets.

For the estimation of the QCD multijet background a loose selection is used, which is equivalent to the medium[1] selection criteria for electrons, and looser isolation requirements for both electrons and muons.

4.3 EVENT SELECTION

Two levels of event selection are used in this analysis. First a *preselection* is applied to select events which have a single-lepton $b^* \to Wt$ signature. The W+jets and the QCD multijet backgrounds are estimated at this level. A second *selection* is then used to isolate the signal.

PRESELECTION Several event quality criteria are applied in the preselection in order to remove ill-reconstructed events and events with jets near a hole in the calorimeter coverage in the region of $\eta \in [-0.1, 1.5]$ and $\phi \in [-0.9, -0.5]$. As shown in table 9, each event is required to have either one electron or one muon with $p_T > 25$ GeV/c, and the E_T^{miss} requirement depends on the flavor of the lepton. Furthermore at least two jets, of which one is b-tagged, are required.

A special requirement is introduced in order to reduce the number of QCD multijet background events by using the fact that these events have on average a low E_T^{miss} and low transverse W mass ($M_T(W)$), which is defined as

$$M_T(W) = \sqrt{\frac{2}{c^3} E_T^{miss} p_T^{\ell} \left(1 - \cos\left(\Delta\phi\left(E_T^{miss}, p_T^{\ell}\right)\right)\right)}, \tag{14}$$

where p_T^{ℓ} is the transverse momentum of the lepton.

SELECTION The selection adds one more requirement: each event is required to have exactly 3 jets (of which one b-tagged). The 3-jet channel is a compromise between the 2-jet channel where the W+jets background is dominant and the 4-jet channel where the $t\bar{t}$ background is dominant.

1 See section 3.2 for more details.
2 In other words, a *jet vertex fraction* cut of 0.75 is applied.

1 electron
0 muons
$E_T^{miss} > 30$ GeV
$\geqslant$ 2 jets
1 b-jet
$M_T(W) > 30$ GeV/c^2

(a) Electron channel.

1 muon
0 electrons
$E_T^{miss} > 25$ GeV
$\geqslant$ 2 jets
1 b-jet
$M_T(W) + E_T^{miss}/c^2 > 60$ GeV/c^2

(b) Muon channel.

Table 9: Preselection cuts defining the electron and muon channels. Only cuts 4 and 5 are the same between the channels. In addition to the cuts presented here several event quality cuts are made in order to remove ill-reconstructed events. The selection defines one more cut, requiring the number of jets to be equal to 3.

4.4 BACKGROUND ESTIMATION

The QCD multijet and W+jets backgrounds are not well modeled by MC and their yields have a large uncertainty [99]. The rate and shape of the QCD multijet and W+jets backgrounds are determined using data-driven methods. The methods described here are described in more detail in [100].

4.4.1 *Estimation of the QCD multijet background*

The matrix method [98] is used to estimate the QCD multijet background. The number of QCD multijet one-lepton events in the selection is estimated as

$$N_{fake}^{tight} = \frac{\epsilon_{fake}}{\epsilon_{real} - \epsilon_{fake}} \left(\epsilon_{real} N^{loose} - N^{tight} \right), \tag{15}$$

where N^{tight} and N^{loose} are the event yields from data in the tight and loose selections, ϵ_{real} and ϵ_{fake} are the selection efficiencies from the loose to the tight selection for signal electrons and fake electrons respectively. These efficiencies are determined using control samples.

The resulting QCD multijet event yields are shown in table 10. For the final analysis an uncertainty of 50% is assigned to these numbers.

	electron		muon	
jet bin	event yield	fraction	event yield	fraction
2-jet	4402±1637	15.0%	3757±256	8.3%
3-jet	2177±751	13.6%	1303±122	5.8%
4-jet	855±331	11.0%	386±58	3.5%

Table 10: Estimate of the QCD multijet background for events passing the preselection per jet-bin and the fraction of the total background the QCD multijet background constitutes. The uncertainties are derived from the matrix method.

jet-bin	κ_{bb}	κ_c	κ_{ll}
1	1.23	0.72	0.99
2	1.11	0.65	0.90
3	0.99	0.58	0.80
4	1.01	0.59	0.82

(a) Electron channel.

jet-bin	κ_{bb}	κ_c	κ_{ll}
1	1.43	0.99	1.01
2	1.30	0.89	0.91
3	1.18	0.81	0.83
4	1.24	0.85	0.87

(b) Muon channel.

Table 11: Correction factors for W+jets as determined with the tag counting method, including the corrections for the flavors fractions as well as the absolute normalization.

4.4.2 *Estimation of the W+jets background*

To estimate the W+jets background several MC samples are used: W+jets are categorized into *light flavor* (events with only up, down and strange quarks), and *heavy flavor* (events which contain at least one charm or bottom quark). The heavy flavor is split up in W_{cc}, W_{bb} and W_c samples which contain events with at least two charm or bottom quarks and one charm quark respectively. The uncertainty on the normalization of the W+jets background is 20%, and the relative normalizations of the subsamples (called heavy flavor fractions) are subject to large uncertainties, up to 100%.

The flavor fractions are determined using a tag-counting method [98], which uses two data samples: the preselected data with the b-tag requirement removed (called the *pretag* sample) and the normal preselected sample (called the *tag* sample). Both samples are dominated by background. The flavor fractions add up to unity: $F_{bb} + F_{cc} + F_c + F_{ll} = 1$, and since the W_{bb} and W_{cc} samples are expected to behave similarly the ratio of F_{bb} and F_{cc} is determined from MC. Two additional equations, one for each lepton charge, allow for solving for the flavor fractions:

$$N^{tag,\pm} = N^{pretag,\pm} \sum_{x\in\{bb,cc,c,ll\}} F_x P_x, \tag{16}$$

where $N^{tag,\pm}$ and $N^{pretag,\pm}$ are the number of W+jets events in the tag and pretag sample for each lepton charge, and P_x are the probabilities that an event from sample x is b-tagged, as found from MC. One set of equations is solved for each jet bin and each lepton flavor, and correction factors $\kappa_x = F_x/F_x^{MC}$ are calculated yielding the set of correction factors as shown in table 11. Since the preselected samples are dominated by background and since the signal is charge-symmetric, the signal does not bias the calculation of the correction factors.

The absolute normalization of the W+jets background is done making use of the charge asymmetry of this sample. As the total charge asymmetry is dominated by W+jets processes, we can find the total number of W+jets events as

$$N = N_+ + N_- = \left(\frac{N_+^{MC} + N_-^{MC}}{N_+^{MC} - N_-^{MC}}\right)(N_+ - N_-), \tag{17}$$

where $(N_+ - N_-)$ is the charge asymmetry in data, and the normalization of MC is extracted by writing the fraction in equation 17 as $(r^{MC}+1)/(r^{MC}-1)$, where r^{MC} is the ratio of positive to negative W+jets events in MC, which is known to be well modeled.

	electron	muon
Wt-channel	709±9	962±10
s,t-channel	823±6	1137±8
$t\bar{t}$	6599±30	9085±36
W+jets	1140±73	2011±86
W+jets HF	3757±47	7129±73
Z+jets	135±2	192±3
diboson	646±15	606±17
QCD multijet	2177±1089	1303±652
total expected	15978±1093	22425±663
data	15477	22698

Table 12: Event yields for the background samples in the selection compared to data. All shown uncertainties are statistical except for the uncertainty on the QCD multijet sample, which is 50% by assignment.

The event yields for the selection, with the W+jets normalization and flavor fractions applied, are shown in table 12.

4.5 SYSTEMATIC UNCERTAINTIES

The systematic uncertainties are evaluated by repeating the analysis with one or more sample(s) representing a variation of the source of each of these uncertainties. The W+jets flavor factions and normalization are recalculated for each variation, and thus the uncertainty of this method is included in the results. The results include systematic uncertainties evaluated on:

- lepton energy scale and resolution,
- lepton trigger and identification scale factors,
- jet energy scale and resolution,
- jet reconstruction efficiency,
- jet vertex fraction scale factors,
- effects of soft jets and pile-up on missing transverse energy,
- b-tagging scale factors for bottom, charm and light jets,
- MC generators,
- parton shower modeling,
- initial and final state radiation,

- background cross section normalizations,
- QCD multijet background normalization,
- luminosity, and
- W+jets background shape and normalization.

All systematic uncertainties involving normalizations, scale factors or efficiencies are evaluated by varying the normalization of the relevant (sub-)samples up and down. For the background cross section normalization uncertainties, the normalization of only one background is changed at a time. The variations per sample are shown in table 13.

The MC generator and parton shower modeling uncertainties are evaluated by comparing MC@NLO and Powheg as generator and Powheg combined with either PYTHIA or HERWIG for particle decay and hadronization on the $t\bar{t}$ background. Initial and final state radiation uncertainties are estimated using signal and $t\bar{t}$ samples generated by AcerMC and PYTHIA with varied parameters for initial and final state radiation. The W+jets shape uncertainty is evaluated by varying generator parameters.

In order to give an idea of their size, the effects of the systematic variations on the event yields are shown in table 14. Systematic variations which do not change the yields (e.g. the W+jets shape systematic) are not shown. The total uncertainty from these sources is $+13\%$ and -12%. The jet energy scale systematic consists of 12 components which are evaluated separately [101]. The effects of each component on the event yields is shown in table 15. The largest component is introduced by the pile-up (μ) offset term, and the total uncertainty arising from the jet energy scale is $+6\%$ and -3%.

4.6 ANALYSIS

This analysis uses the *total invariant mass*, calculated by combining the four-momenta of the three jets, the lepton and the E_T^{miss} (of which the z-component is zero by definition) and taking the invariant mass, as discriminating variable. Other variables were also studied, including the transverse momenta of the lepton and the jets, the pseudorapidity of the lepton, the E_T^{miss}, angular correlations of jets and the lepton and the centrality of the event. The total invariant mass was found to be the best discriminator between signal

	variation	
cross section uncertainty	up	down
Wt-channel	$+8\%$	-8%
s-channel	$+8\%$	-8%
t-channel	$+8\%$	-8%
$t\bar{t}$	$+10\%$	-10%
Z+jets	$+60\%$	-60%
diboson	$+5\%$	-5%

Table 13: Used cross section variations per sample.

	effect	
systematic uncertainty	up	down
luminosity	+0.98%	−0.98%
jet energy scale	+5.98%	−2.91%
jet energy resolution	+3.92%	−3.92%
jet reconstruction	+0.88%	−0.88%
jet vertex fraction	−1.52%	+1.30%
b-tag rate	+0.17%	−0.72%
c-tag rate	+2.57%	−2.63%
mistag rate	+2.22%	−2.24%
electron energy scale	+0.40%	+0.09%
electron energy resolution	+0.30%	+0.32%
muon energy scale	+0.54%	−0.54%
muon energy resolution	+1.96%	−1.96%
lepton identification	+1.75%	−1.75%
E_T^{miss} soft jet	+0.42%	+0.25%
E_T^{miss} pile-up	+0.36%	+0.29%
MC generator	+1.83%	−1.83%
parton shower modeling	+1.40%	−1.40%
initial/final state radiation	+1.70%	−1.70%
background cross section	+6.84%	−6.84%
QCD multijet normalization	+4.53%	−4.53%
W+jets normalization	+4.88%	−4.69%

Table 14: Effect of systematic variations on the number of expected background events.

	effect	
jet energy scale component	up	down
μ offset term	+0.60%	−1.02%
number of primary vertices offset term	−0.87%	+0.24%
effective component 1	+1.06%	−0.27%
effective component 2	+0.35%	−0.97%
effective component 3	+0.41%	+0.24%
effective component 4	+0.34%	+0.34%
effective component 5	+0.32%	+0.39%
effective component 6	+0.43%	+0.17%
η intercalibration (statistical)	−0.97%	+0.10%
η intercalibration (generator)	−0.20%	−0.48%
high p_T term	−1.09%	−0.48%
closure of the calibration	+0.38%	+0.33%
combined	+5.98%	−2.91%

Table 15: Effect of the jet energy scale systematic components on the number of expected background events.

and background. The distributions of a few of the abovementioned variables are shown in figure 31. and figure 32 shows the distribution of the total invariant mass. These distributions show good data-MC agreement, but also show that both the *W*t-channel and the signal are overwhelmed by background.

A b^* signal with a mass of 800 GeV/c^2 is shown on top of the total invariant mass distribution in figure 32. As the momenta of all decay products of the b^* quark are summed in the calculation of this variable (except for the z-component of the neutrino momentum), it is very similar to the mass of the b^* itself, resulting in a peak around a mass of 800 GeV/c^2. This gives a very good separation of signal and background which is especially good for high b^* masses.

The availability of this distribution is an advantage of using the 3-jet bin. In the 2-jet bin the separation in the distribution is less well defined as the information of one decay product is missing, while in the 4-jet bin there is the ambiguity of whether to exclude one jet from the calculation of the total invariant mass (and in this case which jet to exclude) or to assume that all jets originate from the decay products and to include all four jets in the calculation.

4.6.1 *Template fitting*

A template shape fitting method is used to set limits on the cross section as a function of the mass of the b^* in absense of any signal. This method is, in effect, a counting

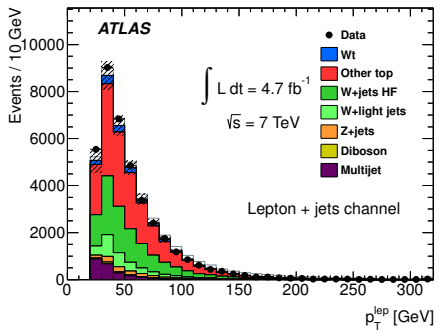

(a) Transverse lepton momentum.

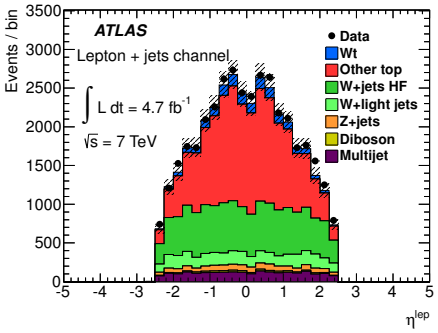

(b) Lepton pseudorapidity.

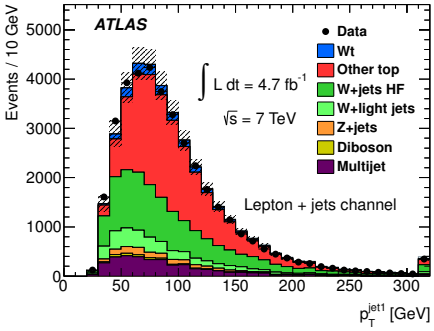

(c) Transverse momentum of first jet.

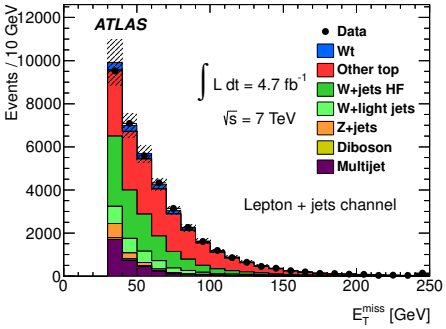

(d) Missing transverse energy.

Figure 31: Control distributions of selected events.

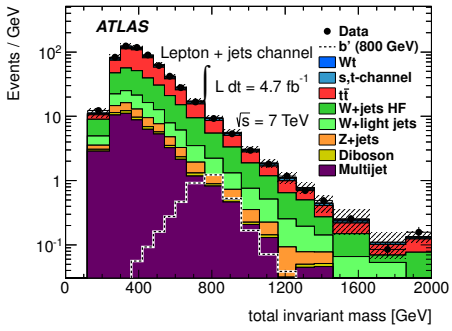

Figure 32: Distribution of the total invariant mass of selected events.

experiment in many bins of the total invariant mass distribution. A likelihood function is defined as the product of single-bin counting experiments:

$$\mathcal{L}(data|\sigma_{b^*},\theta_i) = \prod_{k=1}^{N_{bin}} \frac{\mu_k^{n_k} e^{-\mu_k}}{n_k!} \prod_{i=1}^{N_{sys}} G(\theta_i,0,1), \tag{18}$$

where $\mu_k = s_k + b_k$ is the sum of expected signal and background yields, n_k is the observed yield, and $G(\theta_i,0,1)$ is the Gaussian prior for the i^{th} systematic uncertainty with nuisance parameter θ_i. A flat prior is assumed for the signal cross section: $\pi(\sigma_{b^*}) = 1$. The likelihood function is reduced by integrating over all nuisance parameters:

$$\mathcal{L}(data|\sigma_{b^*}) = \int \mathcal{L}(data|\sigma_{b^*},\theta_i)d\theta_i, \tag{19}$$

and upper limits on σ_{b^*} are set at 95% credibility level (CL) for each b^* mass in table 8 using the Bayesian Analysis Toolkit [102].

4.7 RESULTS

Using the template fitting method a range of upper limits in the b^* cross section is obtained. These results are shown in figure 33 with only the statistical uncertainty as well as with both the statistical and systematic uncertainties included. The b^* process can be excluded up to 95% CL in range where the observed cross section upper limit is below the theory prediction. The intersection of the observed (expected) cross section upper limit and the theory prediction defines the observed (expected) b^* mass limit.

The observed mass limit for couplings $\kappa_L^{b^*} = g_L = 1$ and $\kappa_R^{b^*} = g_R = 0$, with only the statistical uncertainty included, is

$$m_{b^*} = 1057 \text{ GeV}/c^2, \tag{20}$$

below which the b^* is excluded, and where $m_{b^*} = 963$ GeV/c^2 was expected. With also the systematic uncertainties included, the observed mass limit becomes

$$m_{b^*} = 803 \text{ GeV}/c^2, \tag{21}$$

where $m_{b^*} = 834$ GeV/c^2 was expected. The limits have also been calculated as a function of couplings $\kappa_L^{b^*}$ and g_L, while keeping $\kappa_R^{b^*} = g_R = 0$. The results are shown in figure 34.

4.8 COMBINATION

This analysis was combined with the analysis described in [103], which focuses on the dilepton signature of $b^* \to Wt$ and requires two leptons in the event selection, in contrast to the analysis described above, which focuses on the single lepton signature. As a result of the different number of required leptons, these analyses are orthogonal.

Since the dilepton analysis uses events with two leptons, and hence two neutrinos, the top mass can not be reconstructed. Therefore the H_T-distribution is used as discriminating variable. For the combination, all bins of both discrimination distributions, the reconstructed top mass distribution for the single lepton analysis and the H_T-distribution for the dilepton analysis, are used in the construction of the likelihood.

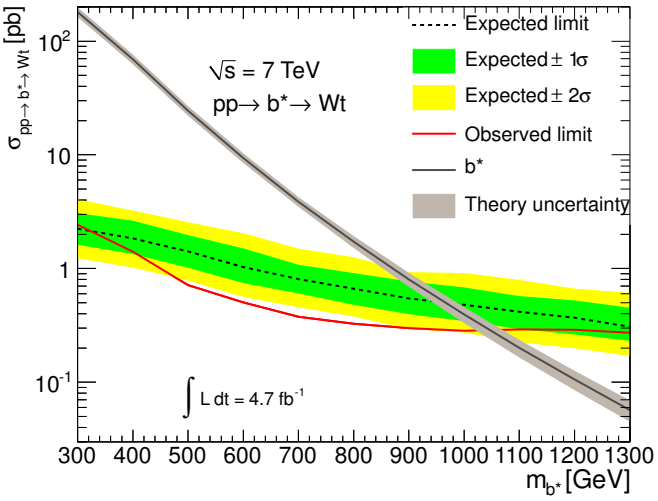

(a) Cross section limits with only statistical uncertainties.

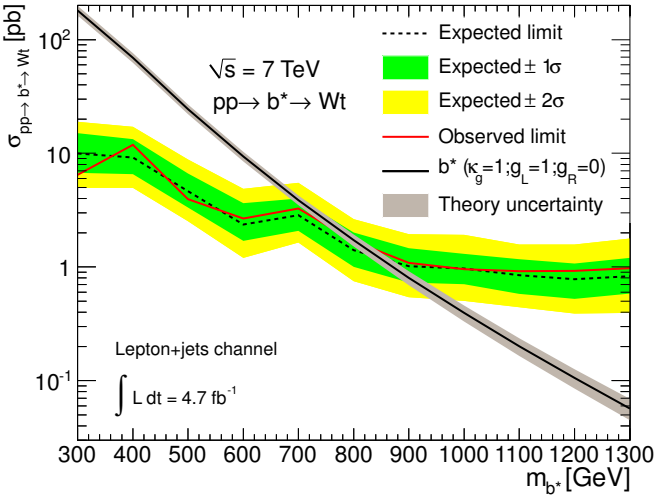

(b) Cross section limits with statistical and systematic uncertainties.

Figure 33: Cross section limits for $b^* \to Wt$ as a function of the b^* mass, with only statistical uncertainties included (figure a) and with both statistical and systematic uncertainties included (figure b). Shown are the theoretically predicted cross section for couplings $\kappa_L^{b^*} = g_L = 1$ and $\kappa_R^{b^*} = g_R = 0$ (in black, with grey uncertainty band), the expected upper limit in the case that no signal is present (dashed, with 1 and 2σ uncertainty bands) and the observed limit (in red).

The results of this combination are shown in figure 35. For only left-handed couplings ($\kappa_L^{b^*} = g_L = 1$ and $\kappa_R^{b^*} = g_R = 0$), the b^* mass limit is observed to be

$$m_{b^*} = 870 \text{ GeV}/c^2, \tag{22}$$

where $m_{b^*} = 910 \text{ GeV}/c^2$ was expected. This is an improvement over the result of the single lepton analysis alone.

Limits have also been calculated for scenarios with right-handed couplings. These limits can be found in [96].

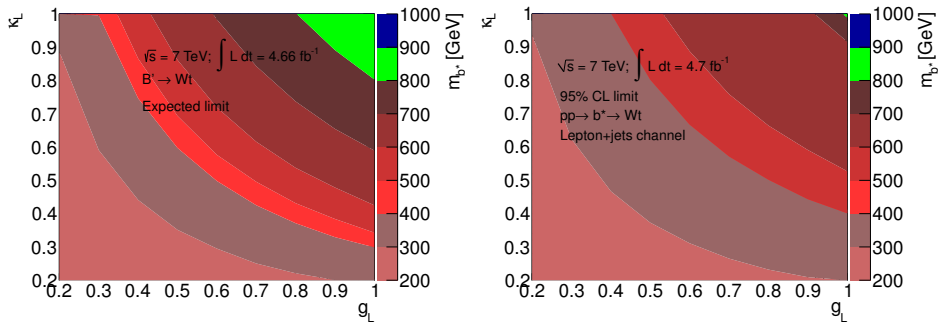

(a) Expected limit.

(b) Observed limit.

Figure 34: Cross section limits for $b^* \to Wt$ as a function of the b^* mass and the couplings κ_L and g_L with statistical and systematic uncertainties included. The b^* signal can be excluded at 95% CL along the contour line of a certain mass.

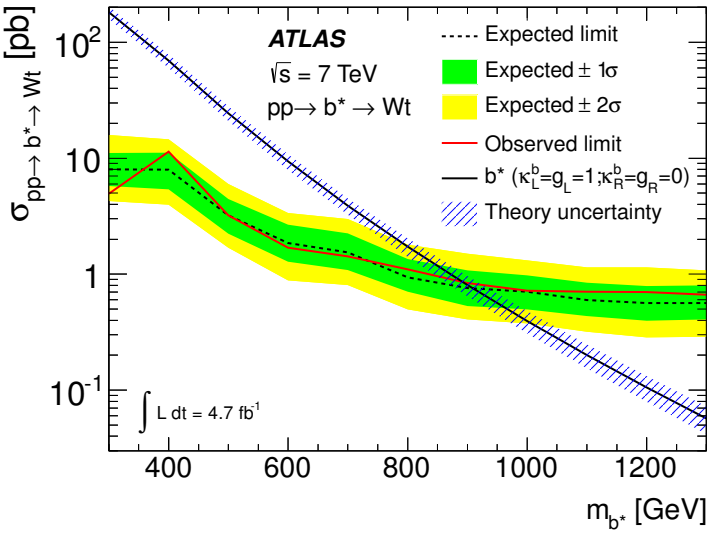

Figure 35: Cross section limits for $b^* \to Wt$ as a function of the b^* mass after combination of the single lepton and dilepton analyses. Shown are the theoratically predicted cross section for couplings $\kappa_L^{b^*} = g_L = 1$ and $\kappa_R^{b^*} = g_R = 0$ (in black, with grey uncertainty band), the expected upper limit in the case that no signal is present (dashed, with 1 and 2σ uncertainty bands) and the observed limit (in red).

5

SINGLE TOP T-CHANNEL

This analysis focuses on the leptonic 2-jet signature of the t-channel, where the top quark decays leptonically, i.e. to a bottom quark and a W boson which subsequently decays to a lepton and a neutrino, and where both the bottom quark from the top decay as well as the light quark from the W interaction are detected (see figure 36).

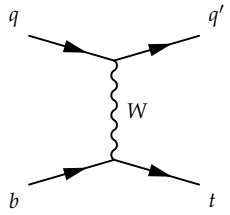

Figure 36: Leading order t-channel production Feynman diagram.

The main backgrounds to the leptonic t-channel are top pair and W+jets. Other backgrounds are s-channel and Wt-channel single top production, Z+jets, diboson and QCD multijet.

This chapter describes the selection of the t-channel events and the measurement of the cross section using a *cut and count* method. The results described in this chapter are used in a more detailed t-channel analysis described in the next chapter, which focuses on polarization.

5.1 DATA AND MONTE CARLO

This analysis is performed using the 2012 dataset recorded by ATLAS at a center-of-mass energy of $\sqrt{s} = 8$ TeV/c^2 with an integrated luminosity of 20.28 fb^{-1}. The contribution from the QCD multijet background is determined using the data-driven matrix method described in section 4.4 and [104]. Other contributions from background and signal processes are estimated using MC samples, in some cases normalized using data.

The t-channel signal MC sample is generated using AcerMC and PYTHIA. AcerMC is a leading-order generator, which allows for an unambiguous identification of the truth-level partons participating in the hard scatter interaction. This is essential in the analysis described in the next chapter.

All top-quark backgrounds, s-channel, Wt-channel and top pair, are generated using Powheg and PYTHIA. Sherpa is used for both W+jets and Z+jets, and the diboson samples are generated using HERWIG.

The W+jets background is the main background in this analysis. Since Sherpa is a leading-order generator the normalization of the W+jets background prediction is not very accurate and has to be determined with data. The Sherpa samples were split up into three samples depending on the flavor of the final state quarks, as Sherpa does not generate separate W+jets samples categorized by the flavor of the quarks in the matrix element. This replaces the categorization as done by Alpgen (see section 4.4). The three samples are: one with bottom quarks (W_b), one with charm quarks (and no bottom quarks) (W_c) and one with only light quarks (W_l).

The resulting correction factors are shown in table 16. These factors are determined using the tag-counting method described in section 4.4.2, where events from the final selection are removed from the used preselection tag and pretag samples in order to reduce the effect of the signal cross section on these factors. As can be seen, these factors are strongly correlated between jet-bins. A significant difference can be seen between the correction factors of the electron and the muon channels.

jet-bin	κ_b	κ_c	κ_l	κ_{tot}
1	0.87	0.79	1.05	0.93
2	0.89	0.81	1.07	0.99
3	0.91	0.83	1.09	0.92
4	0.92	0.84	1.11	0.91

(a) Electron channel.

jet-bin	κ_b	κ_c	κ_l	κ_{tot}
1	0.90	1.16	0.97	1.05
2	0.89	1.15	0.96	1.14
3	0.88	1.14	0.95	1.04
4	0.88	1.13	0.95	0.96

(b) Muon channel.

Table 16: Correction factors for heavy flavor composition (κ_b, κ_c, κ_l) and overall normalization (κ_{tot}) for Sherpa W+jets as determined with the tag counting method. The uncertainty on these correction factors when applied to the final selection is 50% for the flavor composition factors and 20% for the overall normalization [105].

5.2 EVENT SELECTION

The selection consists of two stages: the *preselection* and the *selection*. The preselection selects events with a basic t-channel signature. After the preselection the top quark can be reconstructed. The event selection is designed to efficiently select t-channel events while increasing the ratio of signal to background.

5.2.1 *Preselection*

The event preselection of this analysis follows a similar strategy as the event preselection of the ATLAS 7 TeV t-channel cross section measurement [106]. Events are required to contain at least one good primary vertex candidate and to pass several data quality requirements. Exactly one lepton (electron or muon) is required, which must match the trigger-level lepton.

	electron		muon	
	pretag	tag	pretag	tag
t-channel	$1.75 \pm 0.01 \times 10^4$	$7.98 \pm 0.03 \times 10^3$	$2.27 \pm 0.01 \times 10^4$	$1.02 \pm 0.00 \times 10^4$
top pair	$4.69 \pm 0.01 \times 10^4$	$2.10 \pm 0.01 \times 10^4$	$5.82 \pm 0.01 \times 10^4$	$2.60 \pm 0.01 \times 10^4$
Wt-channel	$7.05 \pm 0.07 \times 10^3$	$2.92 \pm 0.05 \times 10^3$	$8.74 \pm 0.08 \times 10^3$	$3.49 \pm 0.05 \times 10^3$
s-channel	$1.11 \pm 0.01 \times 10^3$	$5.31 \pm 0.05 \times 10^2$	$1.48 \pm 0.01 \times 10^3$	$7.01 \pm 0.05 \times 10^2$
W+HF jets	$2.62 \pm 0.01 \times 10^5$	$1.74 \pm 0.01 \times 10^4$	$5.54 \pm 0.01 \times 10^5$	$3.26 \pm 0.02 \times 10^4$
W+light jets	$8.41 \pm 0.02 \times 10^5$	$1.44 \pm 0.13 \times 10^3$	$1.26 \pm 0.00 \times 10^6$	$2.22 \pm 0.18 \times 10^3$
Z+jets	$1.26 \pm 0.01 \times 10^5$	$3.14 \pm 0.09 \times 10^3$	$8.89 \pm 0.09 \times 10^4$	$2.81 \pm 0.05 \times 10^3$
diboson	$1.53 \pm 0.01 \times 10^4$	$4.85 \pm 0.11 \times 10^2$	$2.04 \pm 0.01 \times 10^4$	$6.20 \pm 0.13 \times 10^2$
QCD multijet	$1.02 \pm 0.51 \times 10^5$	$6.22 \pm 3.11 \times 10^3$	$2.38 \pm 1.19 \times 10^4$	$4.46 \pm 2.23 \times 10^3$
total MC	$1.42 \pm 0.01 \times 10^6$	$6.11 \pm 0.05 \times 10^4$	$2.03 \pm 0.00 \times 10^6$	$8.30 \pm 0.04 \times 10^4$
data	1.44×10^6	6.08×10^4	1.96×10^6	8.26×10^4

Table 17: Event yields after the preselection cuts. All quoted uncertainties are purely based on MC statistics, except for the QCD multijet uncertainty which is set to 50%.

The missing transverse energy (E_T^{miss}) must be larger than 30 GeV, and in order to reduce the amount of QCD multijet background, the transverse W mass[1] is required to be larger than 50 GeV/c^2. These requirements were tightened with respect to the 7 TeV t-channel measurement. Finally, each event is required to have exactly two jets, of which one is b-tagged.

In summary, the most important preselection cuts are:

$$E_T^{miss} > 30 \text{ GeV}, \tag{23}$$

$$n_{jets} = 2, \tag{24}$$

$$M_T(W) > 50 \text{ GeV}/c^2, \tag{25}$$

$$n_{b-jets} = 1. \tag{26}$$

Table 17 shows the event yields for the electron and muon channels after preselection, with (*tag*) and without (*pretag*) the b-tagging requirement (equation 26).

Plots showing the distributions at pretag and tag level of three key variables, the lepton transverse momentum, the missing transverse energy and the transverse W mass, for the electron and muon channels are shown in figure 37. The distributions show a good data-MC agreement, although the muon channels shows a small discrepancy before the b-tagging requirement. In general, the enormous impact of this b-tagging requirement on the backgrounds is cleary visible.

1 See section 4.3 for a definition.

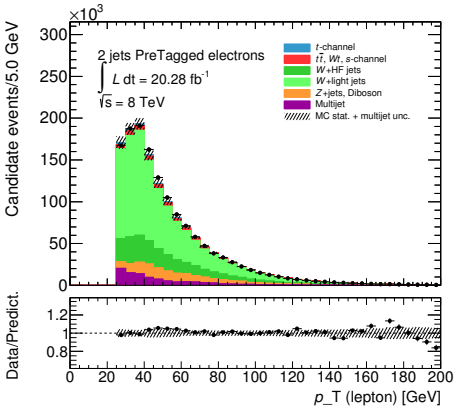

(a) Electron p_T, pretag.

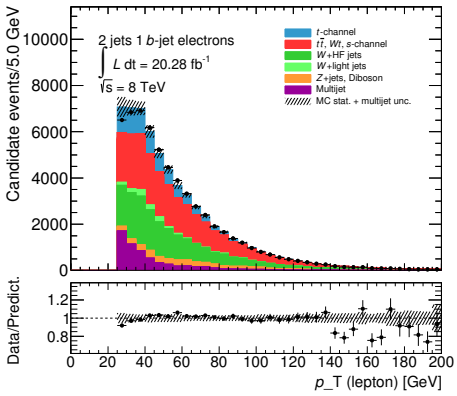

(b) Electron p_T, tag.

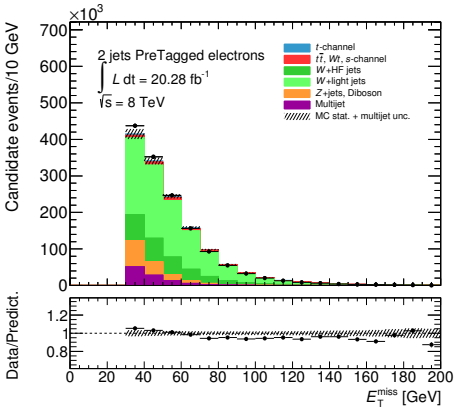

(c) E_T^{miss}, pretag.

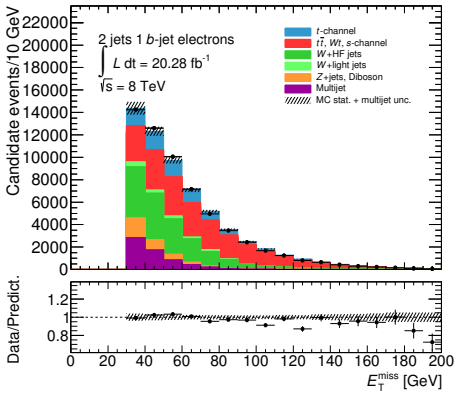

(d) E_T^{miss}, tag.

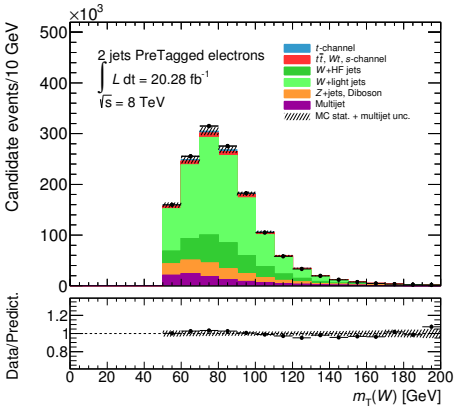

(e) $M_T(W)$, pretag.

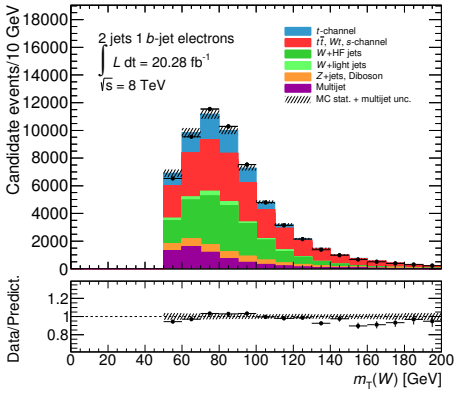

(f) $M_T(W)$, tag.

Figure 37: Electron channel preselection control plots. The plots on the left side show pretag distributions, while the plots on the right side show tag distributions. The hatched band on the MC and the unity line in the ratio plot is the statistical MC uncertainty.

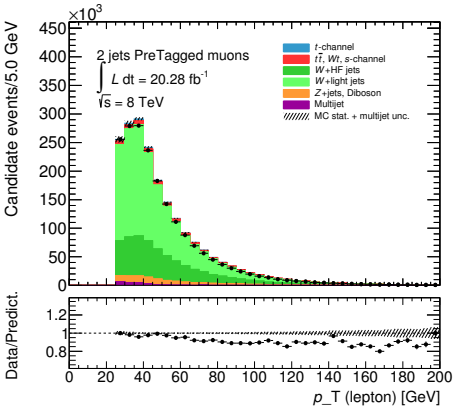

(g) Muon p_T, pretag.

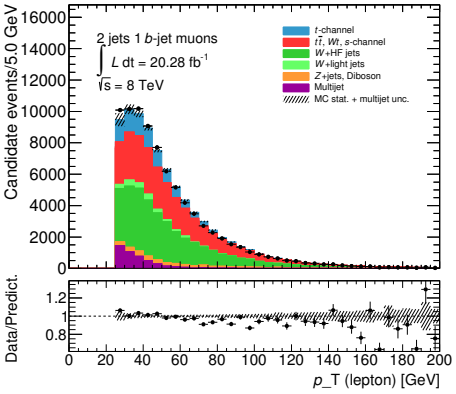

(h) Muon p_T, tag.

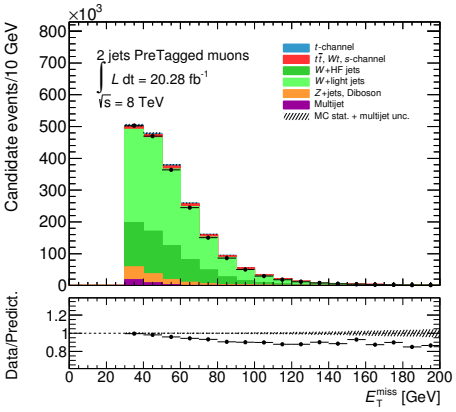

(i) E_T^{miss}, pretag.

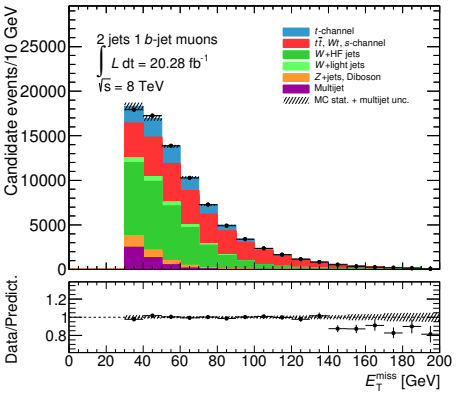

(j) E_T^{miss}, tag.

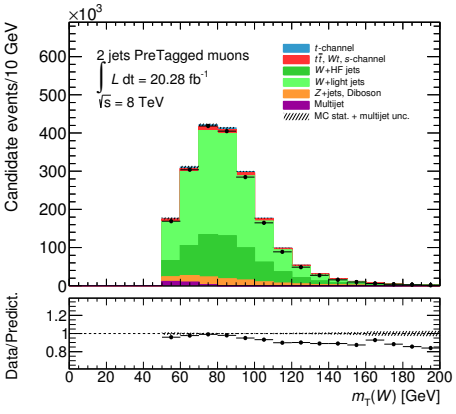

(k) $M_T(W)$, pretag.

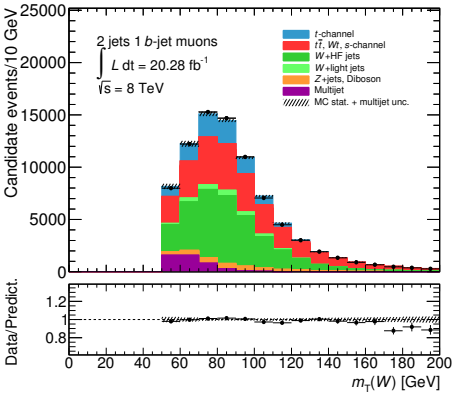

(l) $M_T(W)$, tag.

Figure 37: Muon channel preselection control plots. The plots on the left side show pretag distributions, while the plots on the right side show tag distributions. The hatched band on the MC and the unity line in the ratio plot is the statistical MC uncertainty.

5.2.2 *Particle reconstruction*

Each event that passes the preselection contains the decay products of the leptonic decay of a top quark: a lepton (electron or muon), a neutrino in the form of missing transverse energy and a heavy jet. From these decay products we can reconstruct the four-momenta of the W boson and the top quark.

W BOSON RECONSTRUCTION The momentum of the lepton (electron or muon) is measured by the detector, but the neutrino escapes all detection. By assuming that the neutrino is the only particle that is not detected, and therefore the only particle that contributes to the missing transverse energy, we can write down an equation to reconstruct the neutrino four-momentum using the W boson mass of $M(W) = 80.399\ \mathrm{GeV}/c^2$:

$$M^2(W) = M^2(\ell) + \frac{2}{c^2}\left(\frac{E(\ell)E(\nu)}{c^2} - \vec{p}(\ell)\cdot\vec{p}(\nu)\right), \tag{27}$$

where $M(\ell)$ is the mass of the charged lepton, $E(\ell)$ and $E(\nu)$ are the energies of the charged lepton and the neutrino respectively, $\vec{p}(\ell)$ and $\vec{p}(\nu)$ are the momenta of the charged lepton and the neutrino respectively, and the neutrino mass is assumed to be zero. We can write this as a quadratic equation in $p_z(\nu)$:

$$\begin{aligned} 0 = &\left(p_z^2(\ell)c^2 - E^2(\ell)\right) p_z^2(\nu)c^2 \\ &+ \left(\Delta M_2 c^2 + 2c p_T(\ell)\cdot E_T^{\mathrm{miss}}\right) p_z(\ell)\, p_z(\nu)c^2 \\ &+ \frac{(\Delta M_2)^2 c^4}{4} + \Delta M_2 \left(p_T(\ell)\cdot E_T^{\mathrm{miss}}\right) c^3 + \left(p_T(\ell)\cdot E_T^{\mathrm{miss}}\right)^2 c^2, \end{aligned} \tag{28}$$

where $\Delta M_2 = M^2(W) - M^2(\ell)$, and $p_x + p_y = p_T$. Depending on the momentum of the lepton and the missing transverse energy, equation 28 may have 0, 1 or 2 real solutions for $p_z(\nu)$. The solution with the lowest $|p_z(\nu)|$ is used in the case that there are two real solutions. When there are no real solutions the E_T^{miss} is scaled down to the value at which the equation has exactly one real solution.

TOP QUARK RECONSTRUCTION The top quark decays to a W boson and a bottom quark. By adding the momentum of the bottom quark as measured by the detector and the momentum of the W boson, reconstructed as described above, we obtain the reconstructed momentum of the top quark. This yields distributions as shown in figures 38e and 38f. The other subfigures in figure 38 are described below.

5.2.3 *Selection*

In order to further reduce the remaining backgrounds cuts are placed on four more variables. These cuts are placed on the absolute pseudorapidity of the light (non-b-tagged) jet, the scalar sum of all particle transverse momenta and the missing transverse energy (H_T), the reconstructed top mass as described above and the absolute difference in pseudorapidity between the two jets.

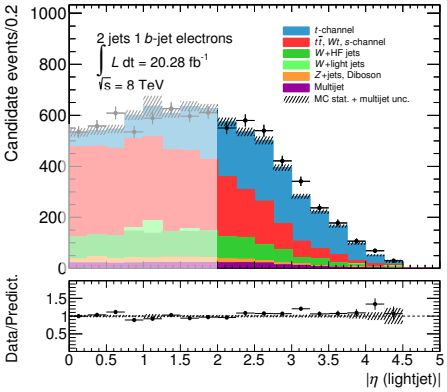

(a) Electron channel, $|\eta(j)|$.

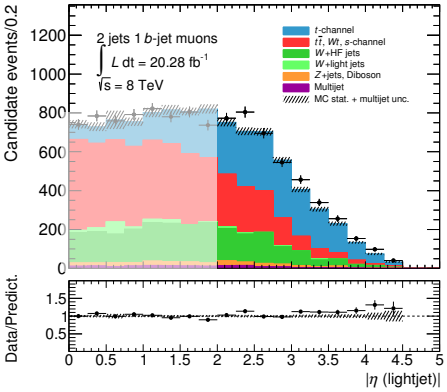

(b) Muon channel, $|\eta(j)|$.

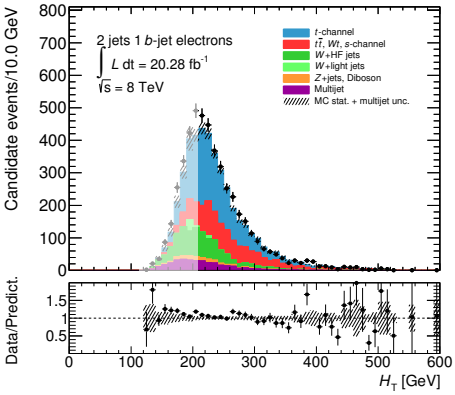

(c) Electron channel, H_T.

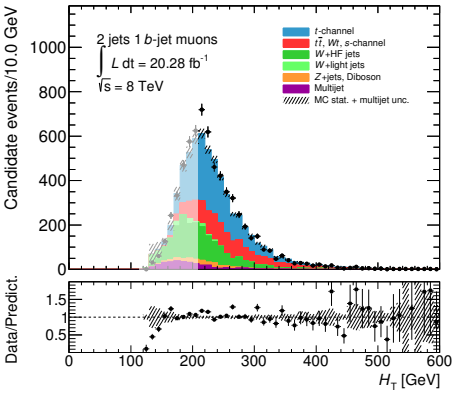

(d) Muon channel, H_T.

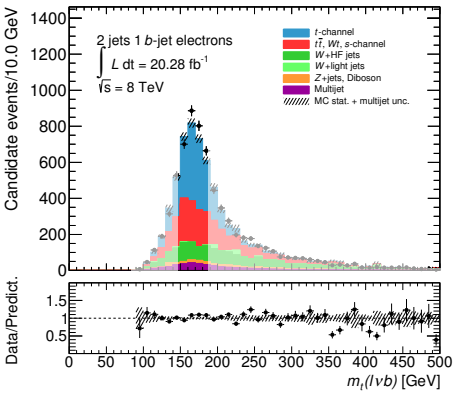

(e) Electron channel, m_{top}.

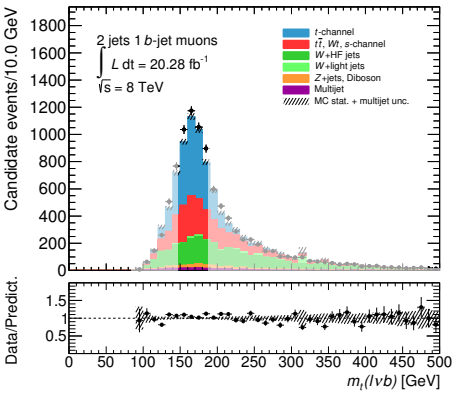

(f) Muon channel, m_{top}.

Figure 38: Distributions of the quantities used in the selection cuts after all selection cuts except the one on the concerning variable. The regions removed by the cut on the concerning variable is shown shaded.

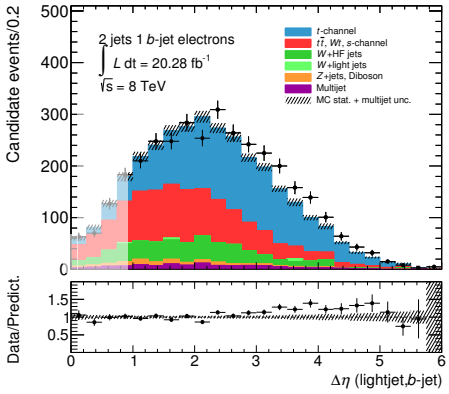

(g) Electron channel, $\Delta\eta(j, b)$.

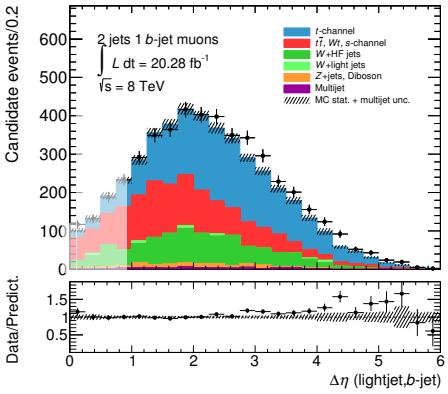

(h) Muon channel, $\Delta\eta(j, b)$.

Figure 38: Distributions of the quantities used in the selection cuts after all selection cuts except the one on the concerning variable. The regions removed by the cut on the concerning variable is shown shaded.

	electron	muon
t-channel	1453±13	1910±15
top pair	750±14	934±16
*W*t-channel	88±7	100±8
s-channel	19±0	29±1
W+HF jets	367±17	736±31
W+light jets	9±6	30±14
Z+jets	57±4	92±8
diboson	5±1	8±1
QCD multijet	93±47	50±25
total MC	2846±30	3893±43
data	3053	4161

Table 18: Event yields after the selection cuts. All quoted uncertainties are purely based on MC statistics, except for the QCD multijet uncertainty which is set to 50%.

The cuts are:

$$|\eta(j)| > 2, \tag{29}$$

$$H_T > 210 \text{ GeV}, \tag{30}$$

$$150 < m_{top} < 190 \text{ GeV}/c^2, \tag{31}$$

$$|\Delta\eta(b,j)| > 1. \tag{32}$$

Figure 38 shows the distributions of the four variables used in these cuts after all selection cuts including the effect of the concerning cut. Table 18 shows the event yields after the selection.

The cut on the pseudorapidity of the light jet makes use of the fact that in t-channel this jet is rather forward (high absolute pseudorapidity) and is effective against the W+jets and top backgrounds. The cut on H_T makes use of the high transverse momenta of the top decay products, and hence is effective against all non-top backgrounds. The cut on the reconstructed top mass is, naturally, effective against all backgrounds in which there is no top quark to reconstruct.

The distribution of the variable used in the last cut, the absolute difference in pseudorapidity between the jets, shows some disagreement between data and MC in the region $|\Delta\eta(b,j)| > 3$. Therefore the cut was placed at a low value, away from this region, making it only moderately effective against the remaining backgrounds. It might be possible to make it more effective by cutting at a higher value, but this comes with the risk of introducing a discrepancy between data and MC.

	preselection		selection
	pretag	tag	
electron	$1.4 \cdot 10^{-2}$	$1.8 \cdot 10^{-1}$	1.2
muon	$1.3 \cdot 10^{-2}$	$1.7 \cdot 10^{-1}$	1.1
combined	$1.4 \cdot 10^{-2}$	$1.7 \cdot 10^{-1}$	1.2

Table 19: Signal-to-background ratio at each step in the event selection. The ratio increases by about an order of magnitude at each step.

The preselection only selects events based on quality requirements and basic event topology and provides a signal-to-background ratio of the order of about 1/75 before the b-tagging requirement and 1/5 after the b-tagging requirement. The selection is efficient for signal and improves the ratio by about an order of magnitude, to 1.2 (see table 19).

5.3 CROSS SECTION MEASUREMENT

With the events selected as above the t-channel production cross section can be measured by scaling the t-channel sample such that data and MC match. In practice, in order to aid calculating the uncertainties, this is done by using a maximum-likelihood fit on the total number of signal and background events:

$$P(N_{obs} \,|\, \mu N_s + N_b), \tag{33}$$

where N_{obs} is the number of observed events, N_s and N_b are the number of expected signal and background events respectively, and μ is a free parameter. RooFit [107] is used to perform the maximum-likelihood fit.

When combining electron and muon channels, μ is found to be $\mu = 1.14 \pm 0.025$, where the uncertainty is based only on data statistics. Since the cross section used for generating the signal MC sample is $\sigma_{mc} = 87.76$ pb, we obtain

$$\sigma_{t-channel} = 100.1 \pm 3.34 \text{ pb (electron)}, \tag{34}$$

$$\sigma_{t-channel} = 99.8 \pm 3.30 \text{ pb (muon)}, \tag{35}$$

$$\sigma_{t-channel} = 100.1 \pm 2.22 \text{ pb (combined)}. \tag{36}$$

The uncertainties quoted here are based purely on data statistics.

5.4 SYSTEMATIC UNCERTAINTIES

In order to estimate the systematic uncertainty of the cross section measurement described in the previous section, various contributions to the total systematic uncertainty are evaluated. Each of these systematic uncertainties is briefly described below.

LUMINOSITY The uncertainty on the total integrated luminosity in the 2012 dataset is estimated using the same method as used for the 2011 dataset as described in [108]. The uncertainty on the luminosity is $\pm 2.8\%$.

JET ENERGY SCALE AND RESOLUTION The uncertainty on the jet energy scale is a large contributor to the systematic uncertainty. It is evaluated by shifting the energies of simulated jets up and down by one standard deviation (depending on the region of the detector and the energy of the jet, this varies between 1 and 6% [74]), and successively performing the analysis including object and event selection. The jet energy resolution uncertainty is evaluated by smearing the resolution in simulation.

JET RECONSTRUCTION EFFICIENCY The calorimeter jet reconstruction efficiency is measured with respect to reconstructed tracks of probe jets. The uncertainty on this efficiency is evaluated by varying the MC jet reconstruction efficiency.

b-TAGGING The uncertainties on the c-tag, b-tag and mistag rates are evaluated by varying the scalefactors used in MC for each of these rates one at a time. While the uncertainties on the b-tag rates are of the order of 2 to 8% depending on the energy of the jet, the c-tag and mistag rate uncertainties are much larger at 8 to 15% and 15 to 40% respectively [75, 109].

LEPTON ENERGY SCALE, RESOLUTION AND RECONSTRUCTION EFFICIENCY The uncertainties on the lepton scale, resolution and reconstruction efficiency are evaluated like the corresponding uncertainties for the jets. These uncertainties are evaluated separately for each lepton flavor, and are much smaller than the jet uncertainties [110].

MISSING TRANSVERSE ENERGY SCALE AND RESOLUTION The effects of the jet and lepton variations are taken into account when calculating the E_T^{miss} while evaluating these

uncertainties, so these effects do not need to be evaluated separately. The effects of the scale and resolution of the measurement of soft jets which are not included in the jet uncertainties are evaluated by separately varying the soft jet scale and resolution and recalculating the E_T^{miss}. These uncertainties are of the order of 2 to 3% [77].

MC GENERATOR Often there are differences in the results produced by different MC generation approaches. These differences are evaluated by replacing one of the MC samples by one generated with a different generator. This is done for all main backgrounds and the signal.

TOP PAIR The nominal top pair sample is generated by Powheg and PYTHIA. This sample is compared to a sample generated by MC@NLO.

W+JETS The nominal *W*+jets sample is generated by Sherpa. An alternative sample generated by Alpgen is used to compare to. The Z+jets background, of which the default sample is also generated by Sherpa, is also compared to a sample generated by Alpgen, simultaneously with the *W*+jets background.

t-CHANNEL The nominal t-channel signal sample is generated by AcerMC, which is a leading order generator. Several next-to-leading order generators are available, of which we use Powheg to compare to. As explained in the next chapter, it is not possible to use Powheg as the nominal generator. The cross section that is used to normalize the two samples is the same[2]: 87.76 pb.

BACKGROUND CROSS SECTION The uncertainties on the cross section of each background are incorporated by varying each background up and down by a predetermined fraction. The variations are shown in table 20.

The uncertainties on the top backgrounds are theoretical uncertainties [112, 113]. The uncertainty found using a data-driven method in the $\sqrt{s} = 7$ TeV t-channel cross section measurement [106] is used for the *W*+jets normalization. In this uncertainty, the effects of all other systematic uncertainties on the *W*+jets normalization have been taken into account. This includes a 100% uncertainty on the t-channel cross section. The theory uncertainties on the Z+jets and diboson cross sections are 4% and 5% respectively. In both cases an uncertainty due to Berends scaling of 24% has to be included [114]. The systematic uncertainties on the cross sections are evaluated separately for each background.

QCD MULTIJET NORMALIZATION Like in the analysis described in the previous chapter, a normalization uncertainty of 50% is assigned to the QCD multijet background.

PDF As shown in [113], the uncertainty due to the PDFs is $\pm 1.1\%$.

5.5 RESULTS

Object and event selections are performed for each of the abovementioned systematic uncertainties. Uncertainties which do not have individual up and down variations are symmetrized by taking the nominal with the negative difference as opposite variation.

2 This is the result of a next-to leading order plus next-to-next-to leading log calculation [111].

	up	down
top pair	+5.9%	−5.9%
*W*t-channel	+6.8%	−6.8%
s-channel	+3.9%	−3.9%
W+jets	+28%	−28%
Z+jets	+24%	−24%
diboson	+25%	−25%

Table 20: Uncertainties on the background cross sections. All uncertainties are theory uncertainties, except for the uncertainty on *W*+jets.

The effects of the systematic uncertainties are shown in table 21. The change from AcerMC to Powheg as t-channel generator gives by far the largest uncertainty.

The large difference in signal event yields between the AcerMC and Powheg samples is unfortunate, but not unexpected since this is a comparison between a leading order and a next-to-leading order generator.

The results, including all systematic and statistical uncertainties, are $\mu = 1.14 \pm 0.27$ and $\mu = 1.14^{+0.27}_{-0.26}$ for the electron and muon channels respectively, yielding a combined result of $\mu = 1.14^{+0.27}_{-0.26}$, which translates to

$$\sigma_{t-channel} = 100.1 \pm 3.34(stat)^{+12.3}_{-12.3}(sys)^{+20.0}_{-20.0}(th)\ pb\ (electron), \quad (37)$$

$$\sigma_{t-channel} = \ 99.8 \pm 3.30(stat)^{+14.3}_{-12.6}(sys)^{+18.2}_{-18.2}(th)\ pb\ (muon), \quad (38)$$

$$\sigma_{t-channel} = 100.1 \pm 2.22(stat)^{+13.3}_{-13.3}(sys)^{+19.1}_{-19.1}(th)\ pb\ (combined). \quad (39)$$

Here the theory uncertainty consists of the t-channel Powheg, top pair MC@NLO and W/Z+jets Alpgen variations and the PDF uncertainty. The quoted systematic consists of all other systematic uncertainties.

When the t-channel Powheg variation is ignored, a combined result of $\sigma_{t-channel} = 100.1 \pm 2.22(stat)^{+13.3}_{-13.3}(sys)^{+7.2}_{-7.2}(th)$ pb is found, where the theory uncertainty is reduced by more than a factor two. When the Powheg variation is used as nominal, instead of the AcerMC sample, the measured cross section goes down by 20%, which is not unexpected due to the differences between to two generators, AcerMC being leading order and Powheg being a next-to-leading order generator.

	electron		muon	
	up	down	up	down
luminosity	−4.9%	+5.1%	−5.1%	+5.4%
jet energy scale	−4.3%	+5.1%	−3.3%	+7.3%
jet energy resolution	+0.8%	−0.8%	+2.0%	−2.0%
jet reconstruction	−0.1%	+0.1%	+0.7%	−0.7%
b-tag rate	−5.4%	+5.8%	−5.4%	+5.8%
c-tag rate	−2.6%	+2.6%	−4.4%	+4.4%
mistag rate	−0.5%	+0.5%	−0.6%	+0.6%
lepton energy scale	+4.3%	−4.3%	−0.6%	+0.2%
lepton energy resolution	−0.4%	−0.1%	−0.8%	+0.6%
lepton trigger	−0.4%	+0.4%	−0.7%	+0.7%
soft jet scale	−1.7%	+0.7%	−0.9%	+2.4%
soft jet resolution	−2.8%	−1.8%	−2.1%	−2.4%
t-channel Powheg	−19.2%	+19.2%	−16.1%	+16.1%
top pair MC@NLO	−3.3%	+3.3%	−2.5%	+2.5%
W+jets, Z+jets Alpgen	−4.3%	+4.3%	+8.1%	−8.1%
PDF	+1.1%	−1.1%	+1.1%	−1.1%
top pair cross section	−2.3%	+2.3%	−2.2%	+2.2%
Wt-channel cross section	−0.4%	+0.4%	−0.3%	+0.3%
s-channel cross section	−0.1%	+0.1%	−0.1%	+0.1%
W+jets cross section	−4.4%	+4.4%	−6.8%	+6.8%
Z+jets cross section	−0.8%	+0.8%	−1.0%	+1.0%
diboson cross section	−0.1%	+0.1%	−0.1%	+0.1%
QCD multijet normalization	−2.8%	+2.8%	−1.2%	+1.2%
MC statistics	+1.8%	−1.8%	+2.0%	−2.0%
total	+23.4%	−23.5%	+23.2%	−22.2%

Table 21: Effects of each systematic uncertainty on the measured cross section. Uncertainties without individual up and down variations are symmetrized.

6

SEARCH FOR CP-VIOLATION IN T-CHANNEL

This chapter describes the further analysis of the t-channel single top events isolated in the previous chapter. A measurement of the polarization of the top quark and the polarization of the W boson in the normal frame, which is sensitive to CP-violating new physics, is performed. A similar analysis has been performed before on the $\sqrt{s} = 7$ TeV/c^2 dataset [115, 116].

As explained in section 1.4, the polarization of the top quark, P, is related to the distribution of the angle between a spin analyzer (a decay product of the top quark) and the top spin direction:

$$\frac{1}{\Gamma}\frac{d\Gamma}{d\cos\theta^x} = \frac{1}{2}\left(1 + P\alpha\cos\theta^x\right). \tag{40}$$

Angle θ^x is defined in the spectator spin basis, in which the spin quantization axis is chosen along the direction of the momentum of the spectator quark, and the charged lepton is used as spin analyzer, in which case $\alpha = s0.998$, where s is the sign of the charge of the lepton. A diagram showing the definition of θ^x is shown in figure 10b.

The polarization of the W boson in the normal frame is related to the angle between the momentum of the lepton in the rest frame of the W boson and the normal axis, which is perpendicular to the momenta of the W boson and the spectator quark in the top quark rest frame (a diagram defining this angle, $\theta^{\hat{N}}$, is shown in figure 10f):

$$\frac{1}{\Gamma}\frac{d\Gamma}{d(\cos\theta^{\hat{N}})} = \frac{3}{8}\left(1+\cos\theta^{\hat{N}}\right)^2\tilde{F}_+^{\hat{N}} + \frac{3}{8}\left(1-\cos\theta^{\hat{N}}\right)^2\tilde{F}_-^{\hat{N}} + \frac{3}{4}\left(\sin\theta^{\hat{N}}\right)^2\tilde{F}_0^{\hat{N}}, \tag{41}$$

where the effective polarization fractions, which satisfy $\tilde{F}_+^{\hat{N}} + \tilde{F}_-^{\hat{N}} + \tilde{F}_0^{\hat{N}} = 1$, are defined as $\tilde{F}_\pm^{\hat{N}} = \frac{1}{2}\{(1+P)F_\pm^{\hat{N}} + (1-P)F_\mp^{\hat{N}}\}$ and $\tilde{F}_0^{\hat{N}} = F_0^{\hat{N}}$. From these polarization fractions the forward-backward asymmetry can be calculated using $A_{FB}^{\hat{N}} = \frac{3}{4}(\tilde{F}_+^{\hat{N}} - \tilde{F}_-^{\hat{N}})$.

The imaginary part of the right-handed tensor coupling, of which a non-zero value would imply the presence of CP-violation, is related to both the top quark polarization and the forward-backward asymmetry in the normal frame via $A_{FB}^{\hat{N}} = 0.64P\mathcal{I}(g_R)$ if the other anomalous couplings, V_R and g_L, are zero.

6.1 FOLDING

Measuring (properties of) the distributions mentioned above is not directly possible, as the resolution and acceptance of the experiment, the object selection and the event

selection all modify the distributions. For example, isolation criteria in the object selection prohibit electrons to be very close to jets, effectively removing the upper end of the $\cos\theta^x$ distribution (at $\theta^x = 0$) as shown in figure 39. Therefore it is necessary to translate between the original distribution (at *generator-level*[1], before the imperfect measurement and the selections) and the measured distribution after the event selection (at *reconstruction-level*).

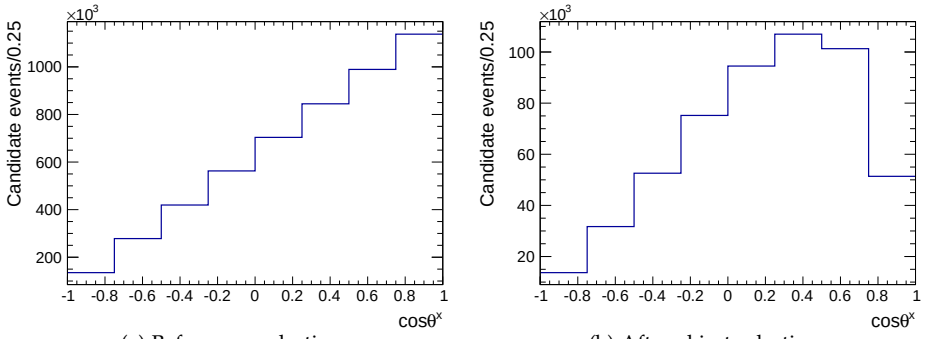

(a) Before any selection.

(b) After object selection.

Figure 39: Distributions of truth-level $\cos\theta^x$ for electron channel MC events before any selection (figure a) and after the object selection and basic quality requirements (figure b).

Folding is the process of translating the generator-level distribution to the reconstruction-level distribution. It is done using a resolution matrix $\mathcal{R}$, which describes the relation between selected generator-level and reconstruction-level events, and an efficiency table $\mathcal{E}$ which describes the effect of the event selection. The expected number of events in bin j at reconstruction-level, ν_j, can then be calculated using

$$\nu_j = \sum_{i \in \theta_{gen}} \nu_i^{gen} \cdot \mathcal{E}_i \cdot \mathcal{R}_{ij}, \tag{42}$$

where ν_i^{gen} is the number of events in bin i at generator-level. A more detailed definition of $\mathcal{R}$ and $\mathcal{E}$ follows below.

6.2 INPUT DATA

This analysis uses the object and event selections as described in the previous chapter. The reconstructed top quark and W boson momentum vectors are used in the computation of the angles θ^x and $\theta^{\hat{N}}$. When computing these angles and boosting momentum vectors to and from the various reference frames (the experimental reference frame, the top quark center-of-mass frame, and the W boson center-of-mass frame) care should be taken to use the same boosts for all momentum vectors, in order not to introduce dissimilar Wigner angles (see appendix A for more details).

1 This is also called *truth-level*.

6.2.1 *Angular distributions*

All angular distributions used in this analysis range from -1 to $+1$ in $\cos\theta$ and are divided into eight bins. The resolution matrices in figure 41 show that this is a reasonable choice for the bin size. The input angular distributions at reconstruction level are shown in figure 40. While the distribution of $\cos\theta^{x}$ is an asymmetric peak originating from a linear distribution (see figure 39), the distribution of $\cos\theta^{\hat{N}}$ is symmetric, with peaks on either side. In all plots shown in this chapter, including these angular distributions, the MC prediction has been scaled using scale factors which have been obtained from the likelihood fit as described in section 6.3.1.

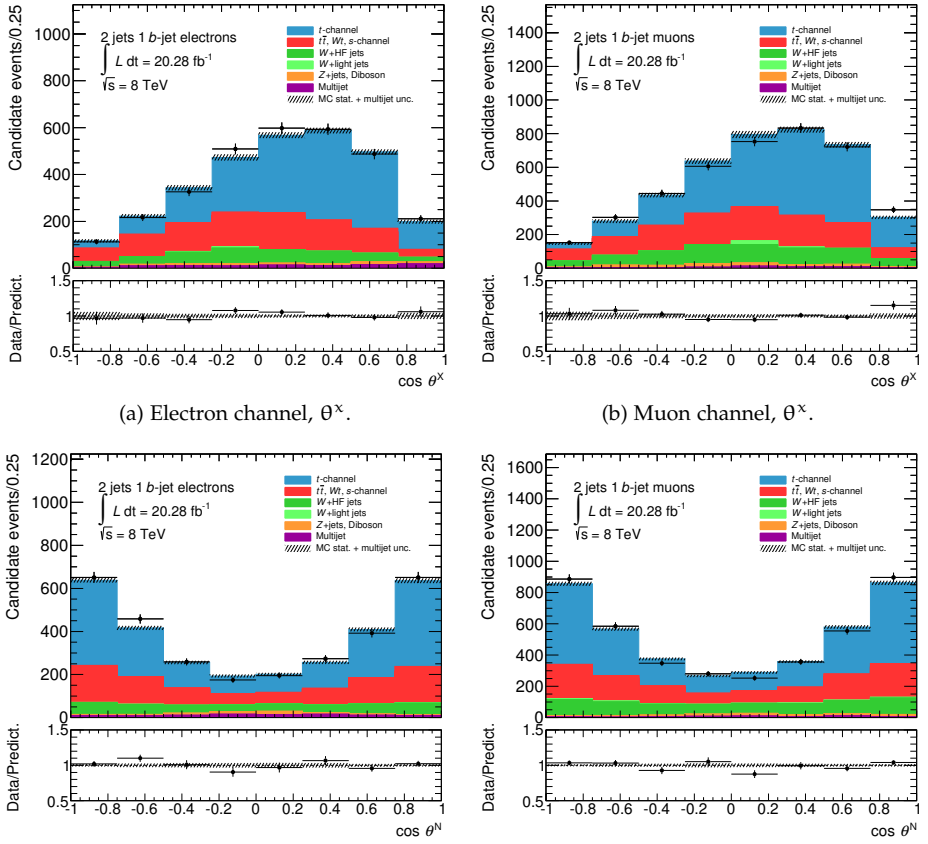

(a) Electron channel, θ^{x}.

(b) Muon channel, θ^{x}.

(c) Electron channel, $\theta^{\hat{N}}$.

(d) Muon channel, $\theta^{\hat{N}}$.

Figure 40: Angular distributions $\cos\theta^{x}$ and $\cos\theta^{\hat{N}}$ of the selected events for both electron (left) and muon channel (right). The hatched band on the MC and the unity line in the ratio plot is the statistical MC uncertainty.

6.2.2 *Resolution matrix*

The resolution matrices are constructed using the AcerMC signal sample, of which both the generator-level and reconstruction-level data are available for each event. A two-dimensional histogram $\mathcal{R}$, corresponding to the angle at generator-level (θ_{gen}) and the angle at reconstruction-level (θ_{reco}), is filled with all selected t-channel events, resulting in a mostly diagonal matrix. This matrix is then normalized such that the sum of all θ_{reco} bins in a θ_{gen} bin is equal to unity:

$$\forall i \in \theta_{gen} : \sum_{j \in \theta_{reco}} \mathcal{R}_{i,j} = 1. \tag{43}$$

The matrices for θ^x in both lepton channels are shown in figure 41.

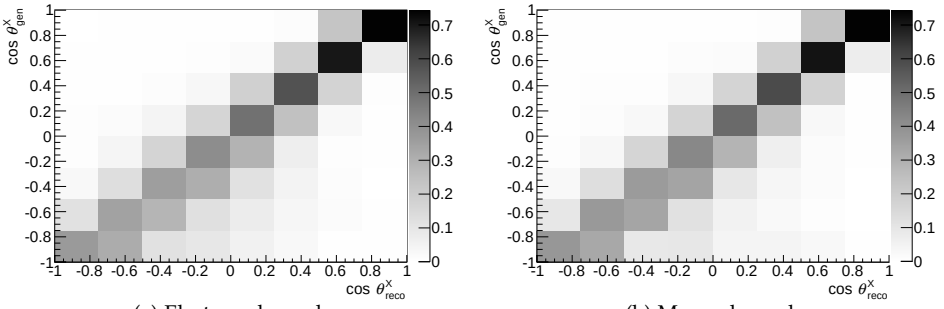

(a) Electron channel. (b) Muon channel.

Figure 41: Resolution matrices for the angle θ^x in the electron and muon channels. The angle at reconstruction-level is shown on the horizontal axis, while the angle at generator-level is shown on the vertical axis. The color code represents the fraction of events in a bin.

6.2.3 *Efficiency table*

The efficiency table describes the effect of the event selection on the generator-level angular distribution. It contains the fraction of generator-level events which pass the event selection for each generator-level θ-bin:

$$\forall i \in \theta_{gen} : \mathcal{E}_i = \frac{N_i^{sel}}{N_i^{tot}}. \tag{44}$$

The efficiency table for θ^x is shown in table 22. Only single top t-channel events where the *W* boson decays leptonically are considered. In one third of these events the *W* decays to a tau lepton. Of the events with an electron or a muon, roughly 10% of the events passes the preselection. The very stringent selection cuts bring these efficiencies below the percent level.

θ^x-bin	1	2	3	4	5	6	7	8	
electron	3.0	5.1	6.6	7.4	7.4	7.5	5.3	1.8	$\times 10^{-3}$
muon	3.5	5.9	7.7	9.1	9.8	9.6	7.3	2.9	

Table 22: Efficiency table per generator-level θ^x-bin for θ^x in both lepton channels.

6.3 LIKELIHOOD FIT

The folding procedure uses a maximum-likelihood estimator fit, which has the polarization (α_P) or helicity (F_+, F_-) parameter(s) and scale factors (β_k) for the signal and the large backgrounds as free parameters. With the set of physics parameters written as γ, the log-likelihood is given by:

$$\ln \mathcal{L}(\gamma, \beta_k; n_{ij}) = \sum_{i \in D} \sum_{j \in N_i} \left(n_{ij} \ln \mu_{ij} - \mu_{ij} \right) - \frac{1}{2} \sum_{k \in B} \left(\frac{\beta_k - 1}{\Delta_k} \right)^2, \tag{45}$$

where the first term is a Poisson term with the observed number of events (n_{ij}) and the expectation value (μ_{ij}) for each bin in every distribution i in the set of distributions D, where N_i is the set of bins in a distribution, and the second term is a Gaussian constraint given by Δ_k on the background scale factors β_k, centered around 1. The expectation value is given by:

$$\mu_{ij} = \sum_{k \in S \cup B} \beta_k \nu_{ijk}, \tag{46}$$

where S is the signal, B is the set of backgrounds, and ν_{ijk} is the number of events in distribution i, bin j and sample k. The number of signal events in each bin is obtained by the folding:

$$\nu_{i=\theta,j,k=\text{signal}}(\gamma) = \sum_{l \in \theta_{gen}} \nu_l^{gen}(\gamma) \cdot \mathcal{E}_l \cdot \mathcal{R}_{lj}, \tag{47}$$

where $\nu_l^{gen}(\gamma)$ is the expected number of events in bin l at generator-level for the set of physics parameters γ.

Although measured on the same dataset, the observables, $\cos\theta^x$ and $\cos\theta^{\hat{N}}$, are treated independently. This can be done because there is no correlation between the two, as shown in section 6.7. When combining the results, in section 6.9, the correlated systematic uncertainties are treated as such.

6.3.1 *Signal and background normalization*

The normalization of background and signal has to be determined simultaneously. To increase the sensitivity of the fitting procedure and reduce any possible influence of anomalous couplings on the fitting, a second distribution is used: the sidebands of the top mass distribution. It should be noted that events in these sidebands fulfill all other selection requirements and therefore obey the same normalization as the signal selection.

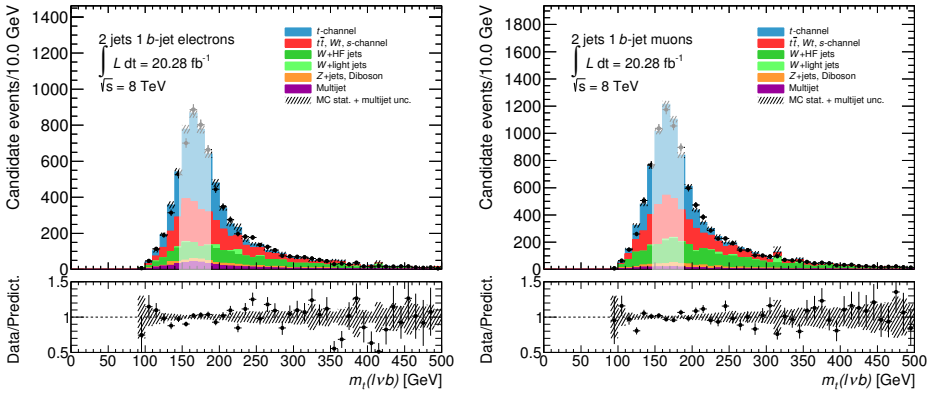

(a) Electron channel.

(b) Muon channel.

Figure 42: Top mass distributions for selected events, without the cut on the top mass, and scaled with the scale factors shown in table 23. The region removed by the inverted top mass cut is shaded.

The signal normalization is allowed to vary unconstrained. The normalizations of the two main backgrounds, top pair and W+jets HF, are constrained using $\Delta_{t\bar{t}} = 9\%$ and $\Delta_{W+\text{jets HF}} = 30\%$, corresponding to the expected accuracy of the predictions based on theoretical uncertainties. The normalization of all other backgrounds is fixed.

Table 23 shows the results of the normalization fit on the $\cos\theta^x$ distribution. A similar set of results can be obtained using the $\cos\theta^{\hat{N}}$ distribution. A cross section measurement using these results is described in section 6.8. Plots of the distributions scaled using the scale factors shown in table 23 are shown in figure 43. All distributions show a very good data-MC agreement. The data-MC agreement in the muon channel top mass distribution is (as can be expected) better when using the top mass distribution in the fit.

process	electron	muon
t-channel	1.144±0.047	1.179±0.043
top	1.021±0.081	1.046±0.081
W+jets HF	0.824±0.081	0.733±0.046

Table 23: Fitted scale factors (β_k) for signal and the two main backgrounds determined from a fit on the $\cos\theta^x$ distribution. The shown uncertainties are based purely on data statistics.

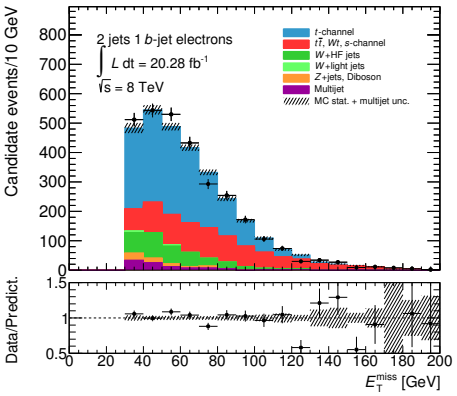

(a) Electron channel, E_T^{miss}.

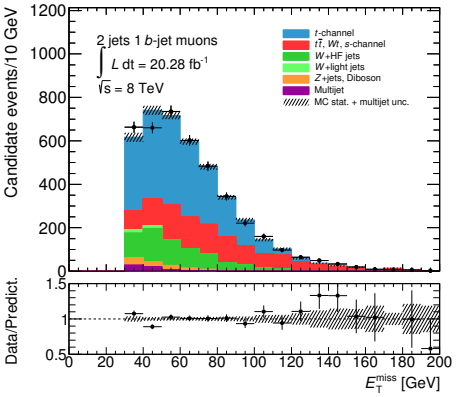

(b) Muon channel, E_T^{miss}.

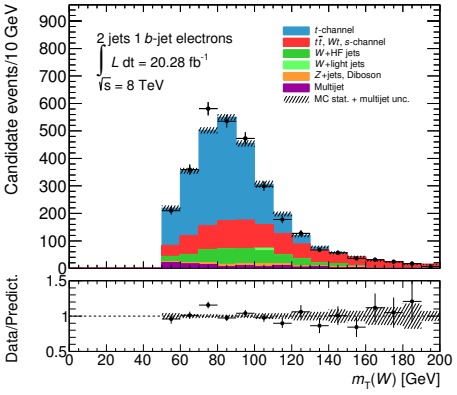

(c) Electron channel, $M_T(W)$.

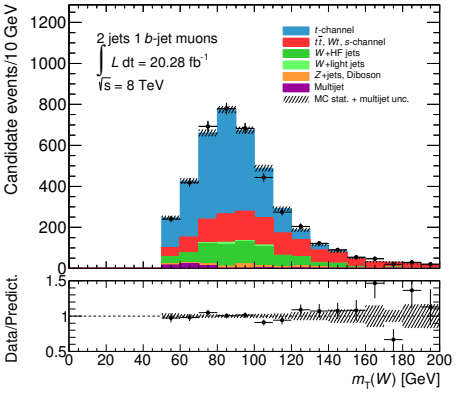

(d) Muon channel, $M_T(W)$.

Figure 43: Distributions of two variables used in the selection, scaled with the scale factors shown in table 23.

6.4 TOP POLARIZATION MEASUREMENT

By applying the folding procedure as described above to the $\cos\theta^x$ distributions (figures 40a and b) and using the sidebands of the top mass distribution (figure 42) to normalize the signal and the two main backgrounds, the following results are obtained:

$$P = 0.946 \pm 0.097 \text{ (electron)}, \tag{48}$$

$$P = 0.893 \pm 0.084 \text{ (muon)}, \tag{49}$$

$$P = 0.924 \pm 0.068 \text{ (combined)}. \tag{50}$$

where the spin analyzing power $\alpha = 1$ of the lepton is used, and where the quoted uncertainties are based purely on data statistics. As expected, the uncertainty on the combined result is lower than than the uncertainties of the individual measurements due to the increased statistics. The difference between the electron and muon channel measurements can be explained by the statistical uncertainty alone.

6.5 W BOSON POLARIZATION MEASUREMENT

Applying the folding method to the $\cos\theta^{\hat{N}}$ distributions (figures 40c and d) and including the sidebands of the top mass distribution in the fit, the following polarization fractions are extracted for the electron channel:

$$\tilde{F}_+^{\hat{N}} = 0.450 \pm 0.060, \tag{51}$$

$$\tilde{F}_-^{\hat{N}} = 0.484 \pm 0.062, \tag{52}$$

$$\tilde{F}_0^{\hat{N}} = 0.066 \pm 0.086. \tag{53}$$

The results for the muon channel are:

$$\tilde{F}_+^{\hat{N}} = 0.515 \pm 0.054, \tag{54}$$

$$\tilde{F}_-^{\hat{N}} = 0.531 \pm 0.055, \tag{55}$$

$$\tilde{F}_0^{\hat{N}} = -0.045 \pm 0.077. \tag{56}$$

All uncertainties quotes here are based purely on data statistics. This yields the following results for $A_{FB}^{\hat{N}}$:

$$A_{FB}^{\hat{N}} = \frac{3}{4}\left(\tilde{F}_+^{\hat{N}} - \tilde{F}_-^{\hat{N}}\right) = -0.026 \pm 0.064 \text{ (electron)}, \tag{57}$$

$$A_{FB}^{\hat{N}} = \frac{3}{4}\left(\tilde{F}_+^{\hat{N}} - \tilde{F}_-^{\hat{N}}\right) = -0.012 \pm 0.058 \text{ (muon)}, \tag{58}$$

$$A_{FB}^{\hat{N}} = \frac{3}{4}\left(\tilde{F}_+^{\hat{N}} - \tilde{F}_-^{\hat{N}}\right) = -0.018 \pm 0.044 \text{ (combined)}, \tag{59}$$

which is fully compatible with the SM within the statistical uncertainty, and the electron and muon channel are compatible, providing an important cross-check.

6.6 SYSTEMATIC UNCERTAINTIES

The systematic uncertainty on the measurements presented in the sections above is estimated by evaluating various contributions. The list of contributions includes all the systematic uncertainties described in section 5.4, and a few additional checks as appropriate for the applied procedure. All notable changes are listed below.

PDF The uncertainty due to the PDFs is $\pm 1.1 \times 10^{-2}$ on αP and $\pm 1 \times 10^{-3}$ on $A_{FB}^{\hat{N}}$ [117].

W+JETS HEAVY FLAVOR COMPOSITION The uncertainty on the flavor composition correction factors shown in table 16 is evaluated by changing κ_c up and down by 50% while keeping the total *W*-jets yield constant [106, 118]. Since the light flavor contribution is negligible κ_b will compensate the variation in κ_c.

MC STATISTICS The statistical uncertainty introduced by the MC samples is evaluated by varying the MC within the uncertainties while performing pseudo-experiments.

The effects of each systematic on the measured polarization and $A_{FB}^{\hat{N}}$ are shown in tables 24 and 25. For the polarization measurement the jet energy scale is the largest contributor to the uncertainty, while for the $A_{FB}^{\hat{N}}$ this is the MC statistics.

6.6.1 *Pile-up check*

As MC samples are generated with a preliminary pile-up distribution (see section 3.1.1) before the data-taking, the simulated pile-up distribution does not match that of data. Therefore the MC samples are reweighted such that the distributions of the number of reconstructed vertices per event are equal in data and MC. After this reweighting there is a significant discrepancy between data and MC in the distribution of the average number of interactions per bunch crossing ($\langle\mu\rangle$), as shown in figure 44. The effects of this discrepancy should be absorbed in the energy calibrations and efficiencies of the MC. This section describes an additional check of this discrepancy.

The discrepancy is large in the tails of the distribution, while in the center the agreement is good. We see the same discrepancy in both the preselection pretag and the selection distributions, so $\langle\mu\rangle$ does not correlate with the b-tag requirement or any of the cuts made in the selection.

As a cross-check, in order to see if the discrepancy has any effect on the analysis, the analysis is repeated on the central 80% of the $\langle\mu\rangle$ distribution: on each side 10% of the events are removed. Separate cut values are determined for data and MC, these are shown in table 26. Since $\langle\mu\rangle$ is stored as an integer the resulting accepted ranges are $\langle\mu\rangle \in [13, 28]$ for data and $\langle\mu\rangle \in [13, 26]$ for MC, and the resulting samples do not contain exactly 80% of the events of the full samples.

The results of the folding on the central $\langle\mu\rangle$ distribution are $\alpha P = 0.982$ for the electron channel and $\alpha P = 1.048$ for the muon channel. Since the results show variations that lie well within the systematic uncertainties of the analysis (e.g. the jet energy scale uncertainty alone is significantly larger than this effect), the discrepancy is assumed to be correctly absorbed in the MC, and to have no effect on the measurement.

	electron		muon		combined	
$\times 10^{-2}$	up	down	up	down	up	down
luminosity	−1.1	+1.2	−1.0	+1.1	−0.9	+0.9
jet energy scale	+13.9	−13.0	+14.3	−17.4	+16.2	−15.8
jet energy resolution	+12.4	−12.4	−5.5	+5.5	+3.5	−3.5
jet reconstruction	−0.1	+0.1	−2.4	+2.4	−1.3	+1.3
b-tag rate	−2.0	+2.2	−1.9	+2.1	−1.9	+2.1
c-tag rate	−0.5	+0.5	−0.9	+1.0	−0.8	+0.8
mistag rate	+0.6	−0.4	+1.1	−1.1	+1.2	−1.1
electron energy scale	+2.8	−5.4	—	—	+1.7	−2.1
electron energy resolution	−3.3	−2.4	—	—	−1.0	−0.5
electron trigger	−0.2	+0.2	—	—	−0.1	+0.1
muon energy scale	—	—	−3.4	−0.1	−1.8	+0.4
muon energy resolution	—	—	−2.3	−3.3	−0.8	−1.7
muon trigger	—	—	−0.2	+0.2	−0.1	+0.1
soft jet scale	−2.3	−3.9	+2.3	−5.8	+0.5	−4.8
soft jet resolution	−4.7	−3.5	−3.0	−9.0	−2.6	−5.2
t-channel Powheg	−2.1	+2.1	−7.6	+7.6	−5.5	+5.5
top pair MC@NLO	−3.9	+3.9	−4.0	+4.0	−3.9	+3.9
W+jets, Z+jets Alpgen	+3.8	−3.8	+5.2	−5.2	+5.5	−5.5
W+jets composition	−4.9	+5.5	−11.5	+6.3	−8.4	+5.9
PDF	+1.1	−1.1	+1.1	−1.1	+1.1	−1.1
top pair cross section	−2.0	+2.1	−1.7	+1.8	−1.7	+1.8
Wt-channel cross section	−0.2	+0.2	−0.3	+0.3	−0.2	+0.2
s-channel cross section	+0.0	−0.0	+0.0	−0.0	+0.0	−0.0
W+jets cross section	+0.2	−0.2	+0.2	−0.2	+0.3	−0.3
Z+jets cross section	+0.5	−0.5	−0.5	+0.5	+0.1	−0.1
diboson cross section	+0.0	−0.0	−0.1	+0.1	−0.1	+0.1
QCD multijet normalization	+1.9	−2.0	+0.1	−0.1	+1.0	−1.0
MC statistics	+5.0	−5.0	+6.5	−6.5	+4.8	−4.8
total	+21.5	−22.9	+21.1	−27.9	+20.7	−22.7

Table 24: Absolute effects ($\times 10^{-2}$) of each systematic uncertainty on the expected polarization. Uncertainties without individual up and down variations are symmetrized.

	electron		muon		combined	
$\times 10^{-3}$	up	down	up	down	up	down
luminosity	−0.2	+0.2	+0.0	−0.0	−0.1	+0.0
jet energy scale	−11.2	+3.3	+6.5	+0.2	−1.5	+1.4
jet energy resolution	+6.8	−6.8	+10.3	−10.3	+8.6	−8.6
jet reconstruction	+0.8	−0.8	−0.6	+0.6	−0.0	+0.0
b-tag rate	−0.2	+0.2	−0.2	+0.2	−0.2	+0.2
c-tag rate	+0.3	−0.3	+1.4	−1.4	+0.9	−0.9
mistag rate	−0.7	+0.4	−0.6	+0.8	−0.6	+0.6
electron energy scale	−3.7	+4.1	—	—	−1.6	+1.9
electron energy resolution	+1.6	−3.1	—	—	+0.8	−1.3
electron trigger	−0.1	+0.0	—	—	−0.0	−0.0
muon energy scale	—	—	−3.3	+1.3	−1.9	+0.8
muon energy resolution	—	—	−0.3	−0.5	−0.3	−0.3
muon trigger	—	—	+0.0	−0.0	+0.0	−0.0
soft jet scale	−1.4	+5.3	−0.0	+1.1	−0.6	+2.9
soft jet resolution	+1.4	+6.9	+0.4	+4.4	+0.9	+5.7
t-channel Powheg	−2.1	+2.1	+2.3	−2.3	+0.3	−0.3
top pair MC@NLO	−6.6	+6.6	+11.4	−11.4	+3.6	−3.6
W+jets, Z+jets Alpgen	+2.1	−2.1	−6.4	+6.4	−2.5	+2.5
W+jets composition	+0.7	−0.7	+1.8	−0.8	+1.4	−0.8
PDF	+1.0	−1.0	+1.0	−1.0	+1.0	−1.0
top pair cross section	−0.5	+0.6	−0.2	+0.2	−0.4	+0.3
Wt-channel cross section	+0.2	−0.2	+0.1	−0.1	+0.2	−0.2
s-channel cross section	+0.0	−0.0	−0.0	+0.0	+0.0	−0.0
W+jets cross section	+0.1	−0.1	+0.0	−0.0	+0.0	−0.1
Z+jets cross section	−0.2	+0.2	+1.4	−1.4	+0.7	−0.7
diboson cross section	−0.2	+0.2	−0.2	+0.2	−0.2	+0.1
QCD multijet normalization	+1.3	−1.4	+2.1	−2.1	+1.6	−1.8
MC statistics	+14.0	−14.0	+12.8	−12.8	+11.8	−11.8
total	+20.2	−21.2	+22.9	−21.7	+19.9	−19.0

Table 25: Absolute effects ($\times 10^{-3}$) of each systematic uncertainty on the expected $A_{\mathrm{FB}}^{\hat{\mathrm{N}}}$. Uncertainties without individual up and down variations are symmetrized.

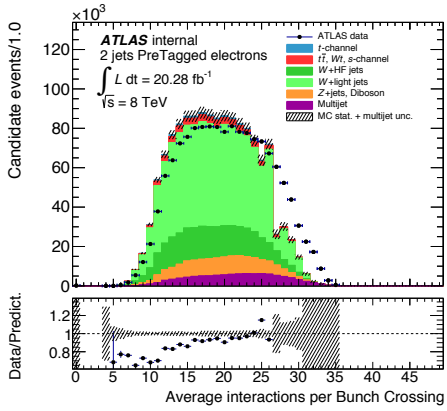

(a) Electron channel, preselection pretag.

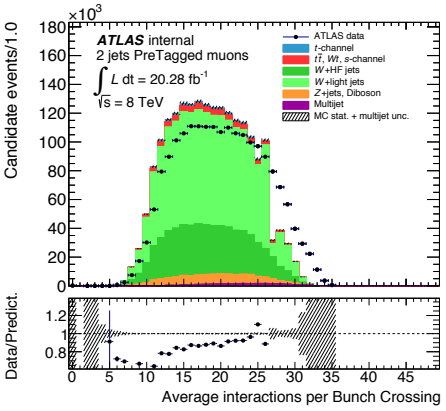

(b) Muon channel, preselection pretag.

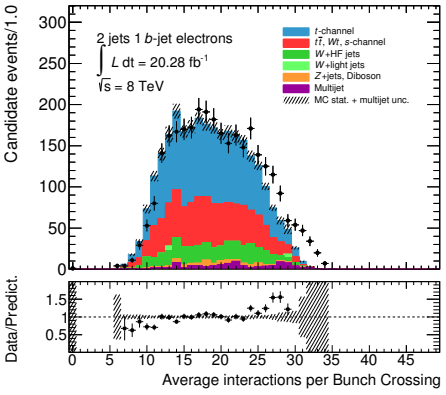

(c) Electron channel, selection.

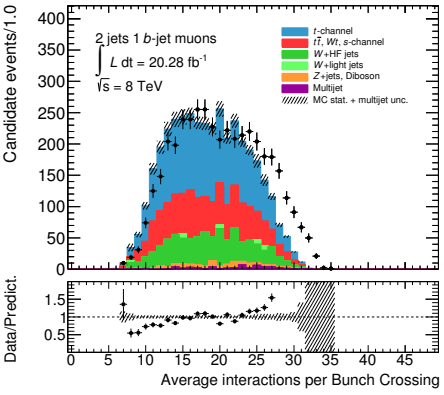

(d) Muon channel, selection.

Figure 44: Distributions of the number of average interactions per bunch crossing. The large discrepancies are an effect of the reweighting of the events to the distribution of the number of reconstructed vertices per event in data.

data:	$12.97 \leqslant \langle \mu \rangle < 28.38$
MC:	$12.20 \leqslant \langle \mu \rangle < 26.28$

Table 26: Central $\langle \mu \rangle$ ranges.

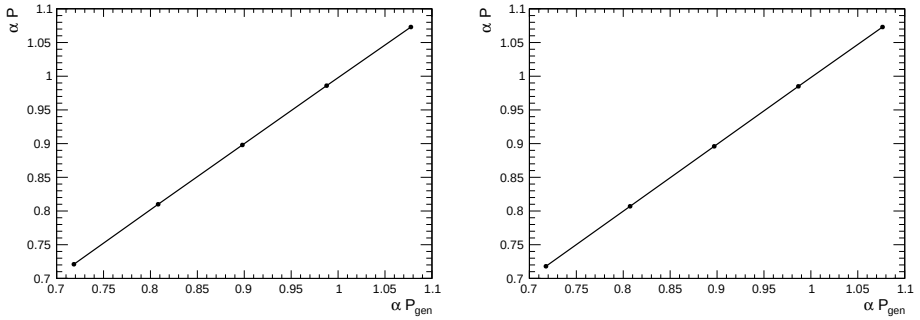

(a) Electron channel. (b) Muon channel.

Figure 45: Response of the folding procedure to obtain the polarization on reweighted signal samples with generator-level polarization at 80%, 90%, 100%, 110% and 120% of the SM value.

6.7 LINEARITY

In order to measure the dependence of the measurement on anomalous couplings the signal events are reweighted to form alternative angular distributions of $\cos\theta^{x}$ and $\cos\theta^{\hat{N}}$ with a different polarization or different W boson helicity fractions respectively.

Figure 45 shows the results of the polarization measurement using folding on four reweighted samples and the nominal sample, with generator-level αP between 80% and 120% of the SM value with steps of 10%. The response is linear, and $\Delta\alpha P/\Delta\alpha P_{\text{gen}} = 1$ at sub-percent level.

To measure the linearity of the W boson polarization in the normal frame measurement, the signal sample is reweighted such that $\tilde{F}_{-}^{\hat{N}}$ is varied from 80% to 120% with 10% steps, while keeping $\tilde{F}_{0}^{\hat{N}}$ constant. As a result, $\tilde{F}_{+}^{\hat{N}}$ changes to satisfy equation 6. The results are shown in figure 46. Again the response is linear, and $\Delta\tilde{F}_{-}^{\hat{N}}/\Delta\{\tilde{F}_{-}^{\hat{N}}\}_{\text{gen}} = 1$ at sub-percent level.

The dependence of the polarization measurement on the W helicity fractions can be determined by using the $\tilde{F}_{-}^{\hat{N}}$-reweighted samples for the polarization measurement. The results are shown in figure 47, and figure 48 shows the folding response of the W helicity fraction measurement on the polarization-reweighted samples. These plots show some cross-talk between the two quantities. As these effects are much smaller than the accuracy of the measurement, these effects are neglected.

6.8 CROSS SECTION MEASUREMENT

The normalization of the signal as determined in the likelihood fit in section 6.3.1 can be used to obtain a measurement of the t-channel cross section. Using $\sigma_{mc} = 87.76$ pb the following results are obtained:

$$\sigma_{t-channel} = 100.4 \pm 4.1(stat)^{+9.4}_{-8.4}(sys)^{+26.1}_{-26.1}(th) \text{ pb (electron)}, \quad (60)$$

$$\sigma_{t-channel} = 103.5 \pm 3.8(stat)^{+10.7}_{-12.5}(sys)^{+23.4}_{-22.9}(th) \text{ pb (muon)}, \quad (61)$$

$$\sigma_{t-channel} = 101.9 \pm 2.8(stat)^{+10.0}_{-10.2}(sys)^{+24.5}_{-24.3}(th) \text{ pb (combined)}, \quad (62)$$

where the theory uncertainty consists of the t-channel Powheg, top pair MC@NLO and W/Z+jets Alpgen variations, the W+jets composition and the PDF uncertainty. These results are compatible with and comparable to those presented in chapter 5. A full breakdown of all systematic uncertainties is provided in table 27. The t-channel Powheg variation is, just as in section 5.5, by far the largest uncertainty. A combined result of $\sigma_{t-channel} = 101.9 \pm 2.8(stat)^{+10.0}_{-10.2}(sys)^{+4.7}_{-3.7}(th)$ pb is found when this uncertainty is ignored, which is significantly better than the result of the previous chapter. It should be noted that the number of measured t-channel events changes with less than 3% when using Powheg as t-channel generator instead of AcerMC, but that the resulting cross section varies by more than 20% due to the different MC efficiencies.

6.9 OVERVIEW OF THE RESULTS

Including the systematic and theory uncertainties described above the following results are obtained for the top polarization:

$$P = 0.946 \pm 0.097(stat)^{+0.200}_{-0.215}(sys)^{+0.081}_{-0.077}(th) \text{ (electron)}, \quad (63)$$

$$P = 0.893 \pm 0.084(stat)^{+0.174}_{-0.233}(sys)^{+0.119}_{-0.153}(th) \text{ (muon)}, \quad (64)$$

$$P = 0.924 \pm 0.068(stat)^{+0.178}_{-0.191}(sys)^{+0.106}_{-0.122}(th) \text{ (combined)}, \quad (65)$$

and for the forward-backward asymmetry:

$$A^{\hat{N}}_{FB} = -0.026 \pm 0.064(stat)^{+0.019}_{-0.020}(sys)^{+0.007}_{-0.007}(th) \text{ (electron)}, \quad (66)$$

$$A^{\hat{N}}_{FB} = -0.012 \pm 0.058(stat)^{+0.019}_{-0.017}(sys)^{+0.013}_{-0.013}(th) \text{ (muon)}, \quad (67)$$

$$A^{\hat{N}}_{FB} = -0.018 \pm 0.044(stat)^{+0.019}_{-0.018}(sys)^{+0.005}_{-0.005}(th) \text{ (combined)}. \quad (68)$$

A similar analysis to the one described in this chapter has been performed on the $\sqrt{s} = 7$ TeV dataset recorded by ATLAS [116]. This analysis uses an unfolding rather than folding method in order to measure $A^{\hat{N}}_{FB}$. The results are consistent and compatible with the results described above:

$$A^{\hat{N}}_{FB} = 0.031 \pm 0.065(stat)^{+0.029}_{-0.031}(sys). \quad (69)$$

The uncertainties of this analysis are larger than those of the analysis described above. This is partly explained by the fact that the $\sqrt{s} = 7$ TeV dataset is smaller than the $\sqrt{s} = 8$ TeV

	electron		muon		combined	
	up	down	up	down	up	down
luminosity	+3.8%	−3.8%	+3.7%	−3.7%	+3.6%	−3.6%
jet energy scale	+3.5%	−3.1%	−4.5%	−3.6%	−2.6%	−3.4%
jet energy resolution	−2.0%	+2.0%	−8.0%	+8.0%	−6.1%	+6.1%
jet reconstruction	−0.1%	+0.1%	−0.7%	+0.7%	−0.5%	+0.5%
b-tag rate	+4.7%	−4.7%	+4.5%	−4.5%	+4.5%	−4.5%
c-tag rate	+0.0%	−0.0%	+0.2%	−0.2%	+0.2%	−0.2%
mistag rate	−0.3%	+0.2%	−0.4%	+0.4%	−0.6%	+0.6%
electron energy scale	−3.5%	+3.8%	—	—	−1.8%	+1.1%
electron energy resolution	+1.4%	+0.7%	—	—	+0.2%	−0.2%
electron trigger	+0.3%	−0.3%	—	—	−0.1%	+0.1%
muon energy scale	—	—	+0.6%	−0.7%	+0.3%	−0.8%
muon energy resolution	—	—	+1.5%	−1.4%	+0.7%	−0.9%
muon trigger	—	—	+0.5%	−0.5%	+0.3%	−0.3%
soft jet scale	+1.7%	−0.4%	−1.1%	−2.3%	−0.1%	−1.3%
soft jet resolution	+2.8%	+1.0%	−0.3%	+1.1%	+0.2%	−0.2%
t-channel Powheg	+25.6%	−25.6%	+21.5%	−21.5%	+23.6%	−23.6%
top pair MC@NLO	+2.7%	−2.7%	+0.8%	−0.8%	+1.4%	−1.4%
W+jets, Z+jets Alpgen	+3.3%	−3.3%	−4.3%	+4.3%	−2.3%	+2.3%
W+jets composition	+1.3%	−1.5%	+5.2%	−2.7%	+3.5%	−2.1%
PDF	+1.1%	−1.1%	+1.1%	−1.1%	+1.1%	−1.1%
top pair cross section	+1.7%	−1.7%	+1.5%	−1.5%	+1.4%	−1.4%
Wt-channel cross section	+0.2%	−0.2%	+0.2%	−0.2%	+0.2%	−0.2%
s-channel cross section	+0.0%	−0.0%	+0.0%	−0.0%	+0.0%	−0.0%
W+jets cross section	−0.1%	+0.2%	−0.1%	+0.1%	−0.2%	+0.2%
Z+jets cross section	+0.1%	−0.1%	+0.3%	−0.3%	+0.1%	−0.1%
diboson cross section	−0.0%	+0.0%	+0.0%	−0.0%	−0.0%	+0.0%
QCD multijet normalization	+1.5%	−1.5%	+0.7%	−0.7%	+0.8%	−0.8%
MC statistics	+1.5%	−1.5%	+3.5%	−3.5%	+3.0%	−3.0%
total	+27.7%	−27.3%	+24.9%	−25.2%	+25.6%	−25.9%

Table 27: Effects of each systematic uncertainty on the expected t-channel cross section. Uncertainties without individual up and down variations are symmetrized.

dataset used for the analysis described in this chapter. All results are fully compatible with the SM within the uncertainties.

Using equation 12, the measurements (with both lepton channels combined) can be combined to obtain $\mathfrak{I}(g_R)$:

$$\mathfrak{I}(g_R) = -0.030 \pm 0.074(\text{stat})^{+0.025}_{-0.023}(\text{sys})^{+0.008}_{-0.008}(\text{th}), \tag{70}$$

where the systematic uncertainties have been evaluated simultaneously in order to correctly treat correlations.

The result is fully compatible with the SM ($\mathfrak{I}(g_R) = 0$) within the uncertainty. No CP-violation is observed.

Measurements of the W boson polarization in top decays have also been performed in $t\bar{t}$ processes by ATLAS and CMS [119]. The resulting helicity fractions can be combined to a measurement of the real part of g_R:

$$\mathfrak{R}(g_R) = -0.10 \pm 0.06(\text{stat})^{+0.07}_{-0.08}(\text{sys}). \tag{71}$$

Also this measurement is compatible with the SM.

6.10 CONCLUSION

In this chapter the results of an analysis in the single top t-channel on data with $\sqrt{s} = 8$ TeV/c^2 are presented. These results are threefold: a measurement of the t-channel cross section, a measurement of the top quark polarization and a measurement of the forward-backward asymmetry in the normal frame. This last quantity is a sensitive probe to the imaginary part of the coupling constant g_R, which is zero in the SM. A non-zero $\mathfrak{I}(g_R)$ would imply CP-violation, making this a quantity of particular interest.

The cross section result is $\sigma_{t-\text{channel}} = 101.9 \pm 2.8(\text{stat})^{+10.0}_{-10.2}(\text{sys})^{+24.5}_{-24.3}(\text{th})$ pb, which is consistent with the result presented in chapter 5 and the SM. The uncertainty on the cross section measurement is rather large, mainly due to the t-channel generator systematic uncertainty. This uncertainty is estimated from the difference in cross section predicted by AcerMC (leading order) and Powheg (next-to-leading order). It is common knowledge that leading order generators describe distributions reasonably well, but their cross section predictions suffer from relatively large uncertainties. It may be somewhat conservative to quote the full difference between leading order and next-to-leading order as systematic uncertainty. When we remove this uncertainty we obtain $\sigma_{t-\text{channel}} = 101.9 \pm 2.8(\text{stat})^{+10.0}_{-10.2}(\text{sys})^{+4.7}_{-3.7}(\text{th})$ pb.

Any future t-channel cross section measurement would benefit from using a next-to-leading order generator as default generator for the t-channel. This is a big future challenge, because the smearing matrix needed for the analysis presented here is non-trivial to construct in a next-to-leading order interpretation. Therefore the smearing matrix used here is always obtained from AcerMC, which is expected to be accurate for this purpose, based on the agreement of the predicted and observed control distributions shown in this thesis.

While the polarization measurement ($P = 0.924 \pm 0.068(\text{stat})^{+0.178}_{-0.191}(\text{sys})^{+0.106}_{-0.122}(\text{th})$) is mainly limited by systematic uncertainties, the forward-backward asymmetry measurement ($A^{\hat{N}}_{FB} = -0.018 \pm 0.044(\text{stat})^{+0.019}_{-0.018}(\text{sys})^{+0.005}_{-0.005}(\text{th})$) is limited by statistics.

The measurement of $\mathcal{I}(g_R)$ is a combination of these two:

$$\mathcal{I}(g_R) = -0.030 \pm 0.074(\text{stat})^{+0.025}_{-0.023}(\text{sys})^{+0.008}_{-0.008}(\text{th}).$$

All quantities have also been extracted for the electron and muon samples individually, which has led to consistent results. Moreover, all results appear to be consistent with the SM expectations.

The measured uncertainty on $\mathcal{I}(g_R)$ is limited by statistics and would improve when more data comes available. During printing of this thesis the LHC has resumed after a shutdown of a year to run at $\sqrt{s} = 13$ TeV/c^2. It will be exciting for a follow-up analysis to be able to use a larger dataset at this higher energy.

The measurement of $\mathcal{I}(g_R)$ is sensitive to a CP-violating coupling in the Wtb vertex. An additional source of CP-violation leads to an asymmetric baryogenesis which can explain the existence of matter and the absence of anti-matter in our universe, which is still one of the biggest questions of science. The results obtained in this analysis are consistent with $\mathcal{I}(g_R) = 0$ and thus no hints of CP-violation have been observed. However, the Wtb vertex can still provide a significant source of CP-violation and the hypothesis for the baryogenesis is not yet ruled out. It may well be that future LHC data provides the answer to this big question.

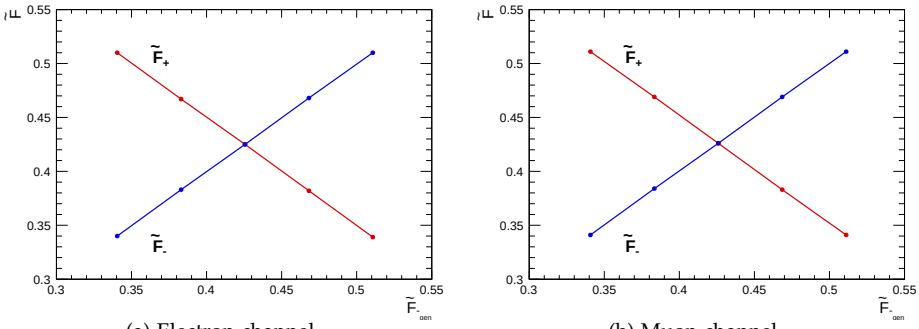

(a) Electron channel. (b) Muon channel.

Figure 46: Response of the folding procedure to obtain the W helicity on reweighted signal samples with generator-level $\tilde{F}_-^N$ at 80%, 90%, 100%, 110% and 120% of the SM value.

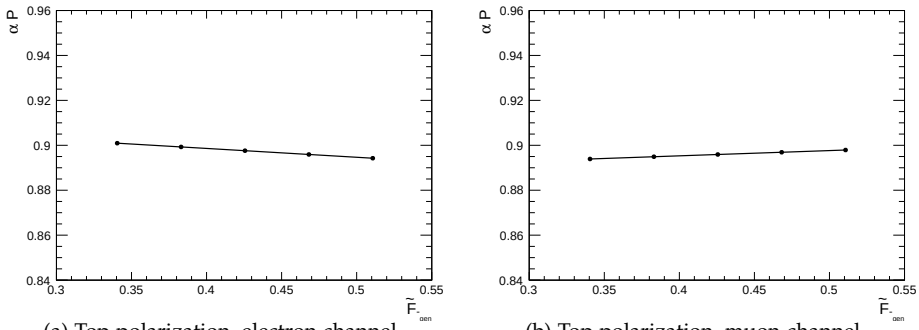

(a) Top polarization, electron channel. (b) Top polarization, muon channel.

Figure 47: Folding response of the polarization on W polarization in the normal frame-reweighted signal samples.

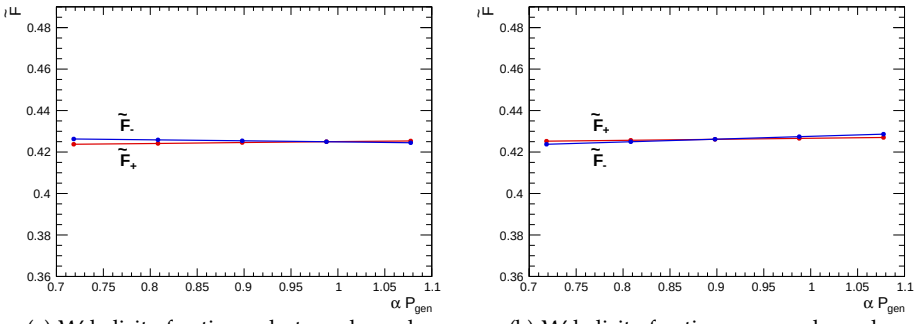

(a) W helicity fractions, electron channel. (b) W helicity fractions, muon channel.

Figure 48: Folding response of the W helicity fractions on polarization-reweighted signal samples.

A

WIGNER ROTATION

Classical Galilean transformations are composed of translations and rotations. Galilean translations and rotations each form a mathematical group. The combination of two successive translations is a translation, and the combination of two successive rotations is a rotation. In relativistic space-time this is no longer the case: two successive Lorentz boosts are only equal to a Lorentz boost if the directions of the boosts are parallel, and hence Lorentz boosts do not form a group.

In order to see this we first have a look at the nature of a Lorentz boost. The Lorentz boost with velocity β in the x-direction can be written as:

$$\begin{pmatrix} ct' \\ x' \\ y' \\ z' \end{pmatrix} = \begin{pmatrix} \gamma_1 & -\gamma_1\beta_1 & 0 & 0 \\ -\gamma_1\beta_1 & \gamma_1 & 0 & 0 \\ 0 & 0 & 1 & 0 \\ 0 & 0 & 0 & 1 \end{pmatrix} \begin{pmatrix} ct \\ x \\ y \\ z \end{pmatrix}, \tag{72}$$

where we see that this involves a symmetric matrix. If B_x is the boost along the x-axis then we can construct a boost in any direction by rotating B_x using a rotation matrix R: $B' = RB_xR^{-1}$. As the result of rotating a symmetric matrix is also a symmetric matrix[1], B' is symmetric. As any boost can be constructed with combination of a rotation R and a boost along the x-axis B_x, the matrix of any Lorentz boost is symmetric.

Now we consider two boosts along directions that are not parallel. For simplicity we look at orthogonal boosts along the x- and y-axes: B_1 and B_2 with boost vectors $\vec{\beta}_1 = \beta_1\hat{x}$ and $\vec{\beta}_2 = \beta_2\hat{y}$ respectively:

$$B_1 = \begin{pmatrix} \gamma_1 & -\gamma_1\beta_1 & 0 & 0 \\ -\gamma_1\beta_1 & \gamma_1 & 0 & 0 \\ 0 & 0 & 1 & 0 \\ 0 & 0 & 0 & 1 \end{pmatrix}, \quad B_2 = \begin{pmatrix} \gamma_2 & 0 & -\gamma_2\beta_2 & 0 \\ 0 & 1 & 0 & 0 \\ -\gamma_2\beta_2 & 0 & \gamma_2 & 0 \\ 0 & 0 & 0 & 1 \end{pmatrix}. \tag{73}$$

1 Any matrix B congruent to a symmetric matrix A is symmetric (B is symmetric if $B = RAR^T$ for any matrix R). As rotations are orthogonal ($R^TR = I$ for any rotation R), any matrix obtained by rotating a symmetric matrix is symmetric.

Consecutive application of these boosts results in:

$$B_2\,B_1 = \begin{pmatrix} \gamma_1\gamma_2 & -\gamma_1\gamma_2\beta_1 & -\gamma_2\beta_2 & 0 \\ -\gamma_1\beta_1 & \gamma_1 & 0 & 0 \\ -\gamma_1\gamma_2\beta_2 & \gamma_1\gamma_2\beta_1\beta_2 & \gamma_2 & 0 \\ 0 & 0 & 0 & 1 \end{pmatrix}, \tag{74}$$

which is clearly an asymmetrical matrix, and hence can not be a Lorentz boost. The result can however be written as the combination of a successive boost B_{12} and a rotation R called a *Wigner rotation* [120, 121]. In this specific case R is a rotation in the x-y-plane with angle

$$\theta = \arctan\left(-\frac{\gamma_1\gamma_2\beta_1\beta_2}{\gamma_1+\gamma_2}\right), \tag{75}$$

given by

$$R = \begin{pmatrix} 1 & 0 & 0 & 0 \\ 0 & \cos\theta & \sin\theta & 0 \\ 0 & -\sin\theta & \cos\theta & 0 \\ 0 & 0 & 0 & 1 \end{pmatrix}, \tag{76}$$

and B_{12}, which obeys $RB_{12} = B_2B_1$, is given by the symmetric matrix:

$$B_{12} = \begin{pmatrix} \gamma_1\gamma_2 & -\gamma_1\gamma_2\beta_1 & -\gamma_2\beta_2 & 0 \\ -\gamma_1\gamma_2\beta_1 & -\gamma_2\cos\theta & -\gamma_2\sin\theta & 0 \\ -\gamma_2\beta_2 & -\gamma_2\sin\theta & \gamma_2\cos\theta & 0 \\ 0 & 0 & 0 & 1 \end{pmatrix}. \tag{77}$$

From this matrix we find that $\gamma_{12} = \gamma_1\gamma_2$ and $\beta_{12} = \beta_1\hat{x} + \beta_2/\gamma_1\hat{y}$. A graphical representation of the given example is shown in figure 49.

Since any rotation can be combined with the Wigner rotation to form one rotation, Lorentz *transformations*, combinations of a Lorentz boost and a rotation, do form a group.

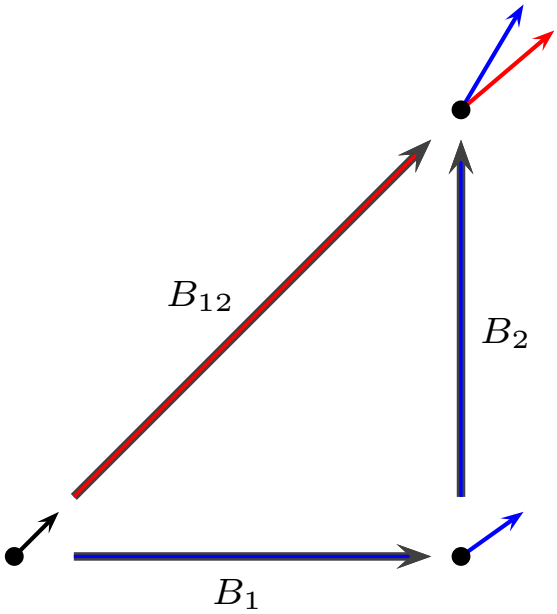

Figure 49: A graphical representation of the Wigner rotation for $\vec{\beta}_1 = 0.7\hat{x}$ and $\vec{\beta}_2 = 0.7\hat{y}$. When the original vector is boosted with B_1 and B_2 successively the resulting vector (shown in blue) is rotated with respect to the result of the combined boost B_{12} (shown in red). Note that, although printed diagonally, boost B_{12} has unequal x- and y-components: $\vec{\beta}_{12} = 0.7\hat{x} + 0.5\hat{y}$.

BIBLIOGRAPHY

[1] S. Weinberg, *A Model of Leptons*, Phys. Rev. Lett. **19** (1967) 1264–1266.

[2] S. L. Glashow, J. Iliopoulos, and L. Maiani, *Weak Interactions with Lepton-Hadron Symmetry*, Phys. Rev. **D2** (1970) 1285–1292.

[3] M. K. Gaillard, P. D. Grannis, and F. J. Sciulli, *The Standard model of particle physics*, Rev. Mod. Phys. **71** (1999) S96–S111, arXiv:hep-ph/9812285 [hep-ph].

[4] S. Novaes, *Standard model: An Introduction*, arXiv:hep-ph/0001283 [hep-ph].

[5] ATLAS Collaboration, G. Aad et al., *Observation of a new particle in the search for the Standard Model Higgs boson with the ATLAS detector at the LHC*, Phys. Lett. **B716** (2012) 1–29, arXiv:1207.7214 [hep-ex].

[6] CMS Collaboration, S. Chatrchyan et al., *Observation of a new boson at a mass of 125 GeV with the CMS experiment at the LHC*, Phys. Lett. **B716** (2012) 30–61, arXiv:1207.7235 [hep-ex].

[7] M. E. Peskin and D. V. Schroeder, *An Introduction to Quantum Field Theory*. Westview Press, 1995.

[8] G. R. Farrar and M. E. Shaposhnikov, *Baryon asymmetry of the Universe in the minimal standard model*, Phys. Rev. Lett. **70** (1993) 2833–2836.

[9] A. H. G. Peter, *Dark Matter: A Brief Review*, arXiv (2012), arXiv:1201.3942 [astro-ph.CO].

[10] S. Dawson, *SUSY and such*, NATO Sci. Ser. **B365** (1997) 33–80, arXiv:hep-ph/9612229 [hep-ph].

[11] D. Tong, *String Theory*, arXiv:0908.0333 [hep-th].

[12] A. Sakharov, *Violation of CP Invariance, c Asymmetry, and Baryon Asymmetry of the Universe*, Pisma Zh. Eksp. Teor. Fiz. **5** (1967) 32–35.

[13] G. 't Hooft, *Symmetry Breaking through Bell-Jackiw Anomalies*, Phys. Rev. Lett. **37** (1976) 8–11.

[14] M. Kobayashi and T. Maskawa, *CP Violation in the Renormalizable Theory of Weak Interaction*, Prog. Theor. Phys. **49** (1973) 652–657.

[15] Particle Data Group Collaboration, K. Olive et al., *Review of Particle Physics*, Chinese Physics C **38** no. 9, (2014) 090001.

[16] W.-S. Hou, *Source of CP Violation for the Baryon Asymmetry of the Universe*, Chin. J. Phys. **47** (2009) 134, arXiv:0803.1234 [hep-ph].

[17] T. M. Tait and C.-P. Yuan, *Single top quark production as a window to physics beyond the standard model*, Phys. Rev. **D63** (2000) 014018, arXiv:hep-ph/0007298 [hep-ph].

[18] DØ Collaboration, S. Abachi et al., *Observation of the Top Quark*, Phys. Rev. Lett. **74** (1995) 2632–2637.

[19] CDF Collaboration, F. Abe et al., *Observation of Top Quark Production in $\bar{p}p$ Collisions with the Collider Detector at Fermilab*, Phys. Rev. Lett. **74** (1995) 2626–2631.

[20] Tevatron Electroweak Working Group, CDF and DØ Collaborations, *Combination of CDF and Do results on the mass of the top quark using up to 5.8 fb^{-1} of data*, arXiv:1107.5255 [hep-ex].

[21] *Summary plots from the ATLAS Top physics group*, May, 2015. https://atlas.web.cern.ch/Atlas/GROUPS/PHYSICS/CombinedSummaryPlots/TOP/.

[22] CDF and DØ Collaborations, *Combination of measurements of the top-quark pair production cross section from the Tevatron Collider*, Phys. Rev. **D89** (2014) 072001, arXiv:1309.7570 [hep-ex].

[23] ATLAS Collaboration, G. Aad et al., *Combination of ATLAS and CMS top-quark pair cross section measurements using up to 1.1 fb^{-1} of data at 7 TeV*, Tech. Rep. ATLAS-CONF-2012-134, CERN, Geneva, Sep, 2012.

[24] ATLAS Collaboration, G. Aad et al., *Measurement of the $t\bar{t}$ production cross-section in pp collisions at $\sqrt{s} = 8$ TeV using $e\mu$ events with b-tagged jets*, Tech. Rep. ATLAS-CONF-2013-097, CERN, Geneva, Sep, 2013.

[25] CDF and DØ Collaborations, *Observation of s-channel production of single top quarks at the Tevatron*, Phys. Rev. Lett. **112** (2014) 231803, arXiv:1402.5126 [hep-ex].

[26] N. Kidonakis, *NNLL resummation for s-channel single top quark production*, Phys. Rev. **D81** (2010) 054028, arXiv:1001.5034 [hep-ph].

[27] CDF and DØ Collaborations, *Single top quark production cross section at the Tevatron*, arXiv:1310.3420 [hep-ex].

[28] ATLAS Collaboration, G. Aad et al., *Measurement of the t-channel single top-quark and top-antiquark production cross-sections and their ratio in pp collisions at $\sqrt{s} = 7$ TeV*, Tech. Rep. ATLAS-CONF-2012-056, CERN, Geneva, Jun, 2012.

[29] ATLAS and CMS Collaborations, *Combination of single top-quark cross-sections measurements in the t-channel at $\sqrt{s} = 8$ TeV with the ATLAS and CMS experiments*, Tech. Rep. CMS-PAS-TOP-12-002, ATLAS-CONF-2013-098, CERN, Geneva, Sep, 2013.

[30] N. Kidonakis, *Single top quark production at the Fermilab Tevatron: Threshold resummation and finite-order soft gluon corrections*, Phys. Rev. D **74** (2006) 114012.

[31] ATLAS Collaboration, G. Aad et al., *Evidence for the associated production of a W boson and a top quark in ATLAS at $\sqrt{s} = 7$ TeV*, Phys. Lett. **B716** (2012) 142–159, arXiv:1205.5764 [hep-ex].

[32] CMS Collaboration, S. Chatrchyan et al., *Single Top associated tW production at* 8 TeV *in the two lepton final state*, Tech. Rep. CMS-PAS-TOP-12-040, CERN, Geneva, 2013.

[33] C. T. Hill and E. H. Simmons, *Strong dynamics and electroweak symmetry breaking*, Phys. Rept. **381** (2003) 235–402, arXiv:hep-ph/0203079 [hep-ph].

[34] S. P. Martin, *Extra vector-like matter and the lightest Higgs scalar boson mass in low-energy supersymmetry*, Phys. Rev. **D81** (2010) 035004, arXiv:0910.2732 [hep-ph].

[35] K. Kumar, W. Shepherd, T. M. Tait, and R. Vega-Morales, *Beautiful Mirrors at the LHC*, J. High Energy Phys. **1008** (2010) 052, arXiv:1004.4895 [hep-ph].

[36] B. Holdom, W. Hou, T. Hurth, M. Mangano, S. Sultansoy, et al., *Four Statements about the Fourth Generation*, PMC Phys. **A3** (2009) 4, arXiv:0904.4698 [hep-ph].

[37] A. K. Alok, A. Dighe, and D. London, *Constraints on the Four-Generation Quark Mixing Matrix from a Fit to Flavor-Physics Data*, Phys. Rev. **D83** (2011) 073008, arXiv:1011.2634 [hep-ph].

[38] A. de Rújula, L. Maiani, and R. Petronzio, *Search for excited quarks*, Phys. Lett. **B140** no. 3 - 4, (1984) 253 – 258.

[39] U. Baur, I. Hinchliffe, and D. Zeppenfeld, *Excited Quark Production at Hadron Colliders*, Int. J. Mod. Phys. **A2** (1987) 1285.

[40] J. Nutter, R. Schwienhorst, D. G. Walker, and J.-H. Yu, *Single Top Production as a Probe of B-prime Quarks*, Phys. Rev. **D86** (2012) 094006, arXiv:1207.5179 [hep-ph].

[41] I. Bigi, Y. Dokshitzer, V. Khoze, J. Kühn, and P. Zerwas, *Production and decay properties of ultra-heavy quarks*, Phys. Lett. **B181** no. 1-2, (1986) 157 – 163.

[42] G. Mahlon and S. J. Parke, *Single top quark production at the LHC: Understanding spin*, Phys. Lett. **B476** (2000) 323–330, arXiv:hep-ph/9912458 [hep-ph].

[43] C.-R. Chen, F. Larios, and C.-P. Yuan, *General analysis of single top production and W helicity in top decay*, Phys. Lett. **B631** no. 3, (2005) 126 – 132.

[44] J. Aguilar-Saavedra, *A Minimal set of top anomalous couplings*, Nucl. Phys. **B812** (2009) 181–204, arXiv:0811.3842 [hep-ph].

[45] J. Aguilar-Saavedra and J. Bernabeu, *W polarisation beyond helicity fractions in top quark decays*, Nucl. Phys. **B840** (2010) 349–378, arXiv:1005.5382 [hep-ph].

[46] R. Schwienhorst, C.-P. Yuan, C. Mueller, and Q.-H. Cao, *Single top quark production and decay in the* t*-channel at next-to-leading order at the LHC*, Phys. Rev. **D83** (2011) 034019, arXiv:1012.5132 [hep-ph].

[47] L. Evans and P. Bryant, *LHC Machine*, J. Instrum. **3** no. 08, (2008) S08001.

[48] CMS Collaboration, S. Chatrchyan et al., *The CMS experiment at the CERN LHC*, J. Instrum. **3** no. 08, (2008) S08004.

[49] LHCb Collaboration, A. Augusto Alves Jr et al., *The LHCb Detector at the LHC*, J. Instrum. 3 no. 08, (2008) S08005.

[50] ALICE Collaboration, K. Aamodt et al., *The ALICE experiment at the CERN LHC*, J. Instrum. 3 no. 08, (2008) S08002.

[51] ATLAS Collaboration, G. Aad et al., *The ATLAS Experiment at the CERN LHC*, J. Instrum. 3 no. 08, (2008) S08003.

[52] ATLAS Collaboration, *ATLAS inner detector: Technical Design Report*. Technical Design Report ATLAS. CERN, Geneva, 1997.

[53] P. Coe, *Frequency Scanning Interferometry - a Versatile, High Precision, Multiple Distance Measurement Technique*, eConf **C0211115** (2002) 017.

[54] ATLAS Collaboration, *ATLAS liquid-argon calorimeter: Technical Design Report*. Technical Design Report ATLAS. CERN, Geneva, 1996.

[55] ATLAS Collaboration, *ATLAS tile calorimeter: Technical Design Report*. Technical Design Report ATLAS. CERN, Geneva, 1996.

[56] ATLAS Collaboration, *ATLAS muon spectrometer: Technical Design Report*. Technical Design Report ATLAS. CERN, Geneva, 1997. distribution.

[57] ATLAS Collaboration, S. Aefsky, *Alignment of the Muon Spectrometer in ATLAS*, Tech. Rep. ATL-MUON-PROC-2011-003, CERN, Geneva, Sep, 2011.

[58] J. C. Barriere, F. Bauer, M. Fontaine, A. Formica, V. Gautard, P. F. Giraud, et al., *The alignment system of the barrel part of the ATLAS muon spectrometer*, Tech. Rep. ATL-MUON-PUB-2008-007, ATL-COM-MUON-2008-002, CERN, Geneva, Jan, 2008.

[59] S. Aefsky, C. Amelung, J. Bensinger, C. Blocker, A. Dushkin, M. Gardner, et al., *The Optical Alignment System of the ATLAS Muon Spectrometer Endcaps*, J. Instrum. 3 no. 11, (2008) P11005.

[60] H. van der Graaf, H. Groenstege, F. Linde, and P. Rewiersma, *RasNiK, an Alignment System for the ATLAS MDT Barrel Muon Chambers: Technical System Description*, http://cds.cern.ch/record/1073160 (2000). Revised version 2.0.

[61] P.-F. Giraud, *Muon Spectrometer alignment*, Presented at the ATLAS Weekly of March 11, 2004.

[62] ATLAS Collaboration, *ATLAS level-1 trigger: Technical Design Report*. Technical Design Report ATLAS. CERN, Geneva, 1998.

[63] ATLAS Collaboration, *ATLAS high-level trigger, data-acquisition and controls: Technical Design Report*. Technical Design Report ATLAS. CERN, Geneva, 2003.

[64] *AtlasTWiki - RunStatsPublicResults2010*, July, 2014. `https://twiki.cern.ch/twiki/bin/view/AtlasPublic/RunStatsPublicResults2010`.

[65] *AtlasTWiki - ApprovedPlotsATLASDetector*, Aug., 2014. https://twiki.cern.ch/twiki/bin/view/AtlasPublic/ApprovedPlotsATLASDetector.

[66] ATLAS Collaboration, G. Aad et al., *Electron performance measurements with the ATLAS detector using the 2010 LHC proton-proton collision data*, Eur. Phys. J. **C72** (2012) 1909, arXiv:1110.3174 [hep-ex].

[67] ATLAS Collaboration, G. Aad et al., *Electron efficiency measurements with the ATLAS detector using the 2012 LHC proton-proton collision data*, Tech. Rep. ATLAS-CONF-2014-032, CERN, Geneva, Jun, 2014.

[68] ATLAS Collaboration, G. Aad et al., *Electron reconstruction and identification efficiency measurements with the ATLAS detector using the 2011 LHC proton-proton collision data*, Eur. Phys. J. **C74** (2014) 38, arXiv:1404.2240 [hep-ex].

[69] ATLAS Collaboration, G. Aad et al., *Measurement of the muon reconstruction performance of the ATLAS detector using 2011 and 2012 LHC proton-proton collision data*, Eur. Phys. J. **C74** (2014) 3130, arXiv:1407.3935 [hep-ex].

[70] S. Hassani, L. Chevalier, E. Lancon, J. Laporte, R. Nicolaidou, et al., *A muon identification and combined reconstruction procedure for the ATLAS detector at the LHC using the (MUONBOY, STACO, MuTag) reconstruction packages*, Nucl. Instrum. Meth. **A572** (2007) 77–79.

[71] T. Lagouri, D. Adams, K. Assamagan, M. Biglietti, G. Carlino, et al., *A Muon Identification and Combined Reconstruction Procedure for the ATLAS Detector at the LHC at CERN*, IEEE Trans. Nucl. Sci. **51** (2004) 3030–3033.

[72] M. Cacciari, G. P. Salam, and G. Soyez, *The anti-k_t jet clustering algorithm*, J. High Energy Phys. **4** (2008) 63, arXiv:0802.1189 [hep-ph].

[73] ATLAS Collaboration, G. Aad et al., *Measuring the b-tag efficiency in a top-pair sample with 4.7 fb^{-1} of data from the ATLAS detector*, Tech. Rep. ATLAS-CONF-2012-097, CERN, Geneva, Jul, 2012.

[74] ATLAS Collaboration, G. Aad et al., *Jet energy measurement and its systematic uncertainty in proton-proton collisions at $\sqrt{s} = 7$ TeV with the ATLAS detector*, Eur. Phys. J. **C75** no. 1, (2015) 17, arXiv:1406.0076 [hep-ex].

[75] ATLAS Collaboration, G. Aad et al., *Calibration of the performance of* b*-tagging for* c *and light-flavour jets in the 2012 ATLAS data*, Tech. Rep. ATLAS-CONF-2014-046, CERN, Geneva, Jul, 2014.

[76] ATLAS Collaboration, G. Aad et al., *Performance of missing transverse momentum reconstruction in proton-proton collisions at $\sqrt{s} = 7$ TeV with ATLAS*, Eur. Phys. J. **C72** (2012) 1844, arXiv:1108.5602 [hep-ex].

[77] ATLAS Collaboration, G. Aad et al., *Performance of Missing Transverse Momentum Reconstruction in ATLAS studied in Proton-Proton Collisions recorded in 2012 at* 8 TeV, Tech. Rep. ATLAS-CONF-2013-082, CERN, Geneva, Aug, 2013.

[78] ATLAS Collaboration, G. Aad et al., *Performance of the Missing Transverse Energy Reconstruction and Calibration in Proton-Proton Collisions at a Center-of-Mass Energy of 7 TeV with the ATLAS Detector*, Tech. Rep. ATLAS-CONF-2010-057, CERN, Geneva, Jul, 2010.

[79] ATLAS Collaboration, G. Aad et al., *Performance of Missing Transverse Momentum Reconstruction in Proton-Proton Collisions at 7 TeV with ATLAS*, Eur. Phys. J. **C72** (2012) 1844, arXiv:1108.5602 [hep-ex].

[80] ATLAS Collaboration, G. Aad et al., *The ATLAS Simulation Infrastructure*, Eur. Phys. J. **C70** (2010) 823–874, arXiv:1005.4568 [physics.ins-det].

[81] T. Sjostrand, S. Mrenna, and P. Z. Skands, *PYTHIA 6.4 Physics and Manual*, J. High Energy Phys. **0605** (2006) 026, arXiv:hep-ph/0603175 [hep-ph].

[82] G. Corcella, I. Knowles, G. Marchesini, S. Moretti, K. Odagiri, et al., *HERWIG 6: An Event generator for hadron emission reactions with interfering gluons (including supersymmetric processes)*, J. High Energy Phys. **0101** (2001) 010, arXiv:hep-ph/0011363 [hep-ph].

[83] T. Gleisberg, S. Hoeche, F. Krauss, M. Schonherr, S. Schumann, et al., *Event generation with SHERPA 1.1*, J. High Energy Phys. **0902** (2009) 007, arXiv:0811.4622 [hep-ph].

[84] P. Nason, *A New method for combining NLO QCD with shower Monte Carlo algorithms*, J. High Energy Phys. **0411** (2004) 040, arXiv:hep-ph/0409146 [hep-ph].

[85] M. L. Mangano, M. Moretti, F. Piccinini, R. Pittau, and A. D. Polosa, *ALPGEN, a generator for hard multiparton processes in hadronic collisions*, J. High Energy Phys. **0307** (2003) 001, arXiv:hep-ph/0206293 [hep-ph].

[86] S. Frixione and B. R. Webber, *Matching NLO QCD computations and parton shower simulations*, J. High Energy Phys. **0206** (2002) 029, arXiv:hep-ph/0204244 [hep-ph].

[87] J. Alwall, M. Herquet, F. Maltoni, O. Mattelaer, and T. Stelzer, *MadGraph 5: Going Beyond*, J. High Energy Phys. **1106** (2011) 128, arXiv:1106.0522 [hep-ph].

[88] B. P. Kersevan and E. Richter-Was, *The Monte Carlo event generator AcerMC versions 2.0 to 3.8 with interfaces to PYTHIA 6.4, HERWIG 6.5 and ARIADNE 4.1*, Comput. Phys. Commun. **184** (2013) 919–985, arXiv:hep-ph/0405247 [hep-ph].

[89] E. Boos, M. Dobbs, W. Giele, I. Hinchliffe, J. Huston, et al., *Generic user process interface for event generators*, arXiv:hep-ph/0109068 [hep-ph].

[90] D. Bourilkov, R. C. Group, and M. R. Whalley, *LHAPDF: PDF use from the Tevatron to the LHC*, arXiv:hep-ph/0605240 [hep-ph].

[91] D. Salihagic, *Comparison of Beam Test Results of the Combined ATLAS Liquid Argon Endcap Calorimeters with GEANT3 and GEANT4 Simulations*. 2006.

[92] F. Aaron et al., *Combined measurement and QCD analysis of the inclusive e-p scattering cross sections at HERA*, J. High Energy Phys. **2010** no. 1, (2010).

[93] GEANT4 Collaboration, S. Agostinelli et al., *GEANT4: A Simulation toolkit*, Nucl. Instrum. Meth. **A506** (2003) 250–303.

[94] ATLAS Collaboration, T. Yamanaka, *The ATLAS calorimeter simulation FastCaloSim*, J. Phys. Conf. Series **331** no. 3, (2011) 032053.

[95] H. Lee, D. Geerts, R. van der Geer, D. Ta, P. Ferrari, M. Vreeswijk, and S. Bentvelsen, *Search for single* B' *production in the decay to* Wt *lepton+jets final states at* $\sqrt{s} = 7$ TeV., Tech. Rep. ATL-COM-PHYS-2012-1040, CERN, Geneva, Jul, 2012. Unpublished.

[96] ATLAS Collaboration, G. Aad et al., *Search for single* b^**-quark production with the ATLAS detector at* $\sqrt{s} = 7$ *TeV*, Phys. Lett. **B721** (2013) 171–189, arXiv:1301.1583 [hep-ex].

[97] ATLAS Collaboration, G. Aad et al., *Luminosity Determination in* pp *Collisions at* $\sqrt{s} = 7$ TeV *Using the ATLAS Detector at the LHC*, Eur. Phys. J. **C71** (2011) 1630, arXiv:1101.2185 [hep-ex].

[98] B. Acharya, S. Adomeit, M. Aoki, B. Alvarez, F. Balli, W. H. Bell, et al., *Object selection and calibration, background estimations and MC samples for the Autumn 2012 Top Quark analyses with 2011 data*, Tech. Rep. ATL-COM-PHYS-2012-1197, CERN, Geneva, Aug, 2012. Unpublished.

[99] A. Doxiadis, *Searching for the Top: observation of the heaviest elementary particle at the LHC*. PhD thesis, Universiteit van Amsterdam, 2010.

[100] H. Lee, *Single Top Quark Production at the LHC*. PhD thesis, Universiteit van Amsterdam, 2013.

[101] ATLAS Collaboration, G. Aad et al., *Update on the jet energy scale systematic uncertainty for jets produced in proton-proton collisions at* $\sqrt{s} = 7$ TeV *measured with the ATLAS detector*, Tech. Rep. ATLAS-CONF-2011-007, CERN, Geneva, Feb, 2011.

[102] A. Caldwell, D. Kollár, and K. Kröninger, *BAT - The Bayesian analysis toolkit*, Comput. Phys. Commun. **180** (2009) 2197–2209, arXiv:0808.2552 [physics.data-an].

[103] J. Koll, H. Zhang, R. Schwienhorst, and J. Nutter, *Search for single B' production in the model of decay to Wt dilepton final states at* $\sqrt{s} = 7$ TeV, Tech. Rep. ATL-COM-PHYS-2011-1705, CERN, Geneva, Dec, 2011. Unpublished.

[104] ATLAS Collaboration, G. Aad et al., *Estimation of non-prompt and fake lepton backgrounds in final states with top quarks produced in proton-proton collisions at* $\sqrt{s} = 8$ TeV *with the ATLAS detector*, Tech. Rep. ATLAS-CONF-2014-058, CERN, Geneva, 2014.

[105] ATLAS Collaboration, G. Aad et al., *Measurement of the top quark pair production cross-section with ATLAS in* pp *collisions at* $\sqrt{s} = 7$ TeV *in the single-lepton channel using semileptonic* b *decays*, Tech. Rep. ATLAS-CONF-2012-131, CERN, Geneva, Sep, 2012.

[106] ATLAS Collaboration, G. Aad et al., *Measurement of the* t*-channel single top-quark production cross section in* pp *collisions at* $\sqrt{s} = 7$ *TeV with the ATLAS detector*, Phys. Lett. **B717** (2012) 330–350, arXiv:1205.3130 [hep-ex].

[107] W. Verkerke and D. Kirkby, *The RooFit toolkit for data modeling*, arXiv:physics/0306116 [physics.data-an].

[108] ATLAS Collaboration, G. Aad et al., *Improved luminosity determination in* pp *collisions at* $\sqrt{s} = 7$ TeV *using the ATLAS detector at the LHC*, Eur. Phys. J. **C73** (2013) 2518, arXiv:1302.4393 [hep-ex].

[109] ATLAS Collaboration, G. Aad et al., *Calibration of* b*-tagging using dileptonic top pair events in a combinatorial likelihood approach with the ATLAS experiment*, Tech. Rep. ATLAS-CONF-2014-004, CERN, Geneva, Jan, 2014.

[110] B. Acharya, J. Adelman, S. Adomeit, M. Aoki, B. Alvarez, L. Asquith, et al., *Object selection and calibration, background estimations and MC samples for top quark analyses using the full 2012 data set*, Tech. Rep. ATL-COM-PHYS-2013-1016, CERN, Geneva, Jul, 2013. Unpublished.

[111] N. Kidonakis, *Next-to-next-to-leading-order collinear and soft gluon corrections for t-channel single top quark production*, Phys. Rev. **D83** (2011) 091503, arXiv:1103.2792 [hep-ph].

[112] N. Kidonakis, *Differential and total cross sections for top pair and single top production*, arXiv:1205.3453 [hep-ph].

[113] ATLAS Collaboration, G. Aad et al., *Measurement of the Inclusive and Fiducial Cross-Section of Single Top-Quark* t*-Channel Events in* pp *Collisions at* $\sqrt{s} = 8$ TeV, Tech. Rep. ATLAS-CONF-2014-007, CERN, Geneva, Mar, 2014.

[114] B. Acharya, J.-F. Arguin, M. Barisonzi, I. Besana, M. Bosman, I. Brock, et al., *Estimation of the W+Jets Background for Top Quark Re-Discovery in the Single Lepton+Jets Channel*, Tech. Rep. ATL-COM-PHYS-2010-834, CERN, Geneva, Oct, 2010. Unpublished.

[115] A. Lleres and X. Sun, *Measurement of t-channel single top-quark polarization observables in pp collisions at* $\sqrt{s} = 7$ TeV *with the ATLAS detector*, Tech. Rep. ATL-COM-PHYS-2012-496, CERN, Geneva, May, 2012. Unpublished.

[116] ATLAS Collaboration, G. Aad et al., *Search for* $\mathcal{CP}$ *violation in single top quark events in* pp *collisions at* $\sqrt{s} = 7$ TeV *with the ATLAS detector*, Tech. Rep. ATLAS-CONF-2013-032, CERN, 2013.

[117] ATLAS Collaboration, *Measurement of t-channel single top-quark polarization observables in pp collisions at* $\sqrt{s} = 8$ TeV *with the ATLAS detector*, in preparation.

[118] ATLAS Collaboration Collaboration, G. Aad et al., *Comprehensive measurements of* t*-channel single top-quark production cross sections at* $\sqrt{s} = 7$ *TeV with the ATLAS detector*, Phys. Rev. **D90** (2014) 112006. 50 p, arXiv:1406.7844 [hep-ex].

[119] ATLAS Collaboration, G. Aad et al., *Combination of the ATLAS and CMS measurements of the W-boson polarization in top-quark decays*, Tech. Rep. ATLAS-CONF-2013-033, CERN, Geneva, Mar, 2013.

[120] E. Wigner, *On the unitary representations of the inhomogeneous Lorentz group.*, Ann. Math. **40** (1939) 149–204.

[121] R. Ferraro and M. Thibeault, *Generic composition of boosts: an elementary derivation of the Wigner rotation*, Eur. J. Phys. **20** no. 3, (1999) 143.

[122] A.-L. de Lavoisier, *Traité élémentaire de chimie*. Culture et civilisation, 1789.

[123] D. I. Mendeleev, *The Principles of Chemistry*. Collier, 1901.

[124] A. Einstein, *Über die von der molekularkinetischen Theorie der Wärme geforderte Bewegung von in ruhenden Flüssigkeiten suspendierten Teilchen*, Ann. Phys. **322** no. 8, (1905) 549–560.

[125] J. J. Thomson, *Cathode Rays*, Philos. Mag. **44** no. 269, (1897) 293–316.

[126] E. Rutherford, *Collision of α Particles with Light Atoms IV. An Anomalous Effect in Nitrogen*, Philos. Mag. **90** no. sup1, (1910) 31–37.

[127] W. Röntgen, *On a New Kind of Rays*, Nature **53** (1896) 274–276.

[128] J. Chadwick, *Possible Existence of a Neutron*, Nature **129** (1932) 312.

[129] S. H. Neddermeyer and C. D. Anderson, *Note on the Nature of Cosmic-Ray Particles*, Phys. Rev. **51** (1937) 884–886.

[130] E. D. Bloom et al., *High-Energy Inelastic e-p Scattering at 6 and 10 degrees*, Phys. Rev. Lett. **23** (1969) 930–934.

[131] M. Breidenbach et al., *Observed Behavior of Highly Inelastic Electron-Proton Scattering*, Phys. Rev. Lett. **23** (1969) 935–939.

[132] M. Gell-Mann, *A schematic model of baryons and mesons*, Physics Letters **8** (1964) 214–215.

[133] G. Zweig, *An SU_3 model for strong interaction symmetry and its breaking; Version 1*, Tech. Rep. CERN-TH-401, CERN, Geneva, Jan, 1964.

[134] M. L. Perl et al., *Evidence for anomalous lepton production in e^+e^- annihilation*, Phys. Rev. Lett. **35** (1975) 1489–1492.

[135] J. J. Aubert et al., *Experimental Observation of a Heavy Particle J*, Phys. Rev. Lett. **33** (1974) 1404–1406.

[136] J.-E. Augustin et al., *Discovery of a Narrow Resonance in e^+e^- Annihilation*, Phys. Rev. Lett. **33** (1974) 1406–1408.

[137] S. W. Herb et al., *Observation of a Dimuon Resonance at 9.5 GeV in 400-GeV Proton-Nucleus Collisions*, Phys. Rev. Lett. **39** (1977) 252–255.

[138] PETRA Collaboration, D. P. Barber et al., *Discovery of Three-Jet Events and a Test of Quantum Chromodynamics at PETRA*, Phys. Rev. Lett. **43** (1979) 830–833.

[139] UA1 Collaboration, J. J. Aubert et al., *The ratio of the nucleon structure functions $F_2{}^N$ for iron and deuterium*, Phys. Lett. B **123** (1983) 275–278.

[140] UA1 Collaboration, G. Arnison et al., *Experimental observation of lepton pairs of invariant mass around 95 GeV/c^2 at the CERN SPS collider*, Phys. Lett. B **126** (1983) 398–410.

[141] DONUT Collaboration, K. Kodama et al., *Observation of tau neutrino interactions*, Phys. Lett. B **504** (2001) 218–224, hep-ex/0012035.

SUMMARY

Why does our universe contain primarily matter, and hardly any anti-matter? This question of baryogenesis is the main motivation for the analyses described in this thesis. *New physics* with a substantial contribution to CP-violating processes can explain the baryon asymmetry. In this thesis, *Searches for new physics through single top*, two analyses are presented that search for such new physics processes: a direct search for an excited b quark that realizes additional CP-violation, and a model-independent search for CP-violation in the top quark production and decay vertex.

The analyses use data recorded with the ATLAS detector, which is one of the largest physics experiments ever built. Situated at one of the interaction points of the Large Hadron Collider at CERN, Geneva, it is designed to measure the products of billions of proton-proton collisions a second, in search of the rare collisions where something special happens. The creation of a top quark is an example such a rare occasion. While pairs of a top quark and an antitop quark are produced relatively often, single top quarks are produced on average less than once a second. Isolating these rare events is done with numerous requirements on the properties of the events.

The top quark was discovered two decades ago, and its mass, production cross section and decay modes have been studied extensively. Nevertheless, the top quark remains a very interesting research subject due to its very high mass and the potential to find new physics in processes involving the top quark.

Both analyses described in this thesis focus at single top processes, processes where a single top quark is produced, and look for new physics, or physics *beyond the Standard Model*.

EXCITED QUARKS

The first analysis is a search for an excited bottom quark (b^*) which decays to a W boson and a top quark, providing a signature similar to that of Wt-channel single top. The b^* is produced through chromomagnetic fusion of a bottom quark and a gluon, which provides a relatively high cross section. A Feynman diagram of the process is shown in figure 50.

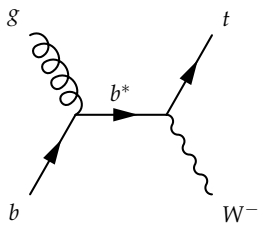

Figure 50: Feynman diagram of b^* production and decay.

The analysis is performed on 4.7 fb^{-1} of $\sqrt{s} = 7$ TeV/c^2 data collected by ATLAS in 2011, and focuses on the single lepton channel. A stringent selection is used to reduce the number of background events to roughly 30 000. The total invariant mass of the events is used to discriminate signal from background. A template fitting method is then used to set limits on the strength of the b^* couplings as a function of its mass.

The results are combined with the results of a similar search in the dilepton channel, yielding a 95% credibility level exclusion of b^* quarks with masses below $m_{b^*} = 870\ GeV/c^2$ for unit size chromomagnetic and SM-like electroweak b^* couplings. The limits have also been calculated as a function of the coupling strengths.

t-CHANNEL AND CP-VIOLATION

The second analysis focuses on the t-channel, of which a Feynman diagram is shown in figure 51. At the LHC, this channel has the highest cross section of all single top channels, and is especially interesting because the produced top quark is polarized.

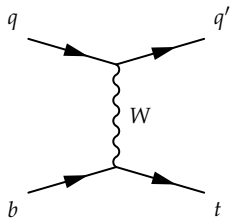

Figure 51: Feynman diagram of single top t-channel production.

This analysis uses $20.28\ fb^{-1}$ of data with $\sqrt{s} = 8\ TeV/c^2$, collected by ATLAS in 2012. First a selection is made to isolate leptonic t-channel events, in which the W boson decays to an electron or a muon. This selection results in a signal-to-background ratio of $S/B = 1$, and selects about 3500 signal events out of roughly 2 million produced in 2012. Using this selection, a cut and count cross section measurement is performed, yielding a cross section of $\sigma_{t-channel} = 100.1 \pm 2.22(stat)^{+13.3}_{-13.3}(sys)^{+19.1}_{-19.1}(th)\ pb$.

The uncertainty of this measurement is dominated by the MC generator uncertainty.

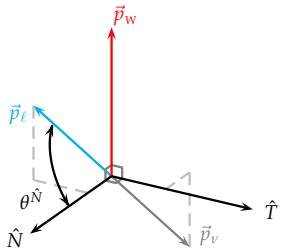

Figure 52: Angle between the momentum of the lepton in the W boson rest frame and the normal axis, as defined in the top quark rest frame.

In the second part of the analysis, the rest frames of the W boson and the top quark are reconstructed. By calculating the angle between the lepton and the light quark (q') in the top rest frame, the polarization of the top quark can be measured with a folding method and likelihood fit, resulting in $P = 0.924 \pm 0.068(stat)^{+0.178}_{-0.191}(sys)^{+0.106}_{-0.122}(th)$. The fit simultaneously determines the t-channel cross section, resulting in a measurement comparable to the one described above: $\sigma_{t-channel} = 101.9 \pm 2.8(stat)^{+10.0}_{-10.2}(sys)^{+4.7}_{-3.7}(th)\ pb$ Also in this measurement the uncertainty is dominated by the MC generator uncertainty. Also the angle of the lepton in the normal frame, which is defined in figure 52, is calculated. This is then used to measure the forward-backward asymmetry in the normal frame: $A^{\hat{N}}_{FB} = -0.018 \pm 0.044(stat)^{+0.019}_{-0.018}(sys)^{+0.005}_{-0.005}(th)$. All measurements are consistent with the Standard Model.

The measurements of the top quark polarization and the forward-backward asymmetry in the normal frame are then combined to a measurement of the imaginary part of the right-handed tensor coupling ($\Im(g_R)$), which is sensitive to CP-violation. The result

is $\mathcal{I}(g_R) = -0.030 \pm 0.074(\text{stat})^{+0.025}_{-0.023}(\text{sys})^{+0.008}_{-0.008}(\text{th})$, which is also fully compatible with the Standard Model. Therefore no CP-violation is observed.

In conclusion, neither analysis described in this thesis has found any deviation from the Standard Model. However, the Wtb vertex can still provide a significant source of CP-violation and the hypothesis for the baryogenesis is not yet ruled out. It may well be that future LHC data provides the answer to this big question.

SAMENVATTING

Waarom bevat ons universum voornamelijk materie, en nauwelijks antimaterie? Deze kwestie van baryogenesis is de belangrijkste motivatie voor de analyses die dit proefschrift zijn bescreven. *Nieuwe fysica* met een substantiële contributie aan LP-schendende processen zou de baryon-asymmetrie kunnen verklaren. Dit proefschrift, *Searches for new physics through single top*, presenteerd twee analyses die zoeken naar zulke nieuwe fysica: een directe zoektocht naar een aangeslagen b-quark, en een modelonafhankelijke zoektocht naar LP-schending in de productie- en vervalsvertex van het top-quark.

De analyses gebruiken data die opgenomen zijn met het ATLAS-detector, dat een van de grootste natuurkundige experimenten is ooit gebouwd is. Het is gelegen aan een van de interactiepunten van de Large Hadron Collider bij CERN, Genéve, en ontworpen om miljarden proton-proton botsingen per seconde te meten, op zoek naar de zeldzame botsingen waar iets bijzonders gebeurt. De productie van een top-quark is een voorbeeld van zo'n zeldzame gelegenheid. Hoewel paren van een top-quark en een antitop-quark relatief vaak voorkomen, worden enkele top-quarks gemiddeld minder dan één keer per seconde geproduceerd. Het isoleren van deze zeldzame gebeurtenissen wordt gedaan door tal van eisen te stellen aan de eigenschappen van de gebeurtenissen.

Het top quark werd twee decennia geleden ontdekt, en zijn massa, productiedoorsnede en vervalmodi zijn uitgebreid bestudeerd. Toch blijft het top-quark een zeer interessant onderzoeksobject vanwege de zeer hoge massa en de potentie om nieuwe fysica vinden in de processen van het top-quark.

Beide analyses in dit proefschrift zijn gericht op enkele-topprocessen, processen waarbij een enkel top-quark wordt geproduceerd, en zoeken naar nieuwe fysica, of *natuurkunde voorbij het Standaardmodel*.

AANGESLAGEN QUARKS

De eerste analyse is een zoektocht naar een aangeslagen bottom-quark (b^*) dat vervalt naar een W-boson en een top-quark, zodat een signaal vergelijkbaar aan dat van het Wt-kanaal enkele-top ontstaat. De b^* wordt geproduceerd door middel van chromomagnetische fusie van een bottom-quark en een gluon, wat een relatief hoge productiedoorsnede mogelijk maakt. Een Feynmandiagram van het proces is weergegeven in figuur 53.

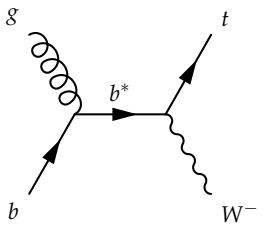

Figuur 53: Feynmandiagram van b^*-productie en -verval.

De analyse is uitgevoerd op 4,7 fb^{-1} $\sqrt{s} = 7$ TeV/c^2 door ATLAS in 2011 verzamelde data, en richt zich op het enkele-leptonkanaal. Een strenge selectie wordt gebruikt om het aantal achtergrondgebeurtenissen te reduceren tot ongeveer 30 000. De totale invariante massa van de gebeurtenissen wordt gebruikt om het signaal te onderscheiden van de achtergrond.

Een sjabloon-fittingmethode wordt vervolgens gebruikt om limieten op de sterkte van de b^*-koppelingen te zetten als een functie van de massa.

De resultaten zijn gecombineerd met de resultaten van een soortgelijke analyse in het dileptonkanaal, wat een exclusie oplevert van b^*-quarks met massa's onder $m_{b^*} = 870\ GeV/c^2$ met een geloofwaardigheidsniveau van 95% voor chromomagnetische koppelingen met sterkte 1 en Standaardmodel-achtige elektrozwakke b^*-koppelingen. De limieten zijn eveneens berekend als functie van de koppelingssterkten.

t-KANAAL AND LP-SCHENDING

De tweede analyse richt zich op het t-kanaal, waarvan een feynmandiagram is weergegeven in figuur 54. Bij de LHC heeft dit kanaal de hoogste productiedoorsnede van alle enkele-top-kanalen. Het is vooral interessant omdat het geproduceerde topquark gepolariseerd is.

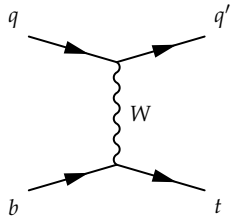

Figuur 54: Feynmandiagram van enkele-top t-kanaal productie.

Deze analyse maakt gebruik van 20,28 fb^{-1} aan data met $\sqrt{s} = 8\ TeV/c^2$ die door ATLAS is verzameld in 2012. Eerst wordt een selectie gemaakt om leptonische t-kanaalgebeurtenissen, waarbij het W-boson vervalt tot een elektron of een muon, te isoleren. Deze selectie resulteert in een signaal- tot-achtergrond verhouding van $S/B = 1$, en selecteert ongeveer 3500 signaalgebeurtenissen uit de ongeveer 2 miljoen geproduceerde in 2012. Met deze selectie wordt een snij-en-tel doorsnedemeting uitgevoerd, waarmee een doorsnede van $\sigma_{t-kanaal} = 100{,}1^{+23{,}4}_{-23{,}0}$ pb wordt gevonden. De onzekerheid van deze meting wordt gedomineerd door de montecarlogenerator-onzekerheid.

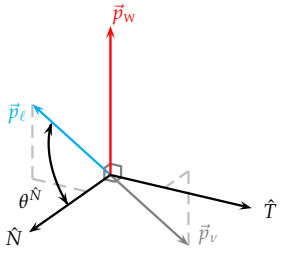

Figuur 55: Hoek tussen de impuls van het lepton in het W-boson-ruststelsel en de loodrechte as, zoals gedefinieerd in het top-quark-ruststelsel.

In het tweede deel van de analyse, worden de ruststelsels van het W-boson en het top-quark gereconstrueerd. Door het berekenen van de hoek tussen het lepton en het lichte-quark (q') in het top-ruststelsel, kan de polarisatie van het top-quark worden gemeten met een vouwmethode en waarschijnlijkheidsfit, wat resulteert in $P = 0{,}924^{+21{,}8}_{-23{,}7}$. De fit bepaalt gelijktijdig de t-kanaal-doorsnede, wat resulteert in een meting te vergelijken met de meting die hierboven is beschreven: $\sigma_{t-kanaal} = 101{,}9^{+23{,}5}_{-23{,}6}$ pb. In deze meting wordt de onzekerheid ook gedomineerd door de montecarlogenerator-onzekerheid. Ook de hoek van het lepton in het normale stelsel, zoals gedefiniëerd in figuur 55, wordt berekend. Dit wordt daarna gebruikt om de voorwaarts-achterwaartsasymmetrie in het normale stelsel te meten: $A_{FB}^{\hat{N}} = -0{,}018 \pm 0{,}044(stat)^{+0{,}019}_{-0{,}018}(sys)^{+0{,}005}_{-0{,}005}(th)$. Alle resultaten zijn consistent met het Standaardmodel.

The metingen van de polarisatie van het top-quark en de voorwaarts-achterwaarts-asymmetrie in het normale stelsel worden daarna gecombineerd tot een meting van het

imaginaire deel van de rechtshandige tensorkoppeling ($\mathfrak{I}(g_R)$), die gevoelig is voor LP-schending. Het resultaat is $\mathfrak{I}(g_R) = -0{,}030 \pm 0{,}074(\text{stat})^{+0{,}025}_{-0{,}023}(\text{sys})^{+0{,}008}-0{,}008(\text{th})$, wat ook volledig compatibel is met het Standaardmodel. Geen LP-schending is waargenomen.

In conclusie: geen van beide analyses die beschreven zijn in dit proefschrift heeft enige afwijking gevonden van het Standaardmodel. Desalniettemin kan de Wtb-vertex een belangrijke bron van LP-schending zijn, en de hypothese van baryogenesis is nog niet verworpen. Toekomstige data van de LHC kan het antwoord op deze vraag geven.

POPULAIR-WETENSCHAPPELIJKE INTRODUCTIE

In dit proefschrift, *Searches for new physics through single top*, beschrijf ik twee analyses die ik heb gedaan met de data van de ATLAS-detector, een van de grootste deeltjesfysica-experimenten ooit gedaan. In deze samenvatting geef ik een toegankelijke inleiding in de deeltjesfysica en sluit ik af met een beschrijving van het onderzoek in dit proefschrift.

ELEMENTAIRE DEELTJES

De deeltjesfysica draait om de vraag *waar is de wereld van gemaakt?* De wereld om ons heen bevat veel verschillende dingen zoals mensen, dieren en planten, maar ook levenloze dingen als zand, lucht en dit proefschrift. De vraag waar al die dingen van gemaakt zijn houdt de mensheid al enkele millenia bezig.

Zo dacht de Siciliaanse filosoof Empedocles, zo'n 450 jaar voor het begin van de jaartelling, dat alles in de wereld was gemaakt van vier elementen: *vuur*, *aarde*, *lucht* en *water*. Aristoteles bedacht daar ongeveer een eeuw later een vijfde element bij: *ether*, waar de hemel en de goden van gemaakt zouden moeten zijn.

Veel andere culturen in de klassieke periode, zoals de Egyptenaren en de Buddhisten, hadden dezelfde vier of vijf elementen. Enkele culturen hadden hier varianten op, zoals de Tibetanen (*ruimte* in plaats van *ether*) en de Chinezen (*vuur*, *aarde*, *metaal*, *water* en *hout*).

In ruwweg dezelfde periode van de Griekse oudheid filosofeerde Democritos dat alle materie is opgebouwd uit piepkleine deeltjes, die niet verder op te delen zijn in kleinere stukjes. Hij noemde deze elementaire deeltjes *atomen*, wat 'ondeelbaar' betekent.

Het heeft vele eeuwen geduurd voor er verandering kwam in de klassieke ideeën over de elementen: in de eerste helft van de 18^{e} eeuw werden enkele chemische elementen gevonden. De Fransman Antoine-Laurent de Lavoisier publiceerde in 1789 een lijst [122] met daarin rond de dertig 'chemische elementen', waaronder zuurstof en waterstof, maar ook licht.

Het aantal elementen groeide in de loop der jaren, en ruwweg een eeuw later zag Dmitrii Mendeleev het licht [123]: hij ontdekte een systeem (het *periodiek systeem*) in de eigenschappen van de (op dat moment) 64 elementen. Met dat systeem kon hij het bestaan van nog niet ontdekte elementen, en hun eigenschappen, voorspellen.

In dezelfde periode kwam de Engelsman John Dalton met de eerste waarnemingen die de atoomtheorie, de theorie dat alle materie uit atomen bestaat, steunden. In 1905 kwam Albert Einstein met berekeningen die de theorie steunden [124], en Jean Baptiste Perrin kwam met de beslissende waarnemingen: het stond vast dat materie uit atomen bestond.

De theorie over de materie bleek echter nog niet compleet. Sir Joseph John Thomson ontdekte een deeltje dat veel kleiner was dan een atoom: het elektron [125]. Het feit dat elektronen zich *in* atomen bevinden betekende dat atomen, ondanks hun naam, niet ondeelbaar zijn. Enkele decennia later ontdekte Ernest Rutherford de atoomkern, waarvan hij niet veel later aantoonde dat deze uit protonen bestaat [126].

Daarmee was de theorie van de materie plots heel anders: het aantal elementaire deeltjes was teruggebracht van vele tientallen naar slechts drie (het elektron, het proton en het foton, dat in 1896 was ontdekt door Wilhelm Röntgen [127]). Men wist nu dat atomen samengestelde deeltjes waren, bestaande uit een atoomkern van protonen en daaromheen elektronen. Het bleef echter niet bij de drie elementen: James Chadwick toonde aan dat er naast protonen ook neutronen in atoomkernen zitten [128]. Zo kwam het model van een atoom er zo uit te zien als in figuur 56.

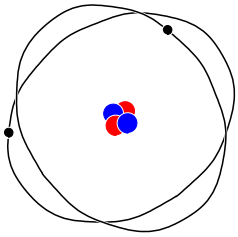

Figuur 56: Het klassieke atoommodel, met in het middel een kern met protonen en neutronen (rood en blauw) en daaromheen elektronen in cirkelbanen (zwart).

Ook hierbij bleef het niet: het muon, een zwaardere, instabiele variant van het elektron, werd ontdekt in 1937 [129]. Tien jaar later werden kort na elkaar het pi-meson (pion), het K-meson (kaon) en het Λ^0-baryon ontdekt. Daarna ging het snel: binnen vijftien jaar werden twee neutrino's, extreem lichte deeltjes die vrijwel overal ongehinderd doorheen vliegen, en enkele tientallen nieuwe mesonen en baryonen ontdekt.

De grote hoeveelheid mesonen en baryonen deed vermoeden dat ook deze deeltjes, net als de atomen, geen elementaire deeltjes waren. Dat bleek in 1969, toen een structuur in het proton (een baryon) werd gemeten [130, 131]. De deeltjes in het proton werden al snel geïdentificeerd als quarks [132, 133]. Wederom was de theorie van de materie plots heel anders. Er waren nu acht elementaire deeltjes: het foton, twee *leptonen* (het elektron en het muon), twee neutrino's en drie quarks. Alle mesonen en baryonen bestaan uit combinaties van de drie quarks, het up-quark, down-quark en het strange-quark, zoals het proton en het neutron in figuur 57.

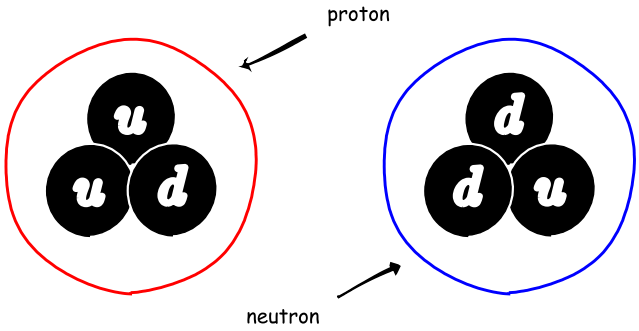

Figuur 57: De substructuur van het proton en neutron: het proton bestaat uit twee up-quarks en een down-quark, en het neutron bestaat uit twee down-quarks en een up-quark.

Kort daarop werd het aantal elementaire deeltjes echter weer uitgebreid met de ontdekking van een derde lepton (het tau-lepton) [134], en een vierde en een vijfde quark (het charm-quark en het bottom-quark) [135–137]. Het gluon, het krachtdeeltje dat quarks bijeen houdt in bijvoorbeeld protonen, werd ontdekt in 1979 [138], en de W- en Z-bosonen die verantwoordelijk zijn voor radioactief β-verval van atoomkernen niet lang daarna in 1983 [139, 140]. Daarna volgden nog het top-quark in 1995 [18, 19], het tau-neutrino in 2000 [141], en meest recentelijk het Higgs-boson in 2012 [5, 6].

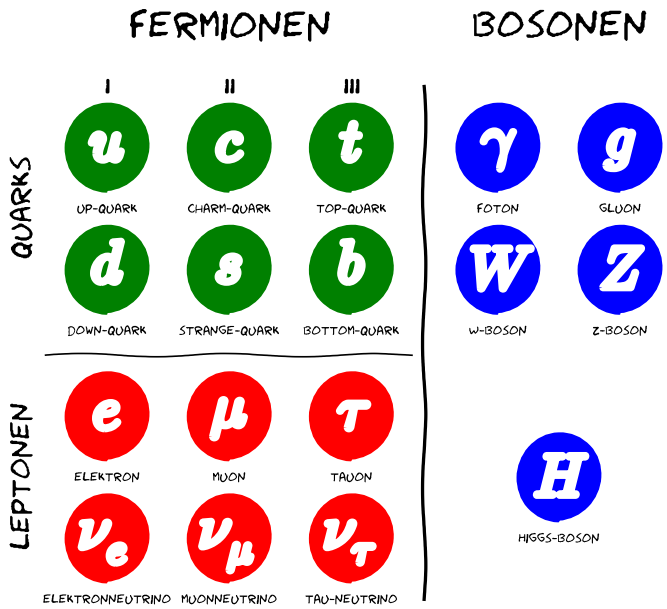

Figuur 58: Alle deeltjes in het Standaardmodel.

Met die laatste ontdekking is het *Standaardmodel*, het model dat alle deeltjes en interacties beschrijft, compleet. We kennen nu 17 deeltjes[2], die opgedeeld kunnen worden in de *fermionen*, de materiedeeltjes, en de *bosonen*, de krachtdeeltjes (zie ook figuur 58). De materiedeeltjes kunnen weer opgedeeld worden in de *quarks* en de *leptonen*, waarvan er elk drie families bestaan.

Alle materie in onze wereld is gemaakt van de deeltjes in de eerste familie: protonen en neutronen bestaan uit up- en down-quarks, en atomen bestaan uit een kern van protonen en neutronen en daaromheen elektronen. De deeltjes in de hogere families zijn vrijwel identiek aan hun buren in de eerste familie, maar zijn zwaarder en daarom *instabiel*: ze vervallen na een (zeer) korte tijd in lichtere deeltjes. De neutrino's zijn een apart verhaal,

2 Hierbij tel ik de antideeltjes, deeltjes met vrijwel dezelfde maar soms omgekeerd eigenschappen, niet mee.

aangezien ze alledrie zeer licht zijn en vrijwel niet te detecteren zijn: die kom je in het dagelijks leven niet tegen.

De bosonen zijn geen materie, maar brengen krachten over. Zo wordt de elektromagnetische kracht (licht) overgebracht door fotonen. Het gluon brengt de sterke kernkracht over, en de W- en Z-bosonen zijn de overbrengers van de zwakke kernkracht. Het Higgs-boson brengt geen kracht over, maar zorgt er voor dat deeltjes massa hebben: als het niet zou bestaan zou alles altijd met de lichtsnelheid bewegen.

Het feit dat het Standaardmodel nu compleet is betekent niet dat we achterover kunnen gaan zitten. Het model heeft namelijk nog enkele tekortkomingen. Zo komt de vierde kracht die we kennen, de zwaartekracht, niet voor in het Standaardmodel. Het graviton, het deeltje dat de zwaartekracht over zou brengen, past namelijk niet in de theorie. Een ander probleem is dat het Standaardmodel het bestaan van donkere materie, massa die in sterrenstelsels aanwezig is maar geen licht uitstraalt, niet kan verklaren.

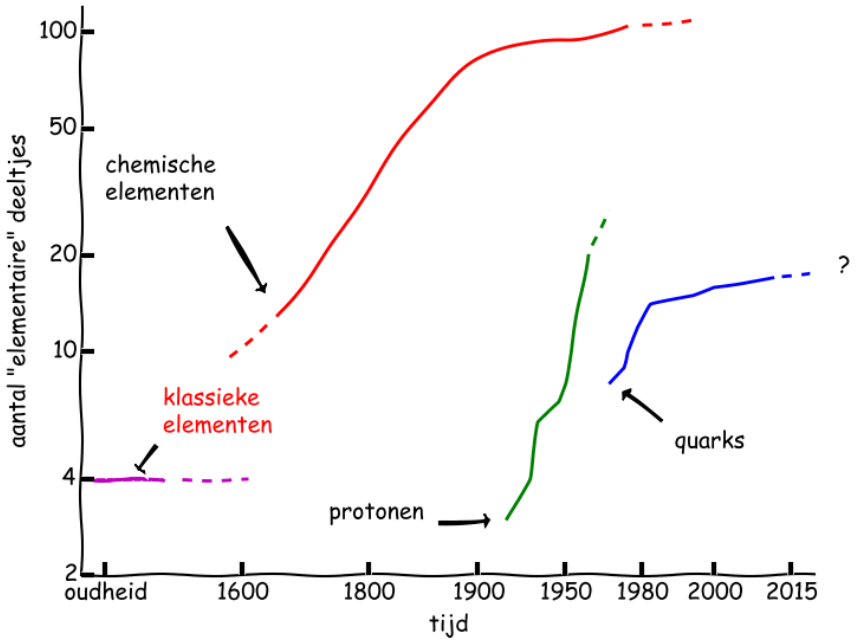

Figuur 59: Het aantal 'elementaire' deeltjes door de eeuwen heen.

Figuur 59 vat de geschiedenis van de deeltjesfysica kort samen. Weergegeven is het aantal deeltjes waarvan men dacht dat ze elementair waren als functie van de tijd. Al tweemaal in de afgelopen eeuwen is gebleken dat deeltjes, waarvan men dacht dat ze elementair waren, samengesteld waren uit andere deeltjes. Al is het natuurlijk verleidelijk om te denken dat de deeltjes in Standaardmodel allemaal elementair zijn, gezien de geschiedenis zou dat onverstandig zijn. Op dit moment weten we echter niet beter.

Ook daarom wordt er druk gezocht naar zogenaamde *nieuwe fysica* of afwijkingen van het Standaardmodel. Er zijn voldoende theorieën die voorspellingen doen over wat er gevonden zal worden, zoals supersymmetrie [10] en stringtheorie [11], maar feit is dat we niet weten wat we zullen vinden. Misschien een supersymmetrisch deeltje? Of een vier generatie materie? Een substructuur in het elektron of een quark? We weten het niet. Het zou natuurlijk ook goed kunnen dat we iets vinden dat we totaal niet verwachten.

VERSNELLERS EN DETECTOREN

Het onderzoek beschreven in dit proefschrift gaat over de allerkleinste deeltjes die bestaan. Om het onderzoek te doen, en deze deeltjes waar te nemen, zijn gigantisch grote apparaten nodig. Waarom kunnen we deze deeltjes niet 'gewoon' zien?

Zien doen we normaliter met onze ogen, maar daarmee kunnen we geen dingen onderscheiden die kleiner zijn dan ruwweg 0,1 mm. Ter vergelijking: een proton is ongeveer 1 fm breed[3]. Met een microscoop kunnen we veel kleinere objecten onderscheiden, maar zelfs met de beste microscoop is het nooit mogelijk om kleinere objecten dan zo'n 500 nm te zien[4]. Dat komt niet door de microscoop, maar door de kwantummechanische eigenschappen van het licht waarmee we objecten bekijken: de fotonen in zichtbaar licht hebben een golflengte, die je kort door de bocht kan opvatten als de breedte van het deeltje, tussen de 400 en 700 nm, en zijn dus (veel) groter dan een proton. Het waarnemen van een proton met (zichtbaar) licht is net als het lezen van braille met een skippybal of het afspelen van een langspeelplaat met een wolkenkrabber als naald: dat werkt niet.

Alle elementaire deeltjes hebben een dergelijke golflengte, die afhangt van de energie van het deeltje[5]: hoe groter de energie, hoe kleiner de golflengte. Deeltjes die klein genoeg zijn om een atoomkern te bekijken moeten veel energie hebben. Om in een proton te kijken is gigantisch veel energie nodig. Om al die energie in een deeltje te krijgen moet het deeltje versneld worden tot bijna de lichtsnelheid.

Om de deeltjes tot zo'n grote snelheid te versnellen is een hele grote machine nodig. De Large Hadron Collider (LHC) bij CERN, Genève, is zo'n grote machine. De LHC ligt 100 meter ondergronds, in een tunnel die een rondje van 27 kilometer beschrijft. In de versneller worden protonen versneld tot bijna de lichtsnelheid. Op maximale snelheid vliegen de protonen meer dan 11 000 rondjes per seconde, verdeeld in twee bundels: de ene linksom, de andere rechtsom.

Op vier plekken in de versneller, de zogenaamde interactiepunten, snijden de bundels elkaar. Hier botsen de protonen met gigantische energie op elkaar, waarna fragmenten en nieuwe deeltjes alle kanten op vliegen. Rond deze interactiepunten zijn grote detectoren gebouwd, waarvan ATLAS er één is. ATLAS is met zijn $46 \times 25 \times 25$ meter de grootste detector van de LHC.

3 Een femtometer (fm) is 10^{-15} m, ofwel 0,000 000 000 000 001 m.
4 Een nanometer (nm) is 10^{-9} m, ofwel 0,000 000 001 m.
5 Dit is de Comptiongolflengte, die gegeven wordt door $\lambda = \frac{hc}{E}$, waar E de energie is van het deeltje en h en c constanten zijn.

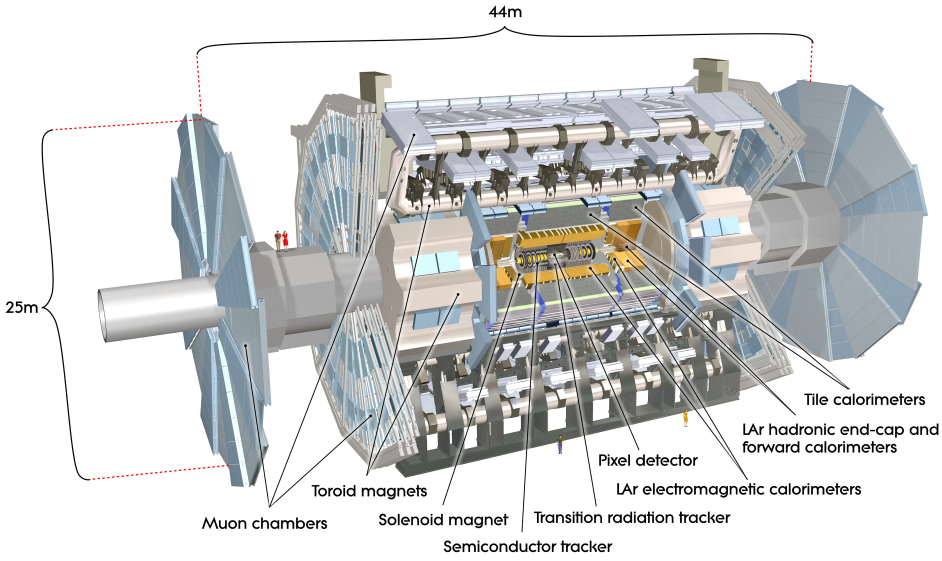

Figuur 60: Een overzicht van de ATLAS-detector.

DIT PROEFSCHRIFT

De analyses die ik beschrijf in dit proefschrift draaien om top-quarks. Top-quarks zijn de zwaarste deeltjes die we kennen, met een massa meer dan 300 000 keer groter dan die van een elektron. Mede door die grote massa bestaan top-quarks maar heel kort: na 10^{-25} s vervallen ze[6], vrijwel altijd in een bottom-quark en een W-boson.

In versnellers als de LHC worden top-quarks meestal in paren gemaakt: een top-quark en een antitop-quark, zijn antideeltje. Top-quarks kunnen ook alléén geproduceerd worden. Er zijn drie van zulke zogenaamde *single top*-processen. Deze worden heel cryptisch het t-kanaal, het s-kanaal en het Wt-kanaal genoemd. Ik heb twee analyses gedaan, gericht op twee verschillende single top-kanalen.

De eerste van de twee analyses is gericht op het Wt-kanaal. In dit proces wordt het top-quark samen met een W-boson gemaakt. In dit kanaal heb ik gezocht naar een hypothetisch nóg zwaarder quark, het b*-quark, dat zou vervallen in een top-quark en een W-boson. Dit zijn dezelfde deeltjes als die in het Wt-kanaal geproduceerd worden, en daarom zou het signaal van het b*-quark erg lijken op het signaal van het Wt-kanaal. Omdat het b*-quark zo zwaar zou zijn is het toch mogelijk de twee van elkaar te onderscheiden.

In deze analyse heb ik het b*-quark niet kunnen ontdekken. Desondanks kan het nog wel bestaan, maar als het bestaat komt het óf heel weinig voor, óf het is te zwaar om in de LHC gemaakt te kunnen worden.

6 Dat is 0,000 000 000 000 000 000 000 000 1 s.

De tweede analyse richt zich op het t-kanaal. Dit proces, waarin het top-quark samen met een lichter quark wordt gemaakt, komt het vaakst voor van de single top-processen.

Allereerst heb ik de *werkzame doorsnede* van dit proces gemeten: de werkzame doorsnede is een maat voor hoe vaak het proces voorkomt. Om deze doorsnede te bepalen is het nodig om dit proces heel goed te kunnen onderscheiden van processen die erop lijken: de zogenaamde achtergronden.

Eenmaal ontdaan van de achtergronden is het ook mogelijk eigenschappen van het proces te bestuderen. Eén van de interessante eigenschappen van het t-kanaal-proces is de polarisatie van het top-quark: de manier waarop het top-quark om zijn as draait. Aan de hand van deze polarisatie kunnen we vaststellen welke koppelingen in het proces een rol spelen. Ook in deze analyse heb ik geen afwijkingen van het Standaardmodel gevonden.